# Magnetic and optical studies of transition metals-doped ZnS nanostructures

A THESIS

Submitted to the

FACULTY OF SCIENCE

THAPAR UNIVERSITY PATIALA

**for the degree of**

**Doctor of Philosophy**

By

**Sunil Kumar**

Regn. No. 951112005


School of Physics & Materials Science

Thapar University

Patiala - 147 004

INDIA

July 2015

# Declaration

It is certified that the thesis work is my own and that the ideas and references cited herein have been duly acknowledged.

(Sunil Kumar)

Attestation by supervisor

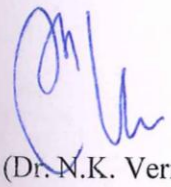

(Dr. N.K. Verma)

Senior Professor

School of Physics and Materials Science,

Thapar University,

Patiala-147004

Punjab, INDIA

# Certificate

This is to certify that thesis entitled, "Magnetic and optical studies of transition metals-doped ZnS nanostructures", submitted by Mr. Sunil Kumar in the partial fulfillment of degree of Doctor of Philosophy in the School of Physics & Materials Science, Thapar University, Patiala, is a record of candidates own work carried out under my supervision and guidance. The matter presented in this thesis has not been submitted in part or full for the award of any degree in any other University or Institute.

Attestation by supervisor

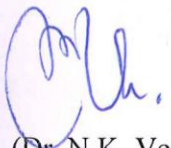

(Dr. N.K. Verma)

Senior Professor

School of Physics and Materials Science,

Thapar University,

Patiala-147004

Punjab, INDIA

# *ACKNOWLEDGEMENT*

*I am really grateful to the Almighty who helped me complete the project within time. With deep regards and profound respect, I extend my gratitude to my supervisor, Dr. N.K. Verma, Senior Professor, School of Physics and Materials Science, Thapar University, Patiala for introducing the present research topic and for his constant guidance, constructive criticism and valuable suggestions throughout this research work. It would have not been possible for me to bring out this work without his help and constant encouragement.*

*I am obliged to Professor Prakash Gopalan, Director, Thapar University for providing infrastructure to carry out research work in a friendly environment. I am highly obliged to Dr. Manoj Kumar Sharma, Head of School of Physics and Materials Science, for his encouragement and support.*

*I would like to thank the Doctoral Committee Members comprising Dr. Puneet Sharma, Dr. S.D. Tiwari and Dr. Bonamali Pal, for their encouragement, constructive comments, and guidance. I am also thankful to the faculty of the School of Physics and Materials Science for their timely guidance and encouragement.*

*I extend my whole hearted gratitude towards Dr. R.K. Jha, Vice Chancellor, Indus International University, Una, Himachal Pradesh, for his motivation, encouragement, and whole-hearted support throughout my research work.*

*I also express my sincere thanks to Dr. Manish Taunk, Department In-charge, Department of Physics, Indus International University, Una, Himachal Pradesh, for his continuous academic support and encouragement.*

*My special thanks to Dr. Sanyog Jain, Assistant Professor, National Institute of Pharmaceutical Education and Research (NIPER), Mohali, Dr. Manasmita Das, University of North Carolina,*

*Chapel Hill, USA, Dr. Akash Katoch, South Korea, Mr. Dinesh Chauhan, National Physical Laboratory, New Delhi and Mr. Narendra Verma, IIT Kanpur, for helping me in this journey.*

*I am thankful to my friends and colleagues: Dr. Manveen Kaur, Dr. Gurmeet Lotey, Dr. Lalanya Khanna, Dr. Jaspal Singh, Mrs. Kamaldeep Kaur, Ms. Gitanjali, Mr. Sudhanshu Singh and Mr. Tej Singh for their cooperation and constant help.*

*I would also take this opportunity to express my gratitude to the non-teaching staff of School of Physsics and Materials Science, and Mr. Vijay from registry, for their help.*

*I am indebted to my parents: Late Mr. Jagdish Singh and Mrs. Ratni Devi for their blessings as well as my wife Mrs. Nitu Kumari for her unconditional support and cooperation, my son Ayushman Thakur, for his love, and brothers Susheel, Praveen, Manish and sister Sunita, for their encouragment and support.*

***(Sunil Kumar)***

# *Contents*

# Chapter 2. Synthesis and characterizations

## Chapter 3. Results and discussion

# *LIST OF FIGURES*

# *LIST OF TABLES*

# *LIST OF PUBLICATIONS*

## I. In SCI Journals

1. **Sunil Kumar, N.K. Verma,** Investigation of the magnetic and optical properties of wurtzite Fe-doped ZnS nanorods, Journal of Electronic Materials, 2015, 44:2829-2834.
2. **Sunil Kumar, N.K. Verma,** Structural, optical and magnetic investigations on Fe-doped ZnS nanoparticles, Journal of Material Science: Materials in Electronics, 2015, 26:2754-2759.
3. **Sunil Kumar, N.K. Verma,** Room Temperature Magnetism in Co-Doped ZnS nanoparticles, Journal of Superconductivity and Novel Magnetism, 2015, 28:137-142.
4. **Sunil Kumar**, **N.K. Verma,** Room temperature investigations on optical and magnetic studies of $Zn_{1-x}Co_xS$ Nanorods, Journal of Magnetism and Magnetic Materials, 2015, 374:548–552**.**
5. **Sunil Kumar**, N.K. Verma, Ferromagnetic and weak superparamagnetic like behaviour of Ni-doped ZnS nanocrystals synthesized by reflux method, Journal of Materials Science: Materials in Electronics, 2014, 25:1132-1137**.**
6. **Sunil Kumar**, N.K. Verma, Effect of Ni-doping on optical and magnetic properties of solvothermally synthesized ZnS wurtzite nanorods, Journal of Materials Science: Materials in Electronics, 2014, 25:785-790.

## II. Publications in addition to Ph.D. work (published earlier to registering for PhD)

1. **Sunil Kumar**, Manasmita Das, Raman Preet Singh, Satyajit Datir, Dinesh Singh and Sanyog Jain, Mathematical models for the oxidative functionalization of multiwalled carbon nanotubes. Colloids and Surfaces A: Physicochemical Engineering Aspects, 2013, 419:156– 165.
2. Manasmita Das, Debarati Bandyopadhyay, Ramanpreet Singh, **Sunil Kumar**, Sanyog Jain, Orthogonal biofunctionalization of magnetic nanoparticles via "clickable" poly-(ethylene glycol) silanes: a "*universal ligand*" strategy to design stealth and target-specific nanocarriers. Journal of Material Chemistry, 2012: 22, 24652.
3. **Sunil Kumar**, Zinki Jindal, Nitu Kumari, N.K. Verma, Solvothermally synthesized europium doped CdS nanorods: applications as phosphors. Journal of Nanoparticles Research, 2011, 13:5465-5471.
4. **Sunil Kumar**, Nitu Kumari, Sudhanshu Singh, Tej Singh, Sanyog Jain, Doping studies of Tb (terbium) and Cu (copper) on CdSe nanorods. Colloids and Surfaces A: Physicochemical and Engineering Aspects, 2011, 389:1-5.
5. **Sunil Kumar**, Sanjeev Kumar, N.K. Verma, S.K. Chakravarti, Room temperature ferromagnetism in solvothermally synthesized pure CdSe and CdSe:Ni nanorods. Journal of Materials Science: Materials in Electronics, 2011, 22:1456-1459.
6. **Sunil Kumar**, Sanjeev Kumar, N.K. Verma, S.K. Chakravarti, Room temperature magnetism in Ni-doped CdSe nanoparticles. Journal of Materials Science: Materials in Electronics. 2011, 22:901-904.

7. **Sunil Kumar**, Sanjeev Kumar, N.K. Verma, S.K. Chakravarti, Room temperature ferromagnetic behaviour of Eu-doped $Cd_{1-x}Zn_xS$ nanoparticles, Journal of Materials Science: Materials in Electronics, 2011, 22: 523-526.

## III. Publications in non-SCI journals

1. **Sunil Kumar**, Nitu Kumari, Inderpreet Kaur, Sanyog Jain, Keya Dharamveer, V.K. Jindal, N. K. Verma, L.M. Bharadwaj, Atomic force microscope nanomanipulation of multiwalled and single walled carbon nanotubes with different physical and chemical treatments. Applied Nanoscience, 2014, 4:19–26.
2. **Sunil Kumar**, Nitu Kumari, Sanjeev Kumar, Sanyog Jain, N. K. Verma, Synthesis and characterization of Ni-Doped CdSe nanoparticles: magnetic studies in 300K-100K temperature range. Applied Nanoscience, 2012, 2:437–443.
3. Sanjeev Kumar, **Sunil Kumar**, Sanyog Jain, N. K. Verma, Magnetic and structural characterization of transition metal co-doped CdS nanoparticles. Applied Nanoscience, 2012, 2:127–131.

## IV. Papers in Conferences/Proceedings

1. **Sunil Kumar**, N.K. Verma, Magnetic and optical studies of $Zn_{1-x}Ni_xS$ nanostructures" at International conference, NANOSCITECH2014, held at Punjab University, Chandigarh, India on 13-15 February, 2014.
2. **Sunil Kumar**, N.K. Verma, Room temperature structural and magnetic investigations on Fe-doped ZnS nanostructures, at Career Point University, Hamirpur, Himachal Pradesh, India on May 10, 2014.

3. **Sunil Kumar**, N.K. Verma, Structural, optical and magnetic studies of $Zn_{1-x}Co_xS$ nanostructures at National Congress on Science and Technology-NCST-13 held at DAVIET, Jalandhar, Punjab, India on May 30-31, 2013.
4. **Sunil Kumar**, N.K. Verma, "Solvothermally synthesized Eu-doped CdS nanorods" at Second Winter School on theme "Nanotechnology in Advanced Drug Delivery" at National Institute of Pharmaceutical Education & Research(NIPER), S.A.S. Nagar, Mohali, Punjab, India in Feb. 2009.

# *ABSTRACT*

One of the challenges for the development of future electronic technologies is the realization of devices that control not only the electron charge, as in present electronics, but also its spin, setting the foundation for future spintronics. In this scenario dilute magnetic semiconductor materials (DMS), with electron charge and spin characteristics, are the ideal candidates to meet these challenges. The spin can induce new functionalities in the spintronics devices which have no analogue in today's semiconductor devices. The study of DMS at nanoscale can provide the possibility of tuning the lattice constants and band gap parameters by varying the amount of the dopant atom and the size of nanomaterials. However, till date, few efforts have been made towards exploiting the room temperature ferromagnetism in transition metals-doped semiconductor nanostructures, but, a concrete universal model is yet to be developed to explain the possible cause of ferromagnetism in doped semiconductor nanostructures. Therefore, it has stimulated a great interest in both basic and applied research.

In present thesis work, the structural, optical and magnetic properties of transition metals-doped ZnS nanostructures, nanoparticles and nanorods, synthesized using chemical synthesis route, have been analyzed. The properties have been studied using various techniques viz. transmission electron microscope (TEM), High resolution (HRTEM), X-ray diffraction (XRD), energy dispersive spectroscopy (EDS), UV-Visible spectroscopy (UV-Vis.), photoluminescence spectroscopy (PL) and vibrating sample magnetometer (VSM). The properties of transition metals-doped ZnS nanostructures found altered than their bulk and undoped counterparts. Magnetism has been observed at room temperature in case of undoped and transition metals-doped ZnS nanostructures; however, the dopants concentration, leading to various exchange interactions, plays a decisive role in inculcating altered optical and magnetic character in ZnS.

# *PREFACE*

This thesis presents structural, optical, and magnetic studies of transition metals-doped ZnS nanostructures, synthesized via chemical synthesis route. These properties have been analyzed using various advanced characterization techniques. The possible mechanisms responsible for the interactions between the guest and host elements have been discussed in detail. This thesis consists of four chapters. Chapter-wise description of thesis is given below:

**Chapter 1** includes in-depth introduction of DMS. It includes the importance of nanotechnology and nanomaterials in various applications. Stress is given on the need of DMS, particularly at nanoscale, in spintronics devices. Various theoretical mechanisms responsible for magnetism in DMS materials have been discussed in detail. The chapter provides a comprehensive literature review to fill the gaps in the existing studies. At the end of the chapter, the potential of ZnS as DMS material has been presented.

**Chapter 2** includes various materials used in synthesizing undoped and transition metals-doped (Ni, Fe and Co) ZnS nanostructure. The chapter consists of various methods used to synthesize undoped and transition metals-doped ZnS nanostructures. These techniques include chemical synthesis routes like, low temperature solvothermal/hydrothermal, reflux technique and chemical precipitation, leading to the different morphology of nanostructures e.g. nanoparticles and nanorods. Characterizations techniques used include transmission electron microscope (TEM), X-ray diffraction (XRD), energy dispersive spectroscopy (EDS), UV-Visible spectroscopy (UV-Vis.), photoluminescence spectroscopy (PL) and vibrating sample magnetometer (VSM).

**Chapter 3** includes the detailed results and discussions of transition metals-doped ZnS nanostructures. The various results obtained using the characterization techniques such as TEM, HRTEM, XRD, UV-Vis., PL, and VSM were done with minute details. The chapter starts with

the analysis of transition metal-doped nanoparticles. Later part of the chapter consists of analysis of the corresponding nanorods.

**Chapter 4** summarizes the results of present thesis work. The summary of main results, in case of nanoparticles as well as nanorods, has been given along with an insight into the future scope of the present research work.

# Chapter 1

# Introduction

# Chapter 1

# Introduction

*This chapter starts with a brief introduction of nanotechnology, quantum confinement and dilute magnetic semiconductors (DMS). Different mechanisms, responsible for the inculcation of magnetic behaviour in host semiconductors, when doped with transition metals atoms, have been discussed briefly. A detailed literature review has been presented to give the idea of background of ZnS based DMS. Potential of ZnS as DMS material and ferromagnetic transition metals, Fe, Co, and Ni have been introduced briefly at the end of chapter.*

## 1.1 Nanotechnology

Since the inception of human race, man is developing different novel techniques to make his life better in all aspects. In this realm, nanotechnology is the newest among the various techniques, which are proving to be useful in all circles of life. Nanotechnology is the study and manipulation of materials, devices, and systems at the nanoscale. The prefix '*nano'* in the word 'nanotechnology' means *'dwarf'*, indicating that nanotechnology is science of miniatures. One nanometer (nm) i.e. $10^{-9}$ m is one billionth part of one meter and materials, which fall under this regime having at least one dimension in 1-100 nm, are known as nanomaterials. These nanomaterials are the cluster of few atoms, just equal to or greater than the size of a molecule. The nanomaterials may be natural or manmade. Many nanomaterials observed in nature include DNA, viruses, natural colloids, colourful dust on butterfly wings, coating on lotus flower and bottom area of gecko feet etc. – just to name a few. The popular man made nanomaterials include quantum dots, quantum rods, nanotubes and quantum wells. To have an idea of

nanoscale, some of the objects encountered in nature and daily life have been compared on nanometer scale as shown in Figure 1.1.

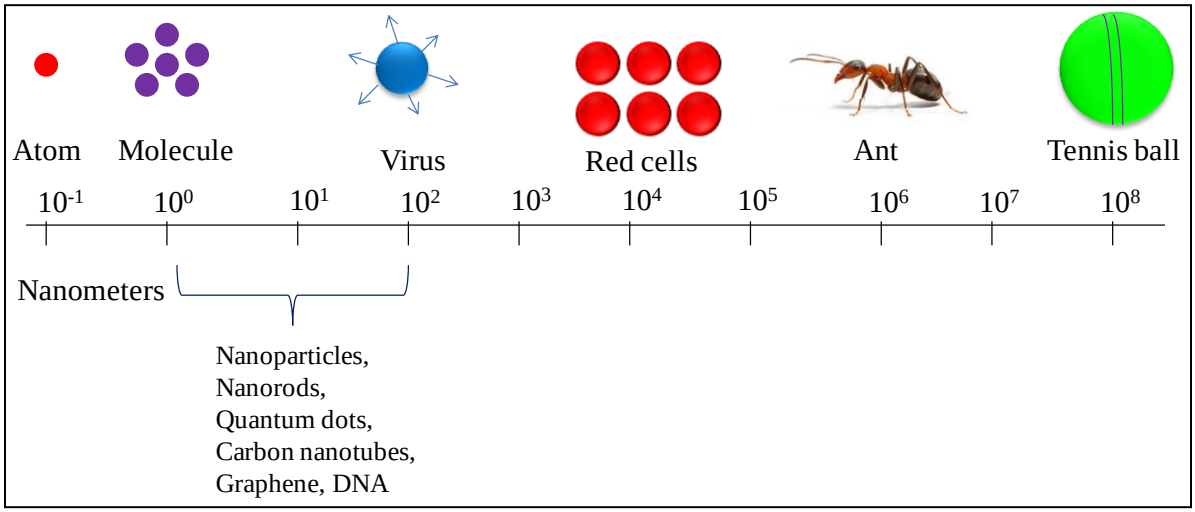


**Figure 1.1** A comparative view of different commonly known objects on nanometer scale

It has been proposed that nanotechnology is used since ancient times. It was the popular lecture *"There's Plenty of Room at the Bottom"* by Professor Richards Feynman at American Physical Society meeting in 1959 which gave impetus to realize the power of nanoscale among the scientific fraternity [1]. The word nanotechnology was first introduced by Norio Taniguchi in 1974. Later in 1980s, Drexler made this term more popular by analysing the molecular motors and robots at nanoscale, claiming it as the engineering of functional systems at molecular scale [2]. In 1981, Binning and Rohrer invented scanning tunneling microscope (STM), which was followed by development of other scanning probe microscopes, like atomic force microscope (AFM). However, the powerful high resolution instruments i.e. scanning electron microscope (SEM) and transmission electron microscope (TEM) were developed in early 1930s. These microscopic tools are indispensable in nanoscale analysis. In addition to these, new semiconducting nanoparticles, popularly known as quantum dots, were discovered in the same period. In 1990s, the miraculous nanomaterials such as Buckyballs by Richard E. Smalley and

carbon nanotubes (CNTs) by Sumio Iijima were discovered which offered plethora of applications in different fields. In 1994, first report on zinc sulphide (ZnS)-based DMS at nanoscale was also realized with manganese-doped ZnS semiconductor. Since early 2000s, many other novel nanomaterials and their applications are under development [3-6]. Many regulations and policies are being framed regarding the safety of using nanomaterials in different areas all over the world [7].

**1.2 Quantum confinement**

Surface area to volume ratio and quantum confinement are two important parameters of nanomaterials, which play a major role in altering their properties at nanoscale. These nanomaterials may be zero dimensional (0-D), one dimensional (1-D), and two dimensional (2-D). In 0-D nanostructures the particles are confined in three dimensions, in 1-D nanostructures the particles are free to move in one dimension but their motion is restricted in remaining two dimensions. In 2-D nanostructures, the particles are free to move in two dimensions but their motion is confined in remaining third dimension. The confinement in the motion of a particle is termed as *quantum confinement*, which, in turn, alters the properties of nanostructures as compared to their bulk counterparts as can be analyzed from the density of states' plots shown in Figure 1.2. The discreteness in density of states depends upon the dimensionality of the nanostructures. From these plots, one can easily estimate different electronic and optical properties of the materials at nanoscale based upon the dimensionality of materials. The examples of 0-D nanostructures are- quantum dots, nanoparticles and nanodots. Carbon nanotubes, nanorods and nanowires etc. are the examples of 1-D nanostructures. 2-D nanostructures include graphene, ultra thin films, nanosheets and nanoribbons. Due to their

increased surface area to volume ratio, the researchers, all around the world, are working on different aspects of nanostructures to exploit their properties.

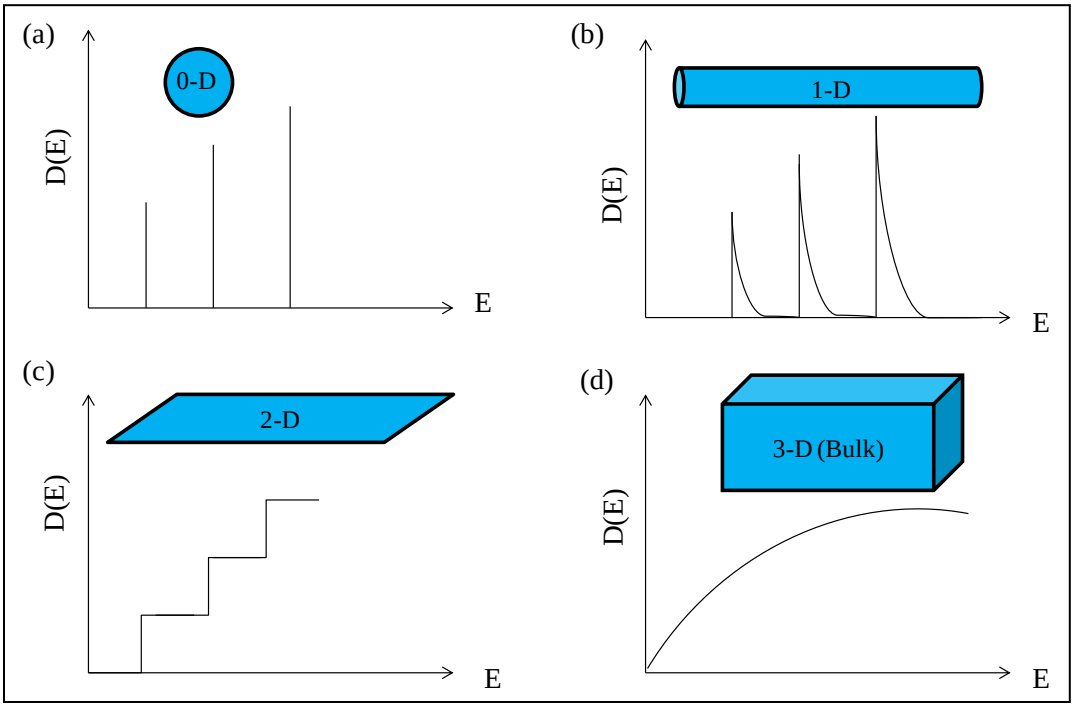


**Figure 1.2** Energy verses density of states plots of (a) 0-D (b) 1-D (c) 2-D (d) 3-D structures

### 1.3 Dilute magnetic semiconductors

Semiconductor industry is growing with fast pace with new developments. In modern era, the development of multifunctional materials is the need of hour in semiconductor industry as we are heading towards the collapse of Moore's law [8]. A lot has been achieved to save Moore's predictions but much more can be done for its sustainability for long time. Modern research is heading towards exploiting novel multifunctional materials, which can give multiple functionalities as a single entity. One possible solution to tackle this severe problem is using the nanostructured materials so that more and more transistors could be assembled on a single chip. Another aspect to tackle this problem is the doping of the host semiconductors with a small amount of guest transition metals or rare earth metals, which develop a novel class of materials

popularly known as dilute magnetic semiconductors (DMS). Figure 1.3(a) represents a non-magnetic host semiconductor, which is doped with guest transition metals atoms, indicated with red circles in figure 1.3 (b).

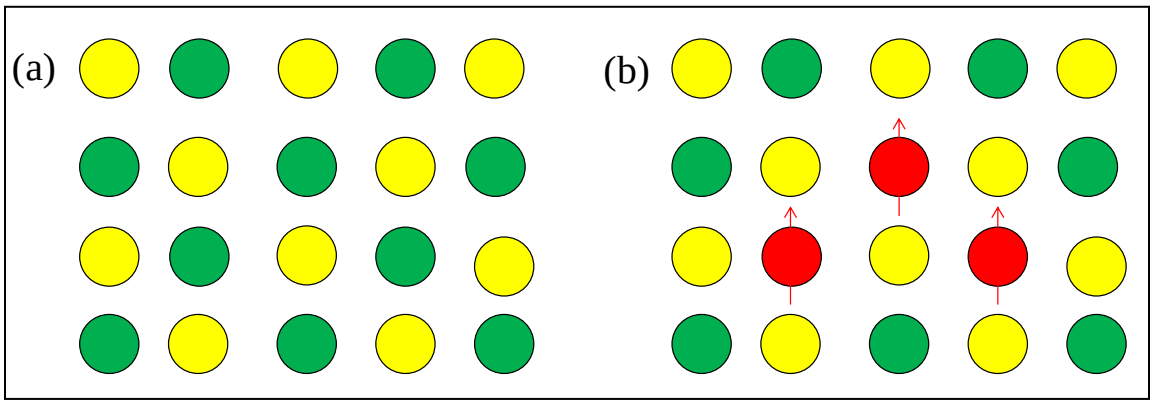


**Figure 1.3** Pictorial representation of (a) non-magnetic host semiconductor material and (b) doped semiconductor material (red circles with arrow mark represent doped magnetic ions)

The main advantage of using DMS materials is to make use of the net spin of the doped atoms along with the charge leading to development of spin-controlled electronics, popularly known as spintronics. Spintronics is composed of two words- spin and electronics. It includes study of spin freedom of the electrons. The spintronics exploits the spin of electron in addition to the charge. The main advantage of DMS is that their properties can be altered by varying the dopant concentration in the host semiconductor. Such materials can have applications in light emitting diodes, spintronics devices, band-gap engineering devices, field detectors, lasers, magnetic resonance imaging (MRI) [9-13]. DMS materaisl have been projected as potential candidate for solar cells applications. It is known that long excited state lifetimes in the intermediate levels are necessary for photovoltaic conversion, as the long excited lifetimes improve the chances of photo-generated carriers to be promoted to conduction band. The conventional inorganic semiconductors do not have a straightforward equivalent long lifetime spin states as in these semiconductors one always finds free carriers with both spin states for which recombination is

readily allowed. However, DMS may exhibit such properties. Hence, the use of ferromagnetic DMS to mimic the triplet states in bulk inorganic semiconductors for photovoltaic power conversion has been proposed in recent time [14].

The substitution of ferromagnetic ions in the host semiconductors may also help in data storage and quantum computers. In current times, the main challenge in development of future technologies is the fabrication of spin controlled devices, so DMS are building blocks for the future electronics industry. During the last few years, scientific community has shown keen interest in the studies of impurity induced materials, including II-VI and III-V semiconductors in addition to other semiconductor materials [15-18].

Current semiconductor technology alters the conductivity of the semiconductor with the doping of external agents, which may cause change in the magnetic, optical, and other properties of the host semiconductor. DMS dependent devices will be based on spin degree of freedom that will increase the storage capacity of future semiconductor devices. The spin can induce new functionalities in the Spintronics devices which have no analogue in today's semiconductor devices [19]. Realizing the DMS at nanoscale can have great impact on current semiconductor technology because these may be the indispensable tool for the Moore's law survival. In recent times, in addition to bulk compounds, attempts have been made to study the magnetism at nanoscale in various compounds. At nanoscale the advantage of quantum confinement effects can be clubbed with impact of doping of host semiconductor, which would pave the path of versatile future spintronics devices [20-25]. Such devices will lead to the realization of altered magnetic optical and electronic properties which will be the beginning of a new chapter in the future electronics industry.

### 1.4 Mechanisms involved in DMS

In DMS, the magnetic and optical properties are altered with doping of very small amount of guest metals in host semiconductor; hence, understanding the interactions between guest metal and host semiconductor is of utmost importance. Although, the origin of the magnetism in DMS is a peculiar issue; however, some theoretical models have been predicted to justify the magnetic origin in these materials [26]. Some of these theoretical models are summarized below:

#### 1.4.1 The Zener model

This model was presented by Zener in 1951 [27]. It explains the origin of magnetism due to the direct and indirect super exchange interactions. The direct interaction involves the exchange between half filled d-electrons of the transition metals and fully filled p-orbitals of anion. The interaction leads to antiferromagnetic coupling of nearest neighbour transition metal cation through a shared anion as represented in Figure 1.4(a).

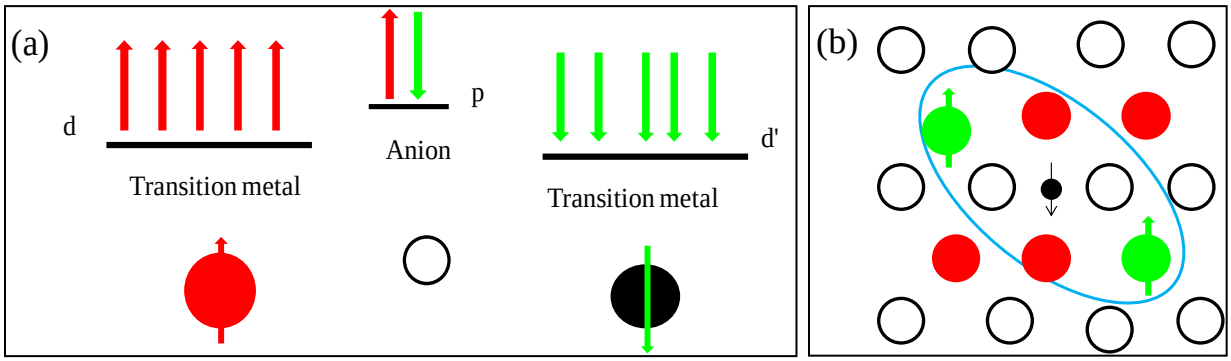


**Figure 1.4** Zener model (a) direct super exchange mechanism indicating coupling through shared anion represented with black circle (b) Indirect super exchange mechanism indicating coupling through conduction electron represented with small dot with spin down.

Whereas, indirect exchange involves the interaction between half filled d-electrons of the transition metals cations mediated by the band carriers which tends to align the half filled spin in ferromagnetic manner as indicated in Figure 1.4(b). According to Zener model the

ferromagnetism is induced only if the indirect exchange dominates over its direct counterpart. In general the direct exchange mechanism dominates at lower distance between the moments, whereas, indirect exchange mechanism works at large distances and super-exchange is effective when the moments are too far away from each other.

### 1.4.2 Ruderman-Kittel-Kasuya-Yosida (RKKY) model

RKKY model elaborates the magnetic interaction between magnetic ions and delocalized conduction band electrons [28, 29]. In this type of interaction the conduction electron in the close vicinity of the magnetic ion gets magnetized, which influences the polarization of neighboring ions which decays in oscillatory manner. The oscillations can have ferromagnetic or antiferromagnetic type of exchange coupling on the basis of the separation of doped magnetic ions. RKKY model predicts that such interaction dominates at high concentration of delocalized carriers in the host material.

### 1.4.3 The mean-field Zener model

This model was suggested by Dietl et al. [30] and it is based on indirect super exchange interaction as suggested by Zener model. Such an interaction is generally mediated by holes which mediate RKKY type of interaction between the doped transition metal ions leading to ferromagnetism. Dietl et al. explained the experimentally observed Curie temperature, $T_c$, values for Mn doped GaAs and ZnTe.

### 1.4.4 Bound magnetic polaron (BMP)

In this mechanism, a magnetization cloud, popularly known as BMP, is formed during the exchange interaction of electrons or holes in the vicinity of the dopant ion in the host. When such BMPs are large in number, they get overlap with their immediate neighbors leading to a long

range ferromagnetic ordering in DMS. Coey et al. [31] have presented a BMP model in oxides DMS as shown in Figure 1.5.

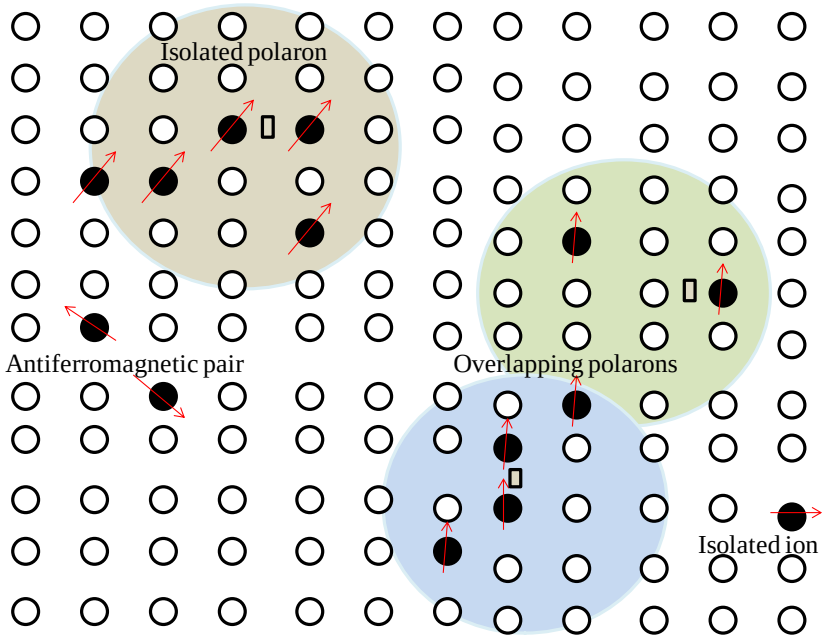


**Figure 1.5** Schematic representation of bound magnetic polaron in DMS.

Smaller circles show cation of host semiconductor and rectangles indicate the vacancies. The circles with arrow marks are doped magnetic ions. The vacancies in the host semiconductor trap the charge carriers and the magnetic ions interact through the trapped charge carriers, which give rise to an effective magnetic field. This causes the alignment of the neighboring charge carriers in their direction which leads to formation of bound polarons. These bound polarons may overlap with each other giving rise to ferromagnetic ordering in the DMS.

## 1.5 Literature review

To get a comprehensive idea about the ZnS based DMS, a deep literature review has been presented.

As far as the use of transition metals in semiconductors is concerned, the first report on bulk multifunctional materials dates back to 1866 when the luminescence properties of ZnS:Cu were

analyzed [32]. It was observed that the phosphorescence is due to the presence of Cu in ZnS. Later in 1920s, Cu incorporated ZnS has been used to obtain green luminescence [33]. During 1960s and 1970s, the semiconductors magnetic research was focussed on the compounds such as EuS, NiO, polymers, ferrites and few complex systems e.g. MnSb, CdCr2S4, SeCuO3, MnAs [34]. The term DMS was first coined around 1978 by the Scientist Robert R. Galazka at 14$^{th}$ International Conference on Physics of Semiconductors. Galazka et al. studied the magneto-optical properties of various II-VI alloys; however, the observed Curie temperature ($T_c$) was very low [35]. Furdyna et al. in 1982 explored the semiconducting and magnetic properties of Mn incorporated CdTe and HgTe alloys. The spin-spin exchange interactions were found in the magnetic ions and band electrons of the semiconductors. They later extended their studies to other $A^{II}_{1-x}Mn_xB^{IV}$ type DMS materials [9, 36-37].

During the 1980s, the main focus of research was on III-V, II-IV and II-VI group compounds. Group III-V DMS include, (In, Mn)As, (Ga, Mn)As, (Ga, Mn)N whereas II-VI DMS includes (Zn,Mn)Te, (Zn,Mn)Se, (Cd,Mn)Te, (Cd,Mn)Se [38-41]. The II-IV DMS materials include (Pb,MnSb)Te, (Pb,Mn)Te. Of these DMS, II-VI group are considered the potential candidates for the advanced applications in optoelectronic devices. The popular compounds of this group include CdS, ZnS, ZnSe, CdSe, CdTe, ZnO and ZnTe etc. These materials are generally doped with transition metals and rare earth metals. These doped materials, presenting either spin glass behaviour or weak ferromagnetism, with very low $T_c$, therefore, considered inadequate for applications requiring ferromagnetic order at room temperature when in bulk form. The obvious choice was to exploit these materials at nanoscale to remove the abnormalities weak ferromagnetism and low Curie temperatures. Since last two decades a tremendous research on studying these DMS at nanoscale has been fascinating the scientific fraternity. Many reports are

available on the transition metals incorporated semiconductors based DMS. Various reports are available on DMS nanostructures of CdS, CdSe, ZnS, ZnO, ZnTe, ZnSe, $SnO_2$ and other II-IV semiconductor materials doped with various transition metals [42-64]. Among these semiconductors, ZnS could be a potential candidate as DMS material. ZnS, due to its wide band gap, can offer enormous possibilities in spintronics based devices. It was in 1994 when the first Mn-doped ZnS nanocrystals, synthesized by Bhargawa et al., encouraged scientific community to explore the optical and magnetic properties of ZnS based DMS materials at nanoscale [65]. It was proposed that $Mn^{2+}$ doped ZnS nanosemiconductor could give high quantum luminescence efficiency and lifetime shortening simultanously [66]. Since then, there have been a lot of studies on the various properties of the doped ZnS nanostructures. Although the photoluminescence studies are main focus in studying the properties of these nanostructures, but in recent times few efforts have been made in studying the magnetic properties of transition metals doped ZnS nanostructures. Some reports on magnetic studies of transition metal doped ZnS nanostructures were found during the literature review.

Tsujii et al. in 2003 [67] studied the magnetism induced in Mn and Eu incorporated ZnS nanocrystals. The studies reveal that most of the Mn ions coordinate with each other on the surface of the nanocrystals, and the amount of Mn doped inside the nanocrystals does not exceed one per nanocrystals in the matrix. Low-temperature magnetization indicates the absence of antiferromagnetic interaction between Mn ions, in contrast to the bulk materials.

Yuan et al. in 2004 [68] studied synthesis, optical, and magnetic properties of $Zn_{1-x}Mn_xS$ nanowires (x = 13.6). Two PL emission bands were observed at 503 and 570 nm. The peak at around 503 nm was attributed to the recombination of free charge carreiers at defect sites on the surface of ZnS, whereas the peak at 570 nm was attributed to $Mn2^{+}$. In this study, magnetization

was measured against temperature during cooling in an applied magnetic field of 500 Oe for the ZnS: Mn nanowires. The results indicate that the Mn doped ZnS nanowires have paramagnetic behaviour.

Biswas et al. in 2005 [69] reported optical and magnetic properties of Mn-doped (Mn = 0-20%) ZnS nanorods. It has been observed that Mn insertion in the ZnS matrix causes a phase change from hexagonal wurtzite to cubic zinc blende structure. Electron paramagnetic resonance (EPR) results support the presence of magnetic dipole interaction for the Mn-incorporated ZnS nanorods with a higher Mn concentration.

Kar et al. in 2006 [70] studied the magnetic properties of $Mn_xZn_{1-x}S$ nanorods synthesized by solvothermal method. Highly intense orange emission at 585 nm was obtained from the $Mn_xZn_{1-x}S$ nanorods. Maximum intensity was obtained for 1 atomic% Mn-doped ZnS nanorods. Six hyperfine lines EPR spectra was obtained for the lower Mn content ZnS nanorods, whereas a single line spectra were observed for higher Mn contents, indicating the formation of Mn clusters at higher Mn concentrations.

Bhattacharya et al. in 2007 [71] studied electrical and magnetic properties of Fe-doped (1-5%) ZnS nanoparticles having size ~3 nm. A regular increase in magnetization was observed in case of 5% doped samples as the temperature is lowered. Magnetization studies at low temperature indicate a ferromagnetic behaviour resulting in 1-D magnetic system having anti-parallel spin alignment.

Wang et al. in 2007 [72] reported the cluster spin-glasslike behaviour of Mn doped ZnS DMS. $Zn_{1-x}Mn_{xS}$ nanoparticles (x = 0.008, 0.16, and 0.32), synthesized by a co-precipitation method. The magnetic properties of the $Zn_{1-x}Mn_{xS}$ nanoparticles were analyzed using alternating-current (ac) susceptibility and direct-current magnetization measurements. For the $Zn_{0.68}Mn_{0.32}S$

nanoparticles, there was strong evidence for appearance of cluster spin-glasslike behaviour, indicated by two maxima at 15 and 25 K in temperature dependence of ac susceptibility. The frequency independence of the peak observed at higher temperature is termed due to intra-cluster ferromagnetic (FM) interactions, and the frequency dependence of the peak at lower temperature is related with the spin glass.

Sarkar et al. in 2007 [73] reported ferromagnetism induced in ZnS nanocrystals and the effect of Mn concentration (Mn = 1.5%, 2.5%, 3.5%, and 6%) on the ferromagnetic behaviour of the ZnS. Magnetic studies were carried out up to 7 T. Ferromagnetic ordering and giant Zeeman splitting are observed below 30 K in these nanoparticles for doping above 1.5%. Samples having Mn concentration above 1.5% showed hysteresis, and detailed investigation confirmed the existence of ferromagnetism in these ZnS nanocrystallites having 2.5%, 3.5%, and 6% Mn doping. The 1.5% doped sample showed paramagnetism down to 2 K. The values of blocking temperature $T_B$ and $H_C$ are found to be maximized for a doping level of 2.5%.

Sambavisham et al. in 2008 [74] reported the magnetism in Fe-doped ZnS nanoparticles. Nanoparticles of $Zn_{1-x}Co_xS$ with x = 0.00, 0.1, 0.2, 0.4 and 0.6, synthesized by chemical co-precipitation method. The optical absorption studies exhibit a blue shift in absorption edge with increased Fe doping. The undoped ZnS samples indicate diamagnetic behaviour, whereas, x = 0.10 and 0.2, Fe-doped ZnS samples exhibit a weak ferromagnetism behaviour termed as superparamagnetic behaviour indicating with partially resolved hysteresis loop.

Kang et al. in 2009 [75] studied synthesis and magnetic properties of single-crystalline Mn and Fe-doped and cobalt doped ZnS nanowires and nanobelts. Strong emission bands were found from photoluminescence spectra of Mn/Fe-doped and Co doped ZnS nanowires. The M-H curves were measured at 5 and 300 K. The magnetic hysteresis loops were seen at both temperatures,

indicating that these ZnS nanostructures are ferromagnetic at room temperature. Fe doped ZnS nanowires exhibit the largest magnetization value. The magnetic property measurements show that the Curie temperature is above the room temperature.

Sambavisham et al. in 2009 [76] reported induced magnetism in Co doped ZnS nanoparticles. $Zn_{1-x}Co_xS$ nanoparticles with x = 0, 0.1, 0.2, and 0.3 were obtained by the co-precipitation method. In the Co doped samples, room-temperature magnetic hysteresis loop is observed and the magnetization reducesas the cobalt content is increased. However, these samples indicate paramagnetic behaviour instead of ferromagnetic at both 300 and 80 K, suggesting that the origin of room temperature magnetization in these cobalt doped ZnS nanoparticles involves the antiferromagnetic interactions.

Li et al. in 2010 [77] reported the computational studies on magnetic properties of Cr-doped ZnS nanowires. At a doping concentration of 2.08%, the Cr atom prefers to substitute for the Zn atom in the bunch of the ZnS nanowires having diameter of 1.2 nm; at a higher doping concentration of 4.17%, the Cr atoms preferably substitute for Zn atom and its neighbouring surface three-coordinated Zn atom. I as been observed that Cr atoms in ZnS nanowires are always ferromagnetically coupled to each other and antiferromagnetically coupled to the mediating sulphur atoms; moreover, the ferromagnetism is not sensitive to surface passivation. The ferromagnetism in Cr-doped ZnS nanowires is associated to a double-exchange mechanism.

Chen et al. in 2011 [78] presented first-principles studies to show the comparative study on the magnetic properties of ZnS nanowires doped with different transition metal atoms. ZnS nanowires doped with one or two transition-metal atoms simultaneously. The results indicate that the doped transition metal atoms prefer to be at the middle position of the nanowires and have no tendency to form clusters. It was reported that the formation energies of transition metals doped

nanowires were smaller than that of the pure counterparts, showing that doping process is an exothermic type of reaction. The Cr atoms induced antiferromagnetic (AFM) interactions, whereas Mn, Fe, Co, and Ni atoms induced ferromagnetic (FM) interactions between the surrounding Zn and S atoms of the host semiconductor.

Eryong et al. in 2011 [79] reported optical and magnetic properties of Fe-doped (x = 0.00, 0.1 and 0.2) ZnS nanoparticles synthesized chemical co-precipitation technique. It was concluded that Fe doping did not create new energy bands or defect states in ZnS, but reduced the intensity of PL peaks. The M–H curves analyzed at 5 K and 300 K, respectively, indicate no remanence or coercive force. This phenomenon indicates that the $Zn_{1-x}Fe_xS$ (x = 0.10) nano-particles are superparamagnetic.

Owens et al. in 2011 [80] reported high temperature magnetic order in ZnS doped with Cu. Ferromagnetic resonance (FMR) study shows non-zero absorption above room temperature indicating a high value of Curie temperature. Field-cooled and zero-field-cooled magnetization data indicate a bifurcation at about 300 K. The muon spin rotation measurements confirm highly non-uniform magnetic order. It was shown that about 25% of the sample volume fraction exhibits strong magnetism.

Reddy et al. in 2011 [81] reported room temperature ferromagnetism in EDTA capped Cr-doped ZnS nanoparticles. The results indicate that ZnS nanoparticles with lower Cr concentration exhibited strong ferromagnetism, but at higher Cr concentrations the ferromagnetism was found suppressed. The EPR spectra of the nanocrystals showed the resonance of electron centres with a *g*-value of 1.989. The signal intensity and line width of the EPR signal increased with increasing Cr concentrations. Magnetic studies indicate decrease in ferromagnetism with increase in

annealing temperature, supposed due to appreciable variation in structural defects which are sensitive to the annealing temperature.

Reddy et al. in 2012 [82] studied structural, optical and magnetic properties of $Zn_{0.97-x}Cu_xCr_{0.03}S$ (x = 0.000, 0.01, 0.02, 0.03, 0.04 and 0.05) nanoparticles. It was predicted that doped Cr and Cu atoms were inserted at the Zn sites in the cubic structure without altering the original ZnS matrix. As the dopant concentration is increased, a strong quenching in PL intensity is reported. PL emission peak indicated a red shift at increased Cu concentration. Magnetization studies showed that Cu and Cr co-doping cause enhanced the room temperature ferromagnetism.

Reddy et al. in 2012 [83] studied the annealing temperature effect on optical and magnetic properties of Cr incorporated ZnS nanoparticles. Photoluminescence studies of Cr-doped ZnS nanoparticles showed that the emission wavelength in 440–675 nm range is tunable with annealing temperature. Magnetic studies indicated decrease in ferromagnetism with increased annealing temperature, predicted due to change in structural defects sensitive to annealing temperature.

Senthilkumaar et al. in 2012 [84] studied the synthesis and magnetic properties of Mn-doped ZnS nanorods synthesized via chemical route with mercaptoethanol as surfactant. The magnetic studies at room temperature predicted paramagnetic behaviour for the doped nanorods. The observations showed that Mn ions existed mainly as a single impurity and no Mn–Mn clusters or pairs were observed and hence no antiferromagnetic behaviour in doped ZnS nanorods was indicated.

Ragam et al. in 2012 [85] reported ferromagnetism induced in $Mn_xZn_{1-x}S$ (x = 0.000-0.07) nanoparticles at room temperature. From M-H measurements, it was seen that ZnS nanoparticles exhibit ferromagnetism at 4 K temperature and $Mn_xZn_{1-x}S$ with x = 0.05 and 0.07 exhibit

ferromagnetism at room temperature. The possibility of the ferromagnetism was predicted due to defects at the surface of the nanoparticles.

Rozale et al. in 2012 [86] reported ferromagnetism induced in Eu-doped ZnS nanocrystals via density functional theory (DFT) and presented a mechanism of ferromagnetism induced in the ZnS nanocrystals when doped appropriately with rare earth elements. It is found that with insertion of Eu in ZnS matrix, a new localized band is found between valence and conduction bands corresponding to the majority spin of Eu-4f states. $Zn_{1-x}Eu_xS$ (x = 0.000, 0.25, 0.5 and 0.75) nanostructures exhibit a half-metallic feature and it was concluded that the emerged ferromagnetic state is more probable in energy as compared to the antiferromagnetic state.

Patel et al. in 2012 [87] studied the impact of swift heavy ions (SHI) on the magnetic behaviour of cobalt doped ZnS thin films in which the Co ions were substituted on Zn sites. The doped materials were synthesized using pulsed laser deposition technique on the substrates held at high temperature of 600 $^{\circ}$C for obtaining films having wurtzite crystal structure and it showed ferromagnetic ordering up to room temperature with some paramagnetic component. The higher order correlation between paramagnetic spins on Co ions was diminished by ions irradiation and the doped ZnS films were found to be purely paramagnetic in nature. This effect was ascribed due to the formation of cylindrical ion tracks resulted due to the thermal spikes obtained from electron and phonon coupling.

Kumar et al. in 2013 [88] reported room temperature ferromagnetism inculcated in chemical co-precipitation technique synthesized $Zn_{1-x}Ni_xS$ nanoparticles with x = 0.01, 0.03 and 0.05. The ZnS nanoparticles at lower Ni concentration indicated saturated M-H hysteresis loop at room temperature with ferromagnetic behaviour, but at higher Ni concentrations no such behaviour was observed which confirm the intrinsic nature of the ferromagnetism at smaller Ni-doping.

Wei et al. in 2013 [89] reported the structure and room temperature ferromagnetism induced in copper doped ZnS nanoparticles. Cu-doped ZnS nanoparticles synthesized via solvothermal technique found to have diameters of 10–20 nm and cubic zinc blende structure. The Cu ions were incorporated into the ZnS lattice and the maximum concentration of the Cu ions reported in the ZnS nanoparticles was 2.84%. The ferromagnetism induced in Cu-doped ZnS nanoparticles was observed at room temperature, was attributed to the super-exchange mechanism.

Patel et al. in 2014 [90], analyzed surfactant assisted Fe doped nanocrystals. It was predicted that the magnetization increases to an optimum level with increase of Fe concentration up to 0.08. Increase in Fe concentration lead the decrease in magnetization. The decrease in ferromagnetism at higher concentration has been correlated with antiferromagnetic interaction between Fe-Fe ions.

Fang et al. in 2014 [91], studied the room temperature ferromagnetism induced with Co-doping in ZnS nanoparticles using first principle calculations. It was proposed that the induced ferromagnetism is due to antiferromagnetic coupling of Co–S–Co and the ferromagnetic coupling of Co–S–Zn–S–Co attributed to *p–d* hybridization interaction and RKKY interaction.

Zhang et al. studied in 2014 [92], the $H^+$-mediated ferromagnetism in Co-Doped ZnS wurtzite nanoparticles of size ~4 nm. It was concluded that the interstitial $H^+$ ions in ZnS matrix may have provided the efficient ferromagnetic order between the neighboring $Co^{2+}$ ions.

In a very recent study, Yang et al. in 2015 [93], reported the room temperature ferromagnetism induced in Co incorporated ZnS nanorods. The cobalt doped ZnS nanorods exhibited the room temperature ferromagnetic behaviour and the magnetic saturation in M-H curves was found increased as the Co doping ratio is increased.

From above discussion, it is clear that with the introduction of transition metals in ZnS nanostructures, ferromagnetism is induced in ZnS nanostructures. Most of the reports on transition metals-doped ZnS nanostructures are focused on photoluminescence studies and some efforts have been made on magnetic studies of transition metals-doped ZnS nanostructures, separately. These include room temperature ferromagntic studies by Zhang et al. in which the saturation magnetization has been found increased with increased annealing temperature [94]. Peng et al. and Shan et al. observed the magnetism in undoped ZnO and ZnS nanostructures [95-96]. Sarkar et al. have reported the suppression in magnetic field dependent photoluminescence in Mn-doped ZnS nanocrystals [97]. Wei et al. reported the the quenching in ZnS nanowires photoluminescence due to Fe doping [98]. Goktas et al. observed the paramagnetism at 5K and ferromagnetism at 300K in Mn-doped ZnS nanorods [99]. Besides these, some other reports on optical properties of doped ZnS nanostrutcures were also observed in literature. [100-113]. In this work, we have tried to unite both studies, optical as well as magnetic, along with the structural properties, so as to exploit ZnS as potential DMS material in future electronics.

**1.6 ZnS as potential DMS material**

ZnS is a popular semiconductor compound of II-VI group. It is an inorganic compound having chemical formula ZnS consisting of Zn and S atoms. ZnS has been used as phosphor and as pigment in many applications. It can be doped as p-type as well as n-type semiconductor. The wide band gap, 3.6 eV, of ZnS provides ample opportunities to tune its band gap at nanoscale. The properties of ZnS can be engineered to greater extent by inserting transition metals in ZnS matrix, creating new energy levels in the ZnS band gap. Ever since the first report on Mn-doped ZnS nanoparticles there has been a great interest in the ZnS based DMS materials research. It can be used in various applications all forms i.e. 0-D in the form of ZnS quantum dots, 1-D in form

of ZnS nanorods or nanowires form or as 2-D films, all giving unique optical and magnetic properties. Meng et al. studied the properties of ZnS nanowires grown on silicon substrate [114]. Cao et al. reported the decrease in particle size as the Mn-doping concentration is increased but the peak intensity was found increased with Mn doping and maximum intensity was reported at 3% Mn [115]. Yang etl al. observed strong green luminescence in $Ni^{2+}$ -doped ZnS nanocrystals [116]. Karar et al. reported enhancement in Mn doped ZnS nanocrystals [117]. Quan et al. reported that emission intensity is Mn dependent due to the enrgy transfer from host ZnS to Mn [118]. Kumar et al. studied the reflective characteristics of Ni-doped ZnS nanoparticle-pigment and their coatings [119]. Dinsmore et al reported the light emitting properties of Mn-doped ZnS nanoparticles at annealing temperature of 525 °C and observed a dramatic increase in cathodoluminescence emission [120]. Chauhan et al. reported then catalytic activities of the Cu doped ZnS nanoparticles. It was reported that Cu doped ZnS bleaches methylene blue much faster than its undoped counterpart when exposed to visible light as compared with ultraviolet light [121]. Some other reports on properties of doped ZnS nanostructures have also been observed in literarature [122-132].

### 1.6.1 Structure of ZnS

The structure of ZnS comprises zinc (Zn) and sulphur (S) atoms. The size of the Zn cation is smaller as compared to the S anion. The S atoms form face centered cubic (fcc) structure. All these S atoms form a tetrahedron within the unit cell. Each of the Zn atoms are surrounded by four S neighbouring atoms indicating a co-ordination number as 4. Generally, ZnS exhibits two types of structures namely- cubic and wurtzite as shown in Figure 1.6. Cubic structure is more stable than wurtzite counterpart.

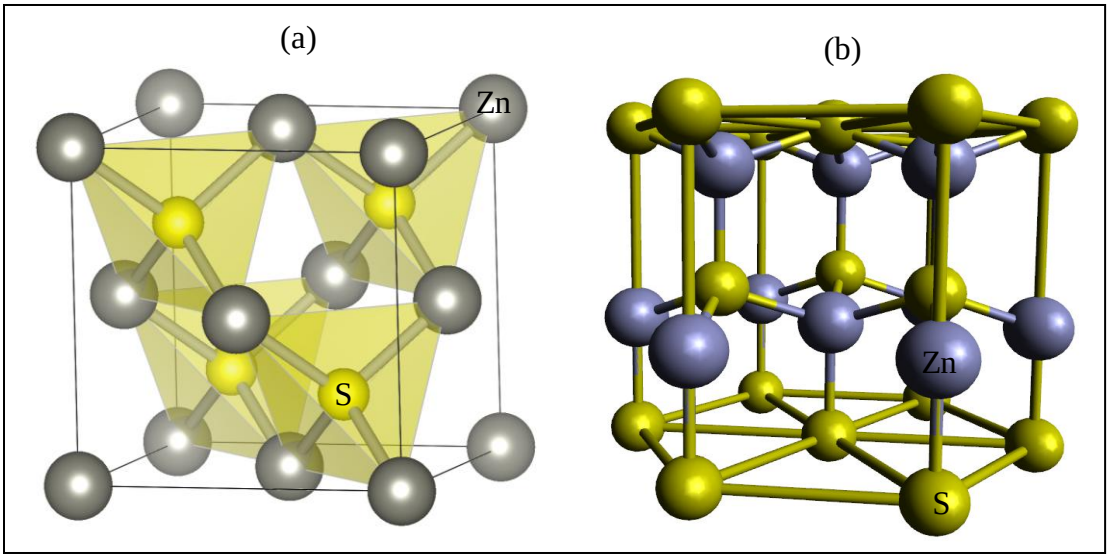


**Figure 1.6** Unit cell structure of ZnS (a) cubic and (b) wurtzite. [133]

The coordination geometry in both forms of ZnS is tetrahedral. Both forms have different band gaps, cubic form has 3.6 eV and that of wurtzite is 3.8 eV. ZnS has many useful properties associated with it in both forms, some of these are summarised in Table 1.1.

**Table 1.1 General properties of ZnS**

| | |
|---|---|
| **Chemical formula** | ZnS |
| **Molecular weight** | 97.46 |
| **Crystal structure** | Cubic and wurtzite |
| **Lattice constant** | 5.4093 Å (cubic) |
| **Band gap (300 K)** | 3.6 eV (cubic), 3.8 eV (wurtzite) |
| **Thermal conductivity** | 25.01 W/mk |
| **Melting point** | 1850 C |
| **Electron mobility** | 180 $cm^2$/Vs |
| **Hole mobility** | 5 $cm^2$/Vs |
| **Refractive index** | 2.378 (for wurtzite structure with, a = 0.3811 nm and c = |

| | |
|---|---|
| | 0.6234 nm at $\lambda$ = 632 nm) |
| **Toxicity** | Low |
| **Electrical behaviour** | Semiconductor |
| **Magnetic behaviour** | Diamagnetic, magnetic susceptibility $\chi$ = -25 x $10^{-6}$ (cgs). |

Zn and S atoms have the electronic congigurations ($1s^2$, $2s^2$ $2p^6$, $3s^2$, $3p^6$, $3d^{10}$, $4s^2$) and ($1s^2$, $2s^2$ $2p^6$, $3s^2$, $3p^4$), respectively. In ZnS structure, s, p, and d-orbitals take part in bonding, which are completely paired. The ZnS band consists of filled valence and empty conduction bands, as no electron is left unpaired, so ZnS behaves as diamagnetic in nature.

**1.7 Transition metals- iron (Fe), cobalt (Co), and nickel (Ni)**

These are the popular d-block elements in modern periodic table having partially filled *d* sub-shell. The partially filled d sub-shell of these metals makes them suitable in doping of various DMS as will be discussed in literature review. The magnetic behaviour of these metals is ferromagnetic in nature. The atomic radius of Zn ions ($Zn^{2+}$) is ~74 pm, whereas the ionic radii (+2 valence state with coordination number = 6) of transition metals, iron (Fe), cobalt (Co), and nickel (Ni) are 61 pm, 65 pm and 69 pm respectively [134]. Hence, when doping is done, it is expected that when higher ionic radii ions, $Zn^{2+}$, are replaced with lower ionic radii ions e.g. $Fe^{2+}$, $Co^{2+}$, and $Ni^{2+}$ compressive strain will be developed in ZnS lattice. Change in lattice parameters is expected due to the compressive strain in the doped ZnS nanostructures.

## 1.8 Objectives of current thesis

Current thesis work focuses on synthesis of transition metals (Ni, Fe and Co) doped ZnS nanostructures viz., nanoparticles and nanorods, synthesized via chemical route. The synthesized nanostructures have been characterized using TEM, HRTEM, XRD, EDS, UV-Vis., PL spectroscopy, and VSM. The idea is to investigate the changes induced in structural, optical and magnetic behaviour of the transition metals doped ZnS with their respective undoped counterparts at nanoscale.

# Chapter 2

# Synthesis and Characterization

# Chapter 2

# Synthesis and Characterizations

*Synthesis and characterization techniques are integral part of nanomaterials. Synthesis techniques play an important role in deciding the morphology and properties of nanomaterials. Characterization techniques help in determining the morphology and properties of synthesized nanomaterials. The control of certain parameters in various techniques may lead to different geometry of the nanostructures. In this chapter various methods used to synthesize transition metals doped ZnS nanostructures, nanoparticles and nanorods have been described. The techniques used in synthesizing nanostructures are low temperature solvothermal/hydrothermal and chemical precipitation leading to the different morphology of nanostructures. Characterization techniques used include transmission electron microscopy (TEM), X-ray diffraction (XRD), energy dispersive spectroscopy (EDS), UV-visible spectroscopy (UV-Vis), photoluminescence spectroscopy (PL), and vibrating sample magnetometer (VSM) measurement.*

## 2.1 Chemicals used in synthesizing transition metals-doped ZnS nanostructures

Various types of precursors are used in synthesis of transition metals-doped ZnS nanostructures. These are given below:

**Zinc precursors**- Zinc acetate, $Zn(CH_3COO).2H_2O$; Zinc chloride, $ZnCl_2$

**Sulphur precursors**- Sodium sulphide, $Na_2.9H_2O$; Thiourea, $SC(NH_2)_2$

**Transition metals precursors**- Nickel chloride, $NiCl_2$; Iron chloride, $FeCl_3$; Cobalt chloride, $CoCl_2$.

**Solvents**- De-ionized water, methanol, ethanol, ethylenediamine (EN), ethylene glycol, sodium hydroxide

### 2.2 Transition metals doping concentrations used to doped ZnS nanostructures

Following transition materials with at given concentrations were used to synthesize doped ZnS nanoparticles and nanorods:

- **Doped ZnS nanoparticles**

  Ni-doped ZnS nanoparticles, $Zn_{1-x}Ni_xS$, where x = 0.00, 0.01, 0.05 and 0.10.

  Fe-doped ZnS nanoparticles, $Zn_{1-x}Fe_xS$, where x = 0.00, 0.01, 0.05 and 0.10.

  Co-doped ZnS nanoparticles, $Zn_{1-x}Co_xS$, where x = 0.00, 0.01, 0.05 and 0.10.

- **Doped ZnS nanorods**

  Ni-doped ZnS nanorods, $Zn_{1-x}Ni_xS$, where x = 0.00, 0.01, 0.05 and 0.10.

  Fe-doped ZnS nanorods, $Zn_{1-x}Fe_xS$, where x = 0.00, 0.01, 0.05 and 0.10.

  Co-doped ZnS nanorods, $Zn_{1-x}Co_xS$, where x = 0.00, 0.01, 0.05 and 0.10.

### 2.3 Synthesis of ZnS nanostructures

Generally an ideal technique used to synthesize nanostructures is the one, which gives high quality nanostructures with minimum impurities and, of course, such a technique should be facile and environment friendly. There are wide varieties of techniques available in literature generally used to synthesize ZnS nanostructures. These techniques include chemical co-precipitation [135], thermal decomposition [136], sol-gel [137], low temperature solvothermal/hydrothermal techniques [138], molecular-beam-epitaxy [139] and refluxed technique [140]. These methods can be used to synthesize various nanostructures including, nanoparticles, nanorods, nanosheets, nano-flowers and other nanostructures [141-155]. Among these techniques, the chemical

synthesis routes involving chemical co-precipitation and solvothermal/ hydrothermal techniques aptly fit in the criteria of being less expensive and simple.

In current studies, chemical synthesis routes such as chemical reflux technique and low temperature solvothermal/hydrothermal techniques have been used to synthesize transition metals doped ZnS nanoparticles and nanorods.

### 2.3.1 Chemical reflux technique

Reflux technique is a chemical synthesis route generally used to synthesize small sized nanocrystals [140]. It is based on distillation which involves the condensation of chemical vapours formed due to the heating of chemical reactants. The vapours formed get condensed in condenser tube and return to the solution again.

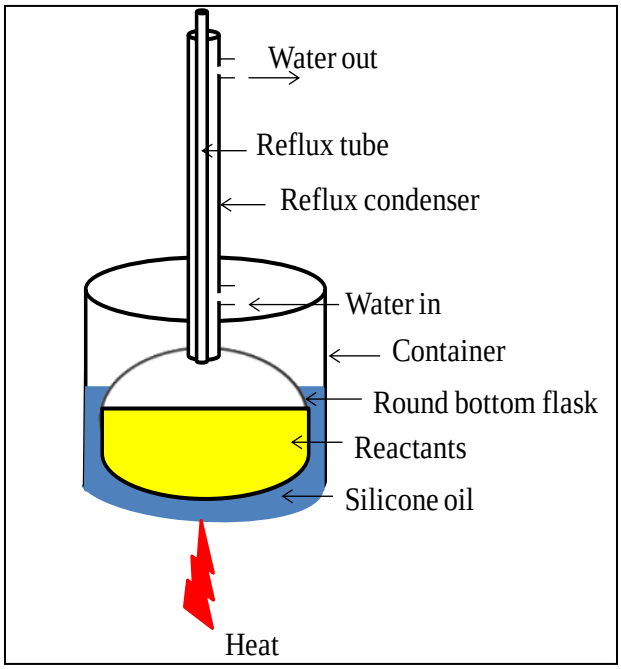


**Figure 2.1** Chemical reflux technique set up for synthesizing nanoparticles

A typical reflux technique involves a liquid reaction mixture placed in an open-ended flask fitted with a condenser having water inlet and outlet. The reaction mixture is heated while continuous stirring and condensate are allowed to collect again in the reaction mixture. In current study,

separately prepared solutions of zinc and sulpher precursors in desired concentration (0.5 M each) have been mixed in a round bottom flask with reflux condenser attached as shown in Figure 2.1. The mixture is stirred constantly at the temperature of 80 °C for 3 hour until the white precipitates appear. The precipitates are washed with water and acetone 4-5 times and the resultant mixture is dried at temperature of 80 °C for 6 hour. For transition metals doping, desired transition metal precursor, in suitable concentration (x = 0.01, 0.05 and 0.1), is added to the above mixture. The size of the nanocrystals depends upon the concentration of precursors, temperature, and duration of the reflux process.

### 2.3.2 Solvothermal and hydrothermal techniques

Solvothermal and hydrothermal techniques are used to synthesize wide variety of nanomaterials, including nanoparticles and nanorods, at elevated temperatures ranging between 100-1000 °C. In a solvothermal technique, different precursors in desired concentration are mixed with appropriate solvent, which may be an organic ligand compound depending on desired morphology of the nanostructures, in an air tight Teflon lined stainless steel cylinder as shown in Figure 2.2. The air tight cylinder is kept in an oven at desired temperature for some time ranging between 3-24 hour. The reaction mixture heated up to a stipulated time period is then allowed to cool at room temperature. The reaction mixture is then washed thoroughly and resultant sample is allowed to dry at an appropriate temperature in an oven. If the solvent used is water then the process is termed as hydrothermal, and if the solvent is other than water, it is termed as solvothermal. Temperature, solvent and time etc. are the crucial parameters for deciding the size and morphology of the nanostructures.

**Figure 2.2** Teflon lined stainless steel cylinder

### 2.3.2.1 Synthesis of transition metals-doped ZnS nanoparticles

Transition metals-doped ZnS nanoparticles have been synthesized using low temperature solvothermal technique [138]. In the current study, zinc acetate as source of Zn, thiourea as a source of sulpher, nickel chloride as source of dopant Ni, cobalt chloride as source of dopant Co, iron chloride as source of dopant Fe, in desired concentrations, have been used, whereas, ethanol has been used as a solvent. In this process zinc acetate and thiourea (1:3), in desired concentrations, are dissolved in the 70 ml ethanol. For transition metals doping, corresponding precursor, in desired concentration, is added to the above mixture. The solution mixture is then sealed in a Teflon lined stainless steel chamber of 100 ml capacity, and placed in an oven at a temperature of 180 $^{o}$C for 10 hour. The reaction has been shown in Figure 2.3. The resultant mixture was cooled at room temperature and washed with water and acetone for several times. The obtained samples were dried for 6h at 80 $^{o}$C. It is important to note here that when ethanol is used as solvent, ZnS nanoparticles obtained has been found having cubic structure, whereas, when EN and ethylene glycol (1:5) mixture is used as solvent, wurtzite structure is obtained.

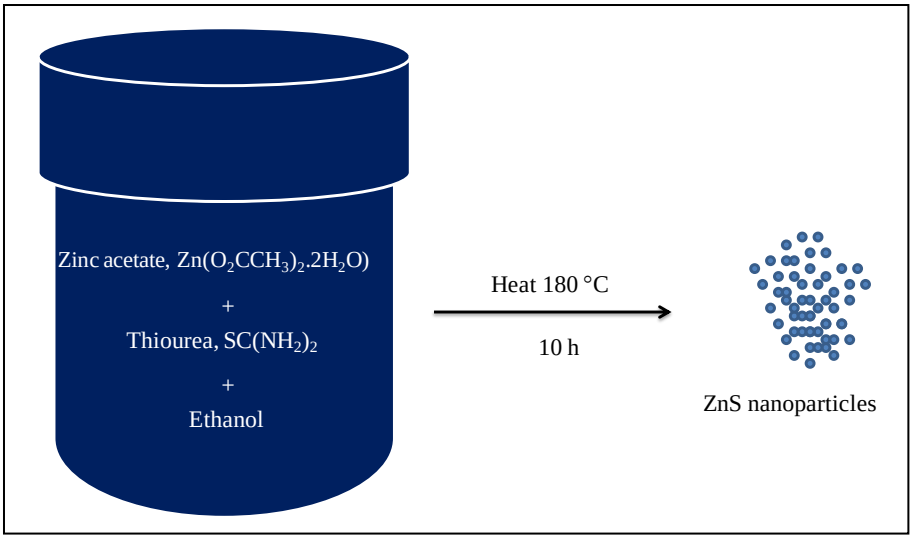


**Figure 2.3** Solvothermal reaction mechanism for synthesizing ZnS nanoparticles

Fe-doped ZnS nanoparticles have been synthesized by using EN and ethylene glycol (1:5) mixture as solvent and Co-doped ZnS nanoparticles have been synthesized this technique replacing ethanol as solvent.

### 2.3.2.2 Synthesis of transition metals-doped ZnS nanorods

Undoped and transition metals doped ZnS nanorods have been synthesized at low temperature by solvothermal technique, as described in the literature, with little modifications [138]. In this study, zinc acetate is used as source of Zn, thiourea as a source of sulpher, nickel chloride as source of dopant Ni, cobalt chloride as source of dopant Co, iron chloride as source of dopant Fe, whereas, mixture of EN and water (1:1) as solvent. Zinc and sulphur precursors taken are dissolved (1:3) in 70 ml en-water solvent. For transition metals doping, a desired dopant concentration, is added to the above mixture. This mixture is put inside a Teflon lined stainless steel chamber of 100 ml capacity as shown in Figure 2.4. This cylinder is then sealed and placed in a hot air oven at a temperature of 180 $^{o}$C for 10 hour. In this process homogenous nucleation occurs and the size of ZnS nanostructures is time and temperature dependent.

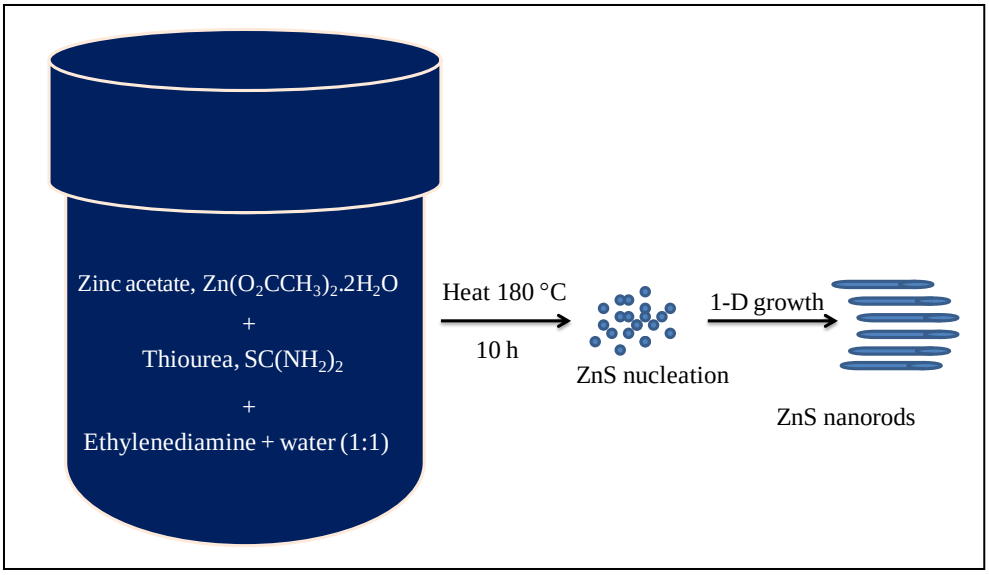


**Figure 2.4** Solvothermal reaction mechanism for synthesizing ZnS nanorods

The resultant solution was allowed to cool at room temperature and washed with water and acetone many times. The powder obtained was dried for 6 hour at temperature of 80 $^{o}$C.

### 2.4 Characterization techniques

Various techniques were used to characterize the undoped and transition metals doped ZnS nanostructures. The techniques used include X-ray diffraction (XRD), Transmission electron microscopy (TEM), Energy dispersive spectroscopy (EDS), UV-Visible (UV-Vis.) spectroscopy, Photoluminescence (PL) spectroscopy and Vibrating sample magnetometer (VSM). The particle size calculated using XRD was confirmed with the TEM results; the band gap obtained using UV-Vis. spectroscopy was confirmed using PL spectroscopy. Different techniques used in present work are discussed briefly as given below:

#### 2.4.1 XRD

XRD is an analytical technique, discovered by Max Von Laue. It is based on high energetic rays, X-rays, with wavelength of 0.01 to 0.1 nm. The X-rays suffer diffraction as they are allowed to fall on the crystalline materials, which produce the diffraction patterns as shown in Figure 2.5.

These patterns are analyzed to collect the information about the crystal structure of materials with the help of popular Bragg's law equation, introduced in 1913 by W.H. Bragg and W.L. Bragg. According to this law, when the X-rays are allowed to incident at the glancing angle $\theta$ on the surface of a crystalline material, the waves diffracted at the same angle $\theta$ are in phase according to the equation [156]:

$$2d\sin\theta = n\lambda$$

Where 'λ' is incident wavelength, 'θ' is glancing angle, 'd' is inter-atomic spacing, and 'n' an integer.

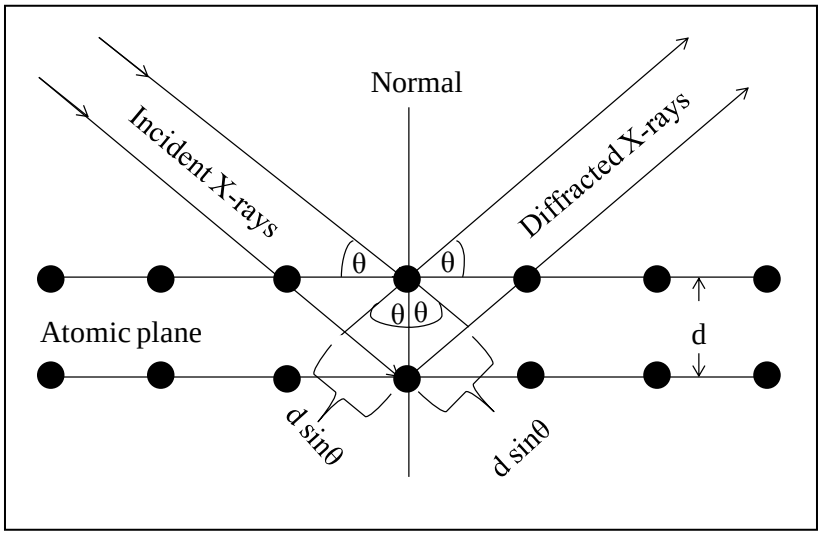


**Figure 2.5** Bragg's law of diffraction

### 2.4.1.1 XRD instrumentation and working

The instrument used to generate the X-ray diffraction pattern is known as X-ray diffractometer. It consists of an X-ray tube, X-ray detector and a sample holder. The X-rays are originated in the X-ray tube and these rays are accelerated towards the sample at incidence angle θ. The waves interact with the samples and the diffracted waves are detected by the detector in the range of 2θ as shown in Figure 2.6. CuKα radiations (λ = 1.5418 Å) are most commonly used X-rays source.

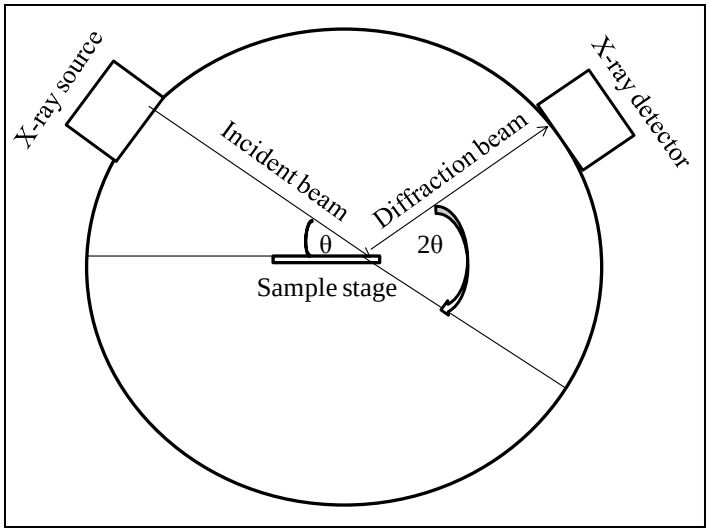


**Figure 2.6** Block diagram of X-ray diffractometer

XRD provides the exact peak positions in a sample which helps in determining the strains or defects induce in a crystal. At nanoscale, there is broadening in diffraction peaks, which is used to estimate the average crystallite size using the Scherrer formula as given below [157]:

$$D = \frac{K\lambda}{\beta\cos\theta}$$

where, 'D' is the mean crystallite size, 'K' is constant shape factor with value 0.94 in spherical nanoparticles, 'λ' is the wavelength of CuKα radiation (λ = 1.5418 Å), 'β' is full width at half maxima (FWHM), and 'θ' is Bragg's angle. A pictorial view of PANalytical X'Pert PRO X-ray diffractometer is shown in Figure 2.7.

**Figure 2.7** Pictorial view of PANalytical X'Pert PRO X-ray diffractometer [158]

### 2.4.1.2 Sample preparation for XRD

The sample under observation should be in the form of fine powder as well as the powder should be enough to comlpetely fill the sample holding plate.

### 2.4.1.3 Applications of XRD

XRD is one of the best non-destructive techniques used to get accurate information about a sample.

- It is used in phase analysis, crystallites size and orientation determination, qualitative phase identification.
- It is used in quantification of strains and defects induced in the crystals due to some impurities.

- XRD is used in determining the lattice parameters of a crystal structure.

*In the current thesis work, XRD analysis of the transition metals doped ZnS nanostructures have been carried out using PANalytical X'Pert PRO X-ray diffractometer with CuKα (λ = 1 .5418 Å) radiation operated at 45 kV and 40 mA.*

### 2.4.2 TEM

TEM is a high resolution electron microscopic technique generally used to give an idea of the morphology of the materials. It works like a slide projector. TEM makes use of an electron beam to generate the image of the specimen. It provides much higher magnifications and has a more resolving power as compared to an optical microscope. It allows the users to finer details of small objects. The main components of TEM include an electron gun, electromagnetic condenser lenses, specimen holder, objective lenses, projector lenses and fluorescent screen as shown in Figure 2.8. The materials used as electron gun are tungsten filament or lanthanum hexaboride ($LaBH_6$). Among these two, tungsten filament is the most commonly used as electron gun source to produce monochromatic electron beam. The emitted electrons from the heated tungsten filament are attracted towards anode and the beam is focused by the Wehnelt cap. The focused beam is accelerated towards the condenser lenses, which produce a coherent beam. The coherent beam is allowed to pass through very thin specimen. The transmitted electrons are focused by objective and projector lenses, which finally strike on a fluorescent screen, producing an image. Pictorial view of TEM instrument is shown in Figure 2.9.

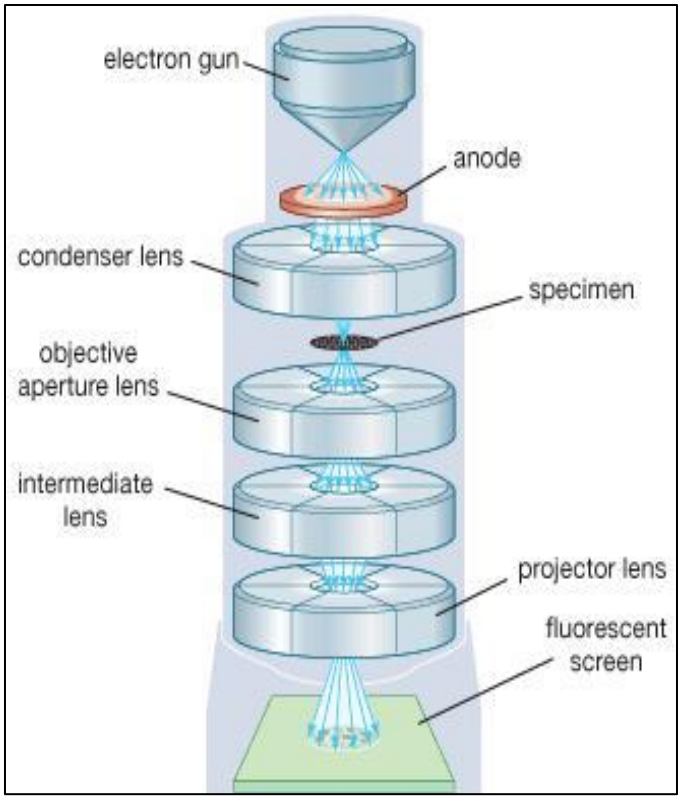


**Figure 2.8** Block diagram of TEM [159]


**Figure 2.9** Pictorial view of TEM instrument [160]

#### 2.4.2.1 TEM sample preparation

Sample preparation is a crucial part of TEM characterization. For having high resolution image the specimen must be thin. The TEM analysis of nano powdered samples is easy as compared to the bulk samples as such materials are needed to be polished appropriately to make them thin enough for characterization. In nano powdered samples, the samples are just dispersed in appropriate solvent and, resultant solution is allowed to spread on specially designed metal mesh grid. The grid is then placed in a sample holder to take the images of the samples. In the present study, carbon coated copper grids have been used to characterize the undoped and doped ZnS nanostructures.

#### 2.4.2.2 Applications of TEM

TEM can be used in different modes to obtain the information:

- TEM gives the information about the morphology and topography of the sample.
- In high resolution (HRTEM) mode, it provides molecular information about the sample.
- In selected area electron diffraction (SAED) mode, it gives the information about crystalline nature of the sample.
- TEM are used to identify the defects and flaws in the samples.

*In the present thesis work, TEM images of the synthesized samples have been recorded using transmission electron microscope (TEM; Hitachi (H-7500)). HRTEM images were recorded using TEM (FEI-Tecnai F30 $G^2$ STWIN) operated at 200 keV.*

### 2.4.3 EDS

EDS is also termed as energy dispersive X-ray spectroscopy (EDX) or energy dispersive X-ray analysis (EDXA). This technique is very useful in current study for the elemental analysis of the doped samples. It generally comes as an accessory with scanning electron microscope (SEM).

EDS analysis comprises the generation of X-ray spectrum from the scanned area of SEM. It uses characteristic X-ray beam to give the idea of different elements present in a sample. The characteristic X-ray beam is allowed to fall on the specimen under observation. This beam may knock off the inner shell electrons bound to the nucleus creating a hole in place of knocked off electron.

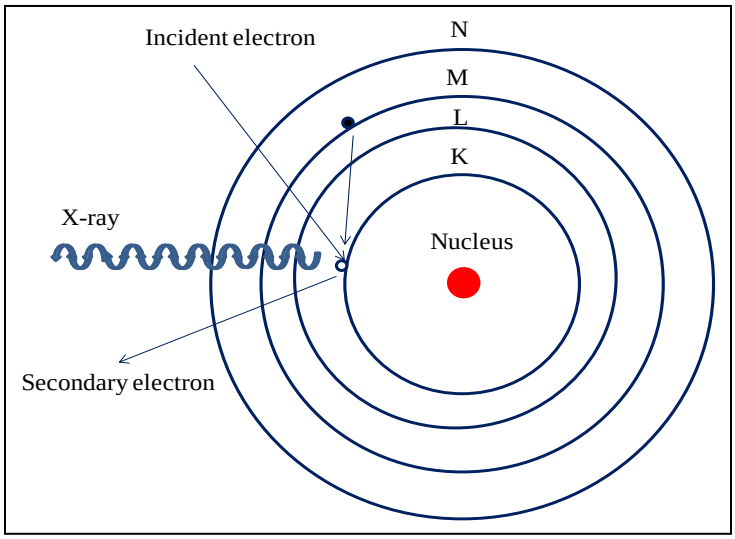


**Figure 2.10** Characteristic X-ray production mechanism

This hole is filled with electron from upper energy levels with a release of energetic beam in the form of X-ray beam. The energy of the released beam is characteristic of a particular atom, which can be measured and an exact idea about the element present in the samples, can be taken. The whole process has been depicted in Figure 2.10.

### 2.4.3.1 EDS instrumentation and working

EDS system is attached with either SEM or TEM instrument. It consists of an electron gun, X-ray detector and software to collect and analyze energy spectra. An electron gun produces high energy electron beam, which falls on the specimen surface and different types of interactions take place as shown in Figure 2.11.

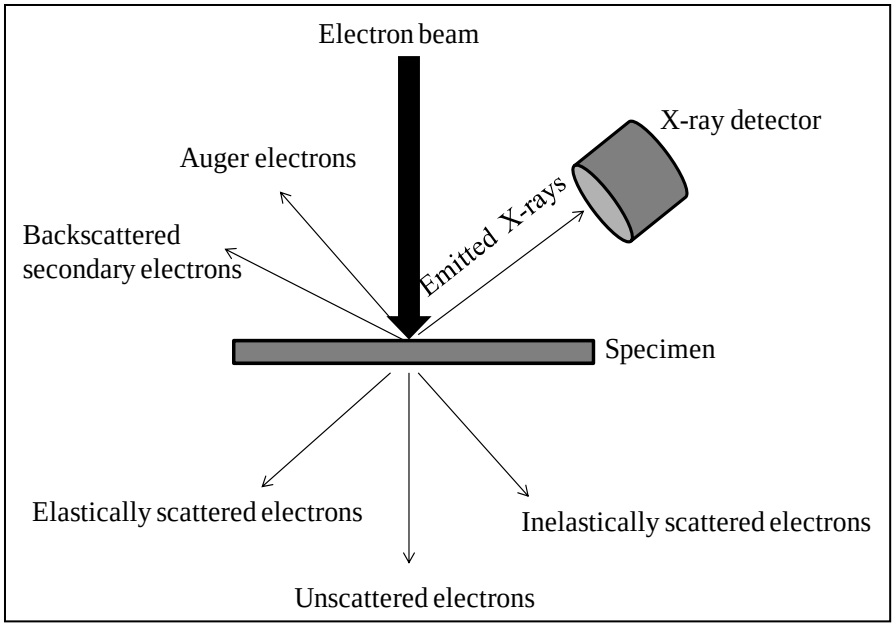


**Figure 2.11** EDS detection scheme

A specially designed X-ray detector absorbs the energy of the X-rays and converts these to useful electrical signals. These signals are fed to the software for further analysis which gives the energy diagram of different elements present in the sample. EDS provides the quantitative analysis of the sample under observation. The detector detects the weight percentage and atomic percentage of elements present in the sample.


**Figure 2.12** Pictorial view of SEM attached EDS system [161]

#### 2.4.3.2 Sample preparation for EDS

The sample preparation for EDS analysis is similar to that used in SEM characterization. Carbon or gold coating is generally required particularly for non-conducting samples and characterizations must be done under vacuum.

#### 2.4.3.3 Applications of EDS

The applications of EDS include:

- Qualitative and quantitative analysis of the samples
- Detection of the elements with atomic numbers, Z>3 to Z = 92; with minimum detection limit as low as 0.1% to a few weight percent, depending on specimen under observation.

*In the current thesis work, the presence of different elements has been confirmed using EDS system of OXFORD Analytical Instrument.*

### 2.4.4 UV-Vis. spectroscopy

UV-Vis. spectroscopy, an indispensable tool to characterize optical properties of samples, is based on Beer-Lambert's law. UV-Vis. region ranges between 200-800 nm of electromagnetic spectrum corresponding to the energy range of 6.2-1.5 eV. The energy given in this energy range is sufficient to excite the ground state electrons to the excited state, which gives idea about the maximum absorbance of a particular sample. It helps in determining the band gap and maximum absorbance wavelength ($\lambda_{max}$) of the samples. In UV-Vis. spectroscopy, the samples can be used in solution and solid forms.

#### 2.4.4.1 Beer-Lambert's law

According to Beer-Lambert's law, the absorbance, i.e., the amount of monochromatic light absorbed by the homogenous solution of a given sample is proportional to thickness, L, and concentration, c, of the sample: $A = \varepsilon cL$, where, ε is extinction coefficient and is called molar absorptivity.

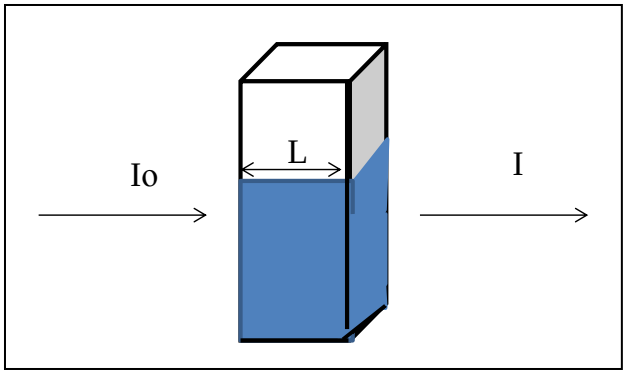


**Figure 2.13** Illustration of Beer-Lambert's law

Absorbance (A) depends upon the intensity of incident and transmitted light i.e. $A = \log\left(\frac{Io}{I}\right)$. Hence, $A = \log\left(\frac{Io}{I}\right) = \varepsilon cL$, where, $I_0$ and I are respectively the intensities of incident and transmitted light. A typical illustration of Beer-Lambert's law is shown in Figure 2.13.

**2.4.4.2 Working of UV-Vis. spectrophotometer**

The components of UV-Vis. spectrophotometer include a stable beam source, monochromator, sample holder, radiation detector or transducer and signal processing unit, as shown in Figure 2.14. A radiation source must provide good continuous intensity in UV and visible region. Generally, deuterium lamp is used as beam source for UV measurements (190-400 nm) and tungsten-halogen lamp is used for visible measurements (400-800 nm). The spectrophotometers consist of both types of beams sources to give the UV-Vis. spectra. To get a beam of desired wavelength from source beam, a monochromator is used, which may be a prism or grating type. The monochromatic beam is allowed to fall onto a quartz cuvette of length 1.0 cm containing a sample solution. The signal emitted from the solution is detected by a detector and converted into an electrical signal; this signal is processed and displayed on the display device.

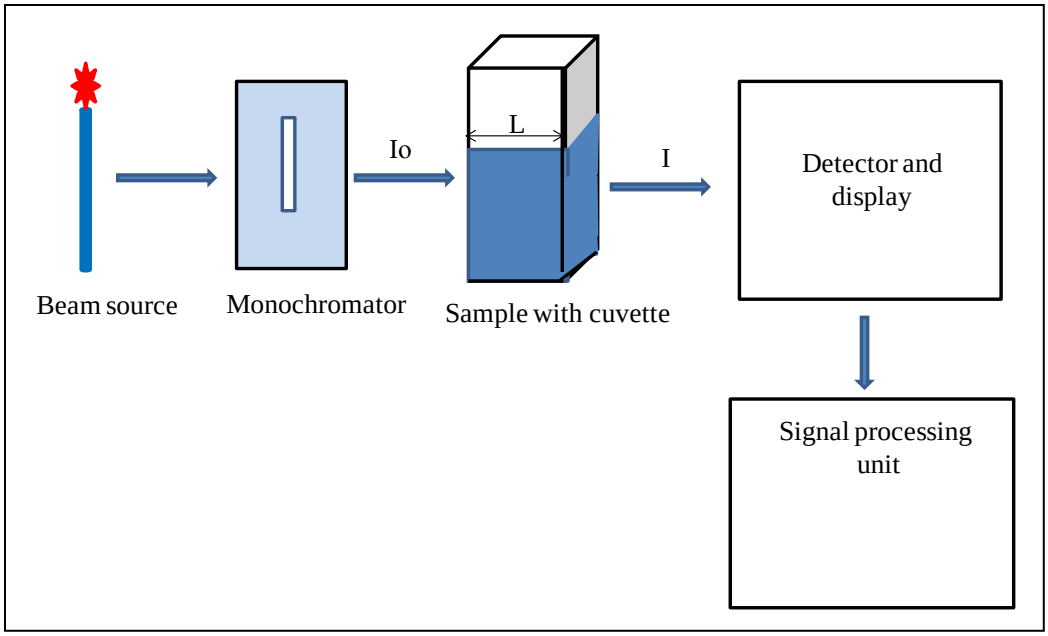


**Figure 2.14** UV-Vis. experimental setup

Pictorial view of UV-Vis. spectrophotometer system is shown in Figure 2.15.


**Figure 2.15** Pictorial view of UV-Vis. spectrophotometer system [162]

#### 2.4.4.3 Sample preparation for UV-Vis. analysis

For obtaining a good UV-Vis. Spectrum, it is desired that the samples must be dispersed thoroughly. Proper sample dispersion is important because if the samples are not dispersed properly in the solvent then the light can be scattered by the particles of the sample which may not provide suitable data. The dispersion can be improved by sonicating the samples for sometime in a solvent. In this study, ethanol has been used as solvent and the samples have been sonicated until they are dispersed properly.

#### 2.4.4.4 Applications of UV-Vis. spectroscopy

UV-Vis. spectroscopy has many applications including:

- Detection of the impurities in the samples,
- Determination of energy band gaps in semiconductors,
- Measurement of maximum absorbance wavelength of the samples,
- Analysis of molecular weight the samples,
- Qualitative and quantitative analysis of samples.

*In the present thesis work, the optical absorption spectra have been recorded with UV-visible spectrophotometer of Analytic Jena, SPECORD 205.*

### 2.4.5 PL spectroscopy

PL spectroscopy is another powerful non-destructive technique to study the optical properties of the materials. Experimental setup of PL spectrophotometer has been shown in Figure 2.16. In this technique, a laser light falls onto a sample which excites its electrons. The excited electrons return to their ground state with the emission of light. This emission of light is known as photoluminescence. In a typical PL spectroscopic technique, a laser light having energy greater

than the optical band gap of the given sample, is directed towards the filter, which throws the selected wavelength light towards the cuvette containing sample.

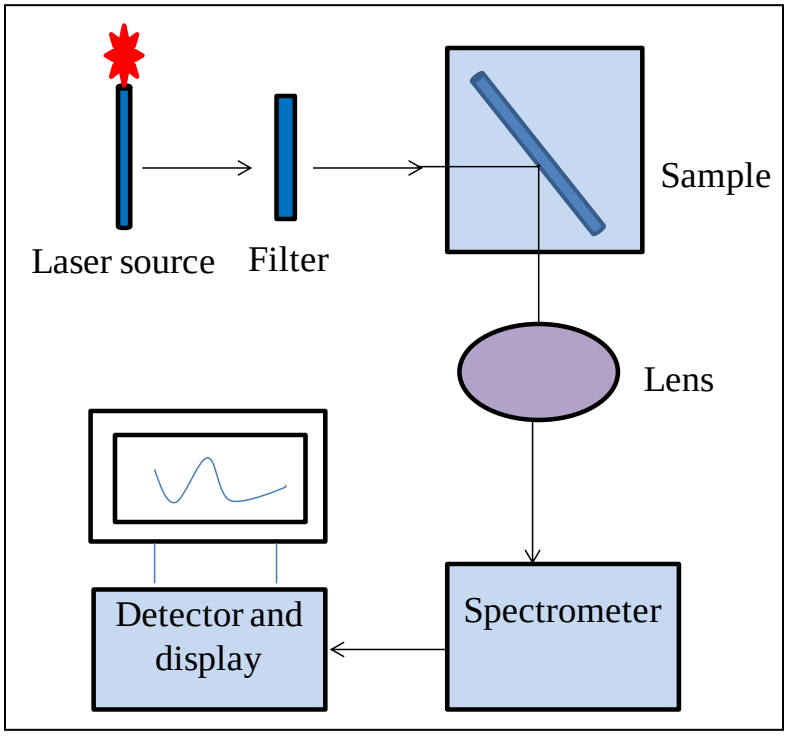


**Figure 2.16** Experimental setup of PL spectrophotometer

The orientation of sample is chosen in such a way that the reflected laser light and PL emission propagate in different directions. The emitted light propagates through fiber optic cable and spectrophotometer. The diffraction grating inside spectrophotometer diffracts different wavelengths in different directions. The detector measures signal intensity corresponding to each wavelength and the output device displays PL spectra of the sample under investigation. Pictorial view of Perkin Elmer LS55 spectrometer has been shown in Figure 2.17.

**Figure 2.17** Pictorial view of Perkin Elmer LS55 spectrometer [163]

### 2.4.5.1 Sample preparation for PL

Sample preparation for obtaining a PL spectrum is same as in UV-Vis. technique. The sample must be dispersed thoroughly in appropriate solvent in a sonicator. In this study, ethanol has been used as solvent and the samples have been sonicated until a clear solution is obtained.

### 2.4.5.2 Applications of PL spectroscopy

Various applications of PL spectroscopy include:

- Determination of the band gaps of semiconductors,
- Determination of the defects induced in the semiconductor lattice,
- Assessment of the quality of the semiconductors.

*In the current thesis work, the PL spectra of the undoped and doped ZnS samples were recorded using Perkin Elmer LS55 spectrometer.*

### 2.4.6 VSM

Vibrating sample magnetometry (VSM) technique is used to study the magnetic behaviour of the materials. This technique was invented in 1956 by Simon Foner at MIT and is based on Faraday's law [164]. In a typical VSM system a piezoelectric material is used to produce sinusoidal vibrations, which induce an electrical signal in pick-up coils generally translated by the transducer family into vertical vibrations. The electrical signal produced is directly

proportional to the sample magnetization. VSM has the capability of measuring extremely week signals of the order of ~$10^{-7}$ emu. The upper range for magnetic field measurement in VSM is 2 Tesla (T).

**2.4.6.1 VSM instrumentation and working**

In a VSM system, the sample is placed inside the sample holder, which is fixed between pair of pick-up coils of the electromagnet. The block diagram of a typical VSM system is shown in Figure 2.18.

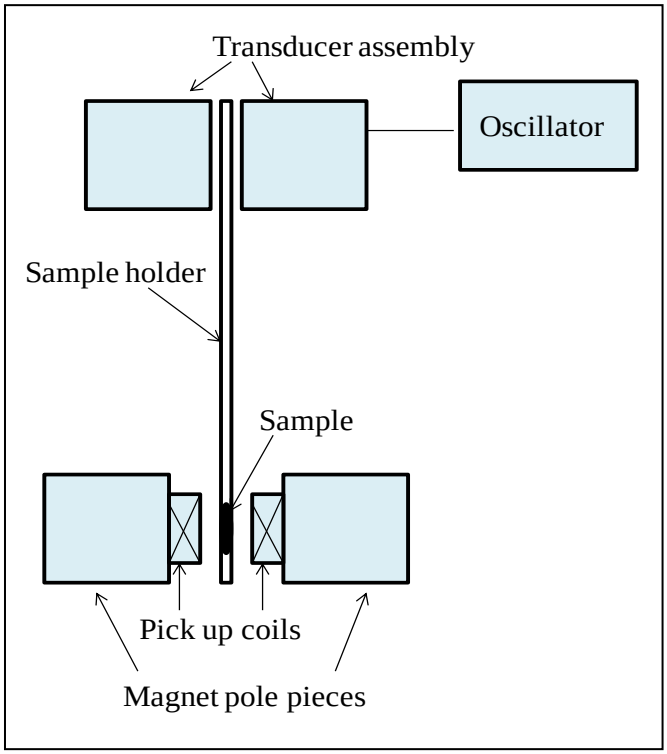


**Figure 2.18** Block diagram of VSM system

The application of magnetic field produced by the electromagnet induces magnetization in the sample. The sample is allowed to vibrate along the vertical axis, which induces a voltage in pickup coil which depends upon magnetic moment of sample. The pickup coils pick the induced signal which depends on the amplitude and frequency of sample vibration. The magnetic

moment (m) as a function of magnetic field (H) is displayed as output. Pictorial view of VSM magnetometer has been shown in Figure 2.19.

**Figure 2.19** Pictorial view of VSM magnetometer [165]

### 2.4.6.2 Applications of VSM

- Measurement of the magnetic properties of materials in powdered, thin films, and liquid form,
- Study of ferromagnetic, diamagnetic, paramagnetic, ferromagnetic, and antiferromagnetic curves of the materials,
- Study of GMR, TMS, and other magneto-optical materials analysis.

*In the present thesis work, the magnetic measurements (M-H) have been carried out using vibrating sample magnetometer (Lake Shore).*

# Chapter 3

# Results & Discussions

# Chapter 3

## Results & Discussions

*This chapter contains the detailed results and discussions of transition metals (Ni, Fe and Co) doped ZnS nanostructures. The various results obtained using the characterization techniques such as TEM, HRTEM, XRD, UV-visible, PL, and VSM have been analyzed with minute details. The chapter starts with the transition metal doped nanoparticles. Later part of the chapter consists of analysis of the corresponding nanorods. The detailed results and discussions have been presented as given below:*

### 3.1 Transition metals-doped ZnS nanoparticles

ZnS nanoparticles have been doped with transitions metals- Ni, Fe and Co, individually. Various studies of these nanoparticles are presented below:

#### 3.1.1 $Zn_{1-x}Ni_xS$ (x = 0.00, 0.01, 0.05 and 0.10) nanoparticles

This section comprises morphological, structural, optical and magnetic studies of $Zn_{1-x}Ni_xS$ (x = 0.00, 0.01, 0.05 and 0.10) nanoparticles synthesized using technique as discussed in chapter 2. The properties have been analyzed using TEM, EDS, XRD, UV-Vis., PL and VSM techniques.

##### 3.1.1.1 Morphological studies

The morphological analysis was carried out using TEM instrument. The TEM images of the ethanol dispersed $Zn_{1-x}Ni_xS$ (x = 0.00 and 0.10) nanoparticles are shown in Figure 3.1. The images indicate nearly spherical shaped nanocrystals with average size ~5 nm in case of x = 0.00 and 0.10 (Figure 3.1a and 3.1b) ZnS nanocrystals.

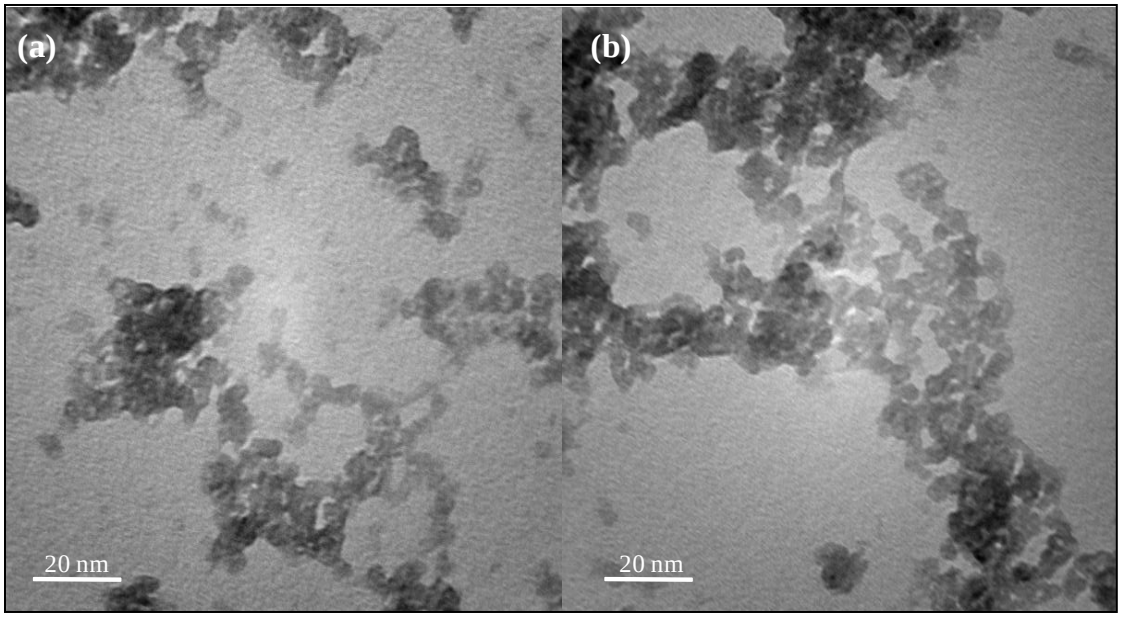


**Figure 3.1** TEM images of $Zn_{1-x}Ni_xS$ nanocrystals (a) x = 0.00 and (b) x = 0.10

The aggregation in the nanocrystals may be attributed to very small size of ZnS nanocrystals. It is clear that there is no significant change in the morphology of the Ni-doped nanocrystals as compared to the undoped counterparts [166].

### 3.1.1.2 Elemental studies

The elemental analysis of $Zn_{1-x}Ni_xS$ nanocrystals has been carried out using EDS. The elements present in $Zn_{1-x}Ni_xS$ nanoparticles have been shown in Figure 3.2. The spectra obtained exhibit the presence of Zn, S in undoped samples, whereas, doped samples indicate Zn, S and Ni atoms present in the samples. The two or more peaks corresponding to an atom indicate different shells electron emission. From the spectra obtained it is clear that Ni is present in the doped samples. The observed atomic percentages of Ni are 0.82%, 3.72% and 7.06% respectively corresponding to x = 0.00, 0.01, 0.05, and 0.10 concentrations, which indicate that the observed amount of Ni is less as compared to the actual doped Ni. The same may be attributed to the removal of non-reacted Ni atoms during washing process.

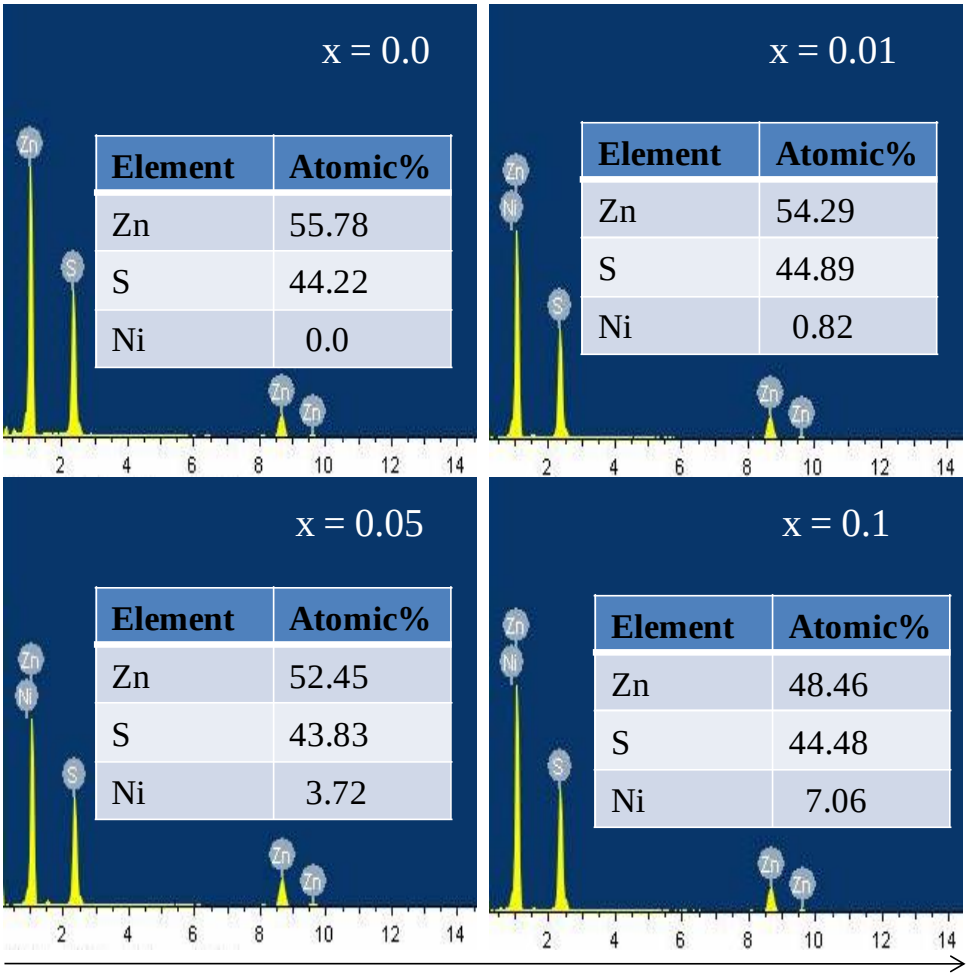


**Figure 3.2** EDS spectra of $Zn_{1-x}Ni_xS$ (x = 0.00, 0.01, 0.05, and 0.10) nanocrystals

### 3.1.1.3 Structural studies

The XRD patterns of $Zn_{1-x}Ni_xS$ (x = 0.00, 0.01, 0.05, and 0.10) nanocrystals have been shown in Figure 3.3. The spectra obtained indicate cubic zinc blende structure of synthesized ZnS nanocrystals (JCPDS No. 05-0566). The diffraction peaks are observed at 2θ = 28.8°, 47.6°, and 56.45° corresponding to, respectively, the lattice planes (111), (220), and (311). As clear from XRD patterns, no separate peaks of Ni impurity phase have been observed in the Ni-doped ZnS nanoparticles, which indicate that Ni has been inserted in the ZnS matrix.

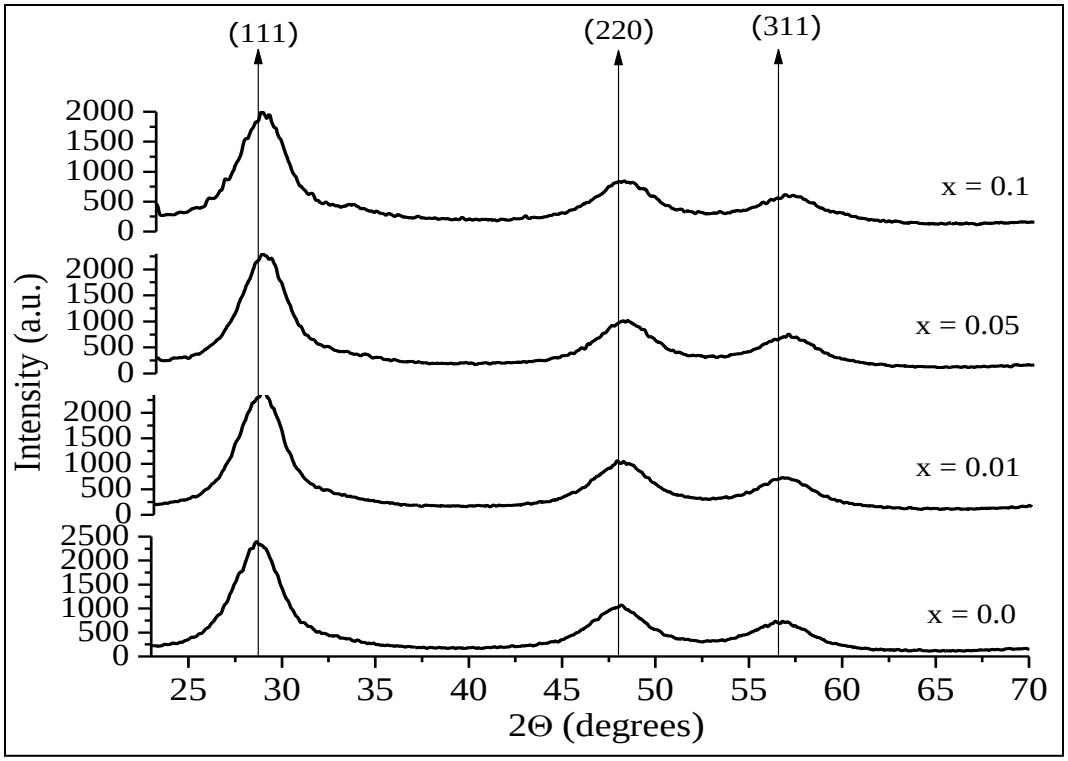


**Figure 3.3** XRD patterns of $Zn_{1-x}Ni_xS$ (x = 0.00, 0.01, 0.05, and 0.10) nanocrystals

A slight shift in the peak positions for Ni-doped ZnS nanoparticles *w.r.t.* the undoped counterpart also confirms the doping in ZnS matrix. It can be seen that the intensity of the XRD peaks decrease with increase in doping concentration, which may be associated with the strains and defects induced in ZnS lattice. The broadening of peaks indicates the nanometer regime of the ZnS nanocrystals. The average crystallite size was estimated by using Scherrer formula [155]. The diameter of the nanocrystals was found to be ~5 nm which is in close agreement with the TEM observations. The lattice parameter of ZnS nanocrystals has been calculated using the relation:

$$\frac{1}{{d_{hkl}}^2} = \frac{h^2 + k^2 + l^2}{a^2}$$

where, 'a' is lattice parameter, '$d_{hkl}^2$' is square of inter-planar spacing corresponding to the plane (hkl). The value of '$d_{hkl}$' has been obtained from X'Pert High Score software and for x = 0.00

concentration it is 3.13 Å, whereas for x = 0.10 concentration it is 3.08 Å. The calculated value of lattice parameter, a = 5.40 Å, for undoped (x = 0.00) ZnS nanoparticles, is more than those for Ni-doped (x = 0.01, 0.05 and 0.10) ZnS nanoparticles. In case of x = 0.10 concentration, this value is 5.31 Å. The Scherrer equation assumes that peak broadening is due to nanometer size of the crystallite, however, the peak broadening can be caused due to the instrumental broadening and due to strain broadening. Hence the average crystallite size and the strain induced in the lattice due to the doping have been estimated using the Williamson-Hall (W-H) plots using the equation [167]:

$$\beta Cos\theta = \frac{K\lambda}{D} + 4\varepsilon Sin\theta$$

where, 'D' is mean size of crystallite, 'K' is constant shape factor with value 0.94 in spherical nanoparticles, 'λ' is the wavelength of CuKα radiation (λ = 1.5418 ), 'β' is FWHM, 'θ' is Bragg's angle and 'ε' is strain induced. The size and strain induced in the lattice has been calculted by plotting βCosθ along y-axis and Sinθ along x-axis. The W-H equation when compared with general equation of line, y = mx + c, where 'm' is the slope and 'c' is the intercept, indicates that factor Kλ/D is the intercept and 4ε is the slope of the line. Hence from the intercept, one can obtain the value of average crystallite size, wherease from the slope of line, the strain induced can be calculated. W-H plots for different Ni concentrations (x = 0.00, 0.01, 0.05 and 0.10) have been plotted as shown in Figure 3.4. The βCosθ versus Sinθ plots exhibit a negative slope indicating that lattice is under compressive strain due to the different ionic radii of Zn ions and Ni ions. Various lattice parameters, size and strain induced at different Ni-doping concentrations are shown in Table 3.1.

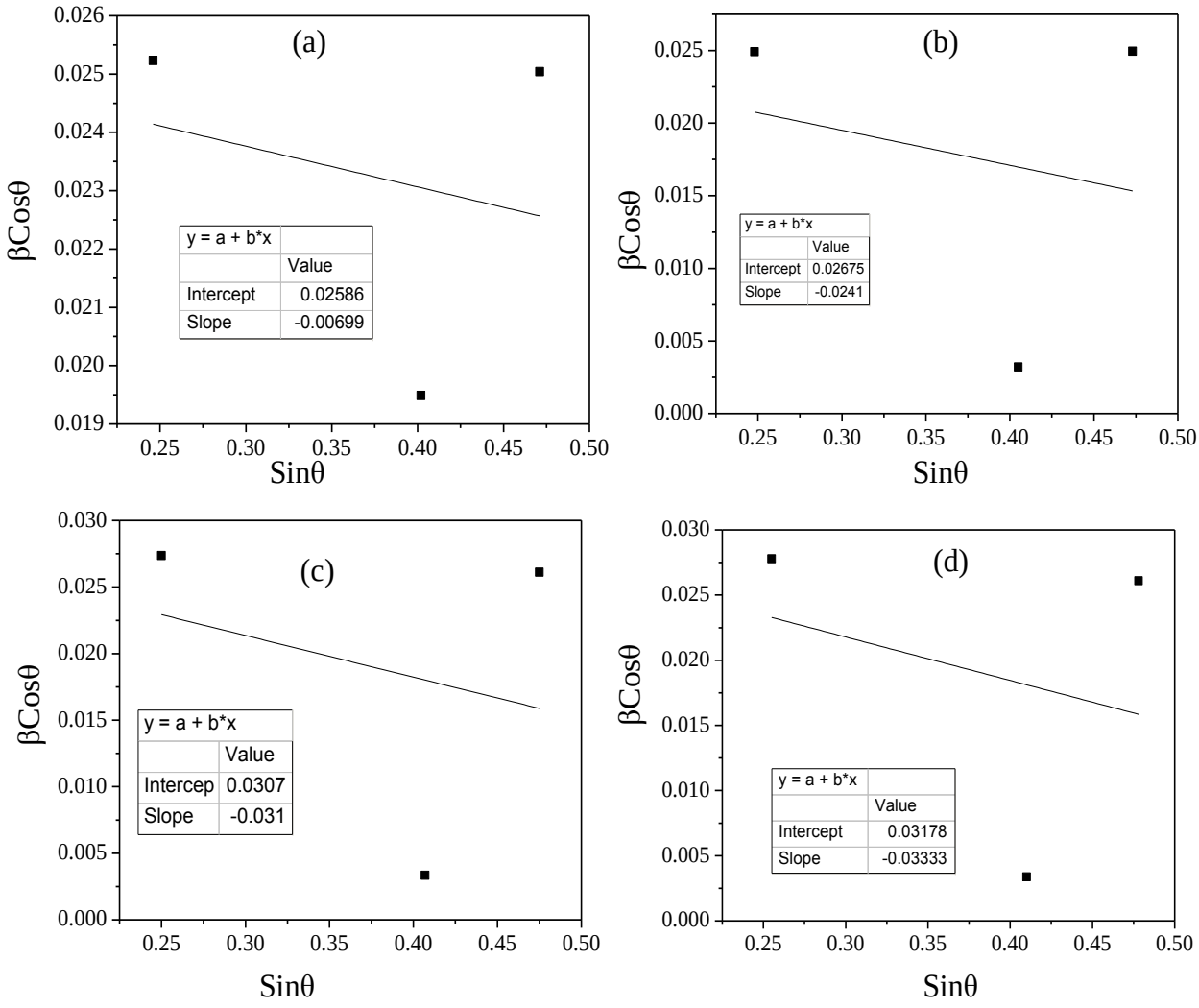


**Figure 3.4** W-H plots of $Zn_{1-x}Ni_xS$ nanocrystal at (a) x = 0.0, (b) x = 0.01, (c) x = 0.05, and (d) x = 0.1

**Table 3.1** Structural parameters of $Zn_{1-x}Ni_xS$ (x = 0.0, 0.01, 0.05, and 0.1) nanocrystals

| Ni doping (x) | 2θ | | | Lattice constant (Å) | d-spacing (Å) | Crystallite size (nm) | | Strain (ε) |
|---|---|---|---|---|---|---|---|---|
| | (111) | (220) | (311) | | | Debye Scherrer's equation | W-H plot | |
| 0.00 | 28.44 | 47.35 | 56.19 | 5.40 | 3.13 | 5.71 | 5.36 | -0.002 |
| 0.01 | 28.47 | 47.40 | 56.26 | 5.37 | 3.11 | 5.60 | 5.18 | -0.004 |
| 0.05 | 28.51 | 47.43 | 56.43 | 5.32 | 3.10 | 4.98 | 4.51 | -0.007 |
| 0.10 | 28.58 | 47.55 | 56.52 | 5.25 | 3.08 | 4.59 | 4.38 | -0.008 |

The reduction in lattice parameters in case of Ni-doped ZnS nanoparticles may be ascribed to compressive strain induced due to the replacement of bigger Zn ions with smaller Ni ions. From table it is clear that strain increases as the doping concentration is increased. In cases the crystallite size calculated using W-H plots is smaller than that of Scherrer's formula.

### 3.1.1.4 Optical studies

The optical studies have been analyzed on the basis of the spectra obtained via UV-Vis. and PL spectroscopy. The results obtained are discussed below:

#### 3.1.1.4.1 UV-Vis. studies

UV-Vis. spectra obtained for $Zn_{1-x}Ni_xS$ nanocrystals have been shown in Figure 3.5.

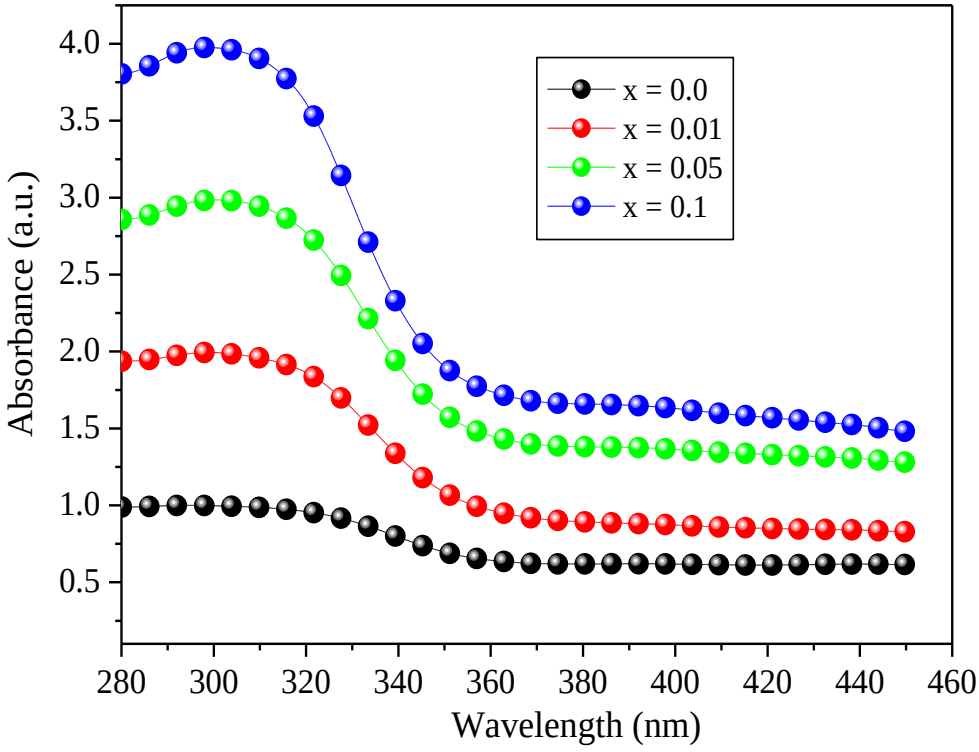


**Figure 3.5** UV-Vis. spectra of $Zn_{1-x}Ni_xS$ (x = 0.00, 0.01, 0.05, and 0.10) nanocrystals

The spectra exhibiting the absorption edge appearing at 317 nm for undoped ZnS nanocrystals corresponding to a band gap of 3.90 eV - blue-shifted when compared with bulk ZnS (3.6 eV) -

may be associated to quantum confinement effects [166]. The blue shift is more prominent as the doping concentration is increased. For x = 0.10, the absorption edge appears at 305 nm corresponding to the band gap of 4.06 eV. The blue-shift in Ni-doped ZnS nanoparticles may be attributed to the small radii of $Ni^{2+}$ ions as compared to $Zn^{2+}$, indicating that the $Zn^{2+}$ ions have been replaced with $Ni^{2+}$ ions in the doped ZnS nanocrystals. The increase in band gap of $Zn_{1-x}Ni_xS$ nanocrystals may be attributed to quantum confinement of ZnS nanocrystals. The blue-shift may also be associated with the strain induced in ZnS lattice due to doping.

#### 3.1.1.4.2 PL studies

The room temperature PL emission spectra obtained at excitation wavelength of 300 nm ($\lambda_{ex.}$ = 300 nm) are shown in Figure 3.6. The spectra obtained indicate two broad peaks centered at 360 nm and 435 nm. The peak centered at 360 nm may be attributed to wide band edge emission; whereas, the blue emission peak at 435 nm, may be attributed to radiative recombination between sulphur vacancies related donor energy levels and purity of phase of host ZnS material [166]. The PL intensity increases with x = 0.01 Ni doping, but, as the Ni-doping concentration is increased to x = 0.05 and 0.10, the intensity has been found to decrease. The increase in PL intensity at lower doping concentration may be attributed to a vacancy at interstitial sites or at the lattice position due to the doping. It may create new radiation centers, resulting in an increase in the PL intensity [168, 169]. As the concentration is increased to x = 0.05 and 0.10, the doped Ni ions interfere with the radiative recombination process.

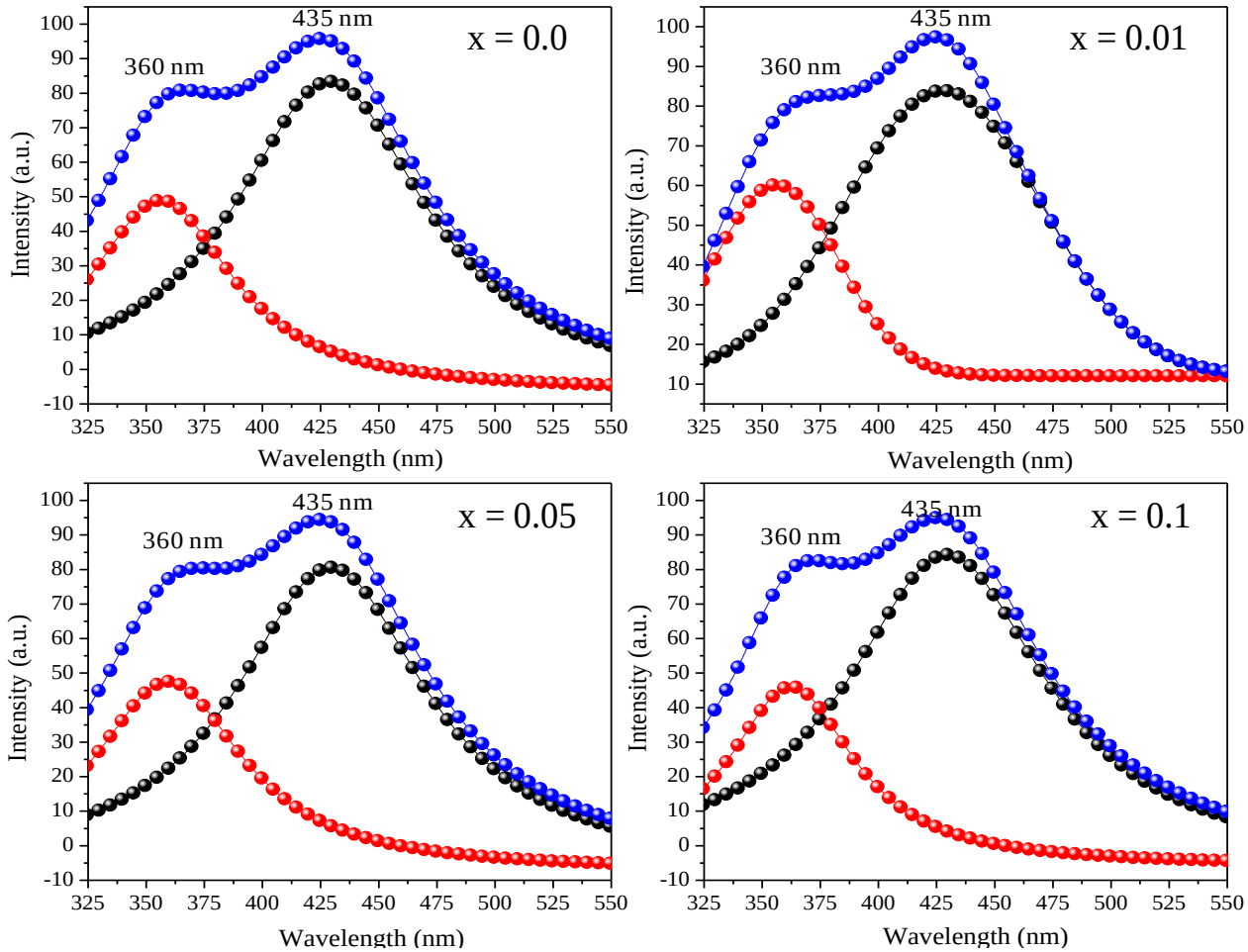


**Figure 3.6** PL spectra of $Zn_{1-x}Ni_xS$ (x = 0.00, 0.01, 0.05, and 0.10) nanoparticles

This effect overshadows the effect of creating new radiation centers, resulting in the quenching of fluorescence intensity at higher doping concentrations. Similar observations have been reported in literature with Ni-doping in ZnS nanoparticles [170].

### 3.1.1.5 Magnetic studies

Magnetic studies of $Zn_{1-x}Ni_xS$ nanocrystals have been analyzed on the basis of M-H curves up to 1.5 Tesla (T), obtained using VSM at room temperature, as shown in Figure 3.7 (a, b). M-H curves have been analyzed to study the magnetism induced in ZnS nanoparticles due to Ni-doping.

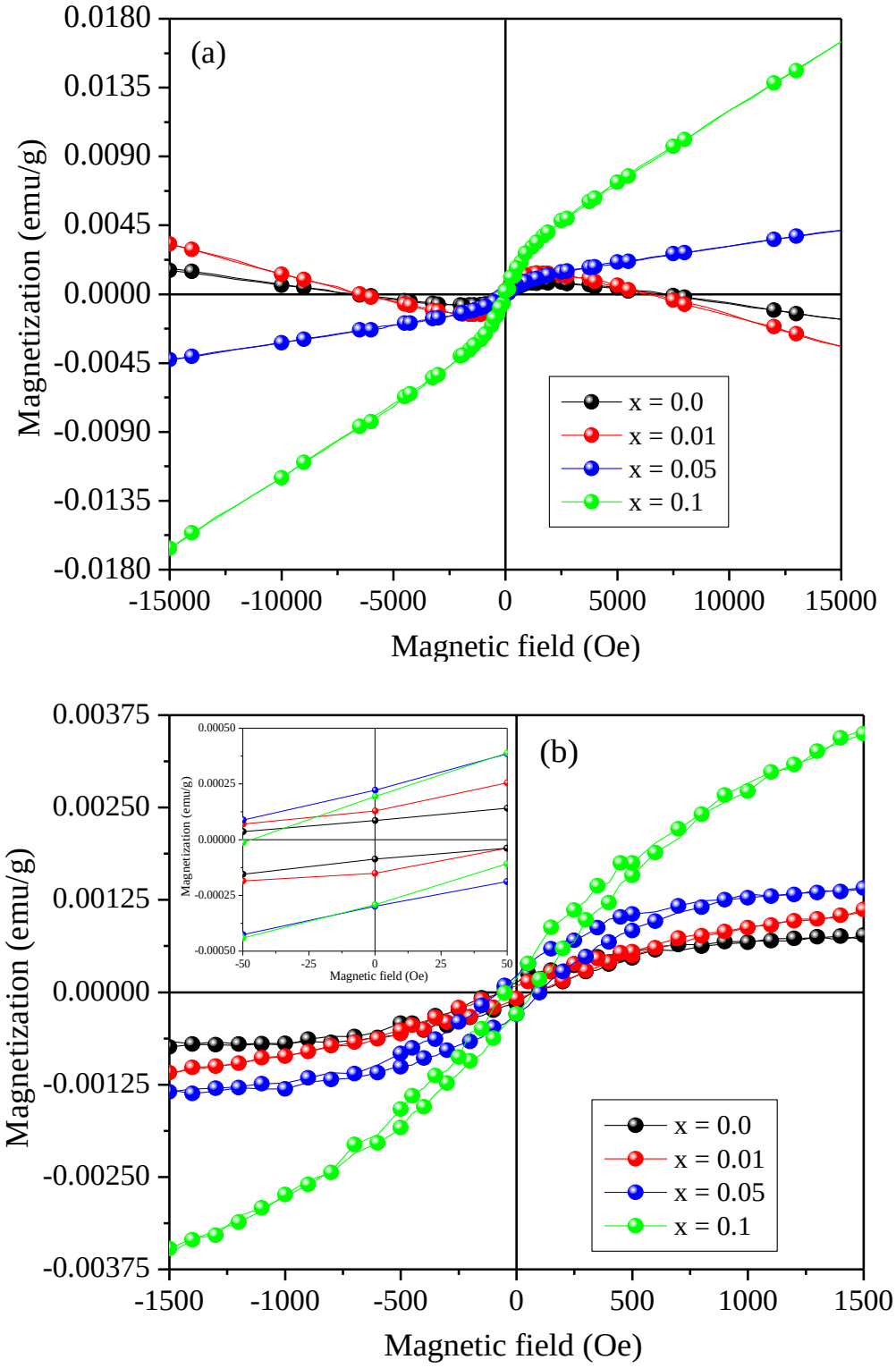


**Figure 3.7** M-H curves of $Zn_{1-x}Ni_xS$ (x = 0.00, 0.01, 0.05, and 0.10) nanoparticles (a) at 15000 Oe (b) at 1500 Oe [inset: magnified M-H curve at 50 Oe]

It is clear that at x = 0.00 and 0.01, Ni concentration the ZnS nanocrystals exhibit a weak ferromagnetic magnetic behaviour; whereas, at x = 0.05 and 0.10 Ni concentrations the ZnS nanoparticles indicate highly ferromagnetic behaviour. The increased ferromagnetic behaviour with increased Ni-concentration confirms that ferromagnetism induced is caused due to presence of Ni in ZnS matrix [166]. The values of remanent magnetizations for x = 0.00, 0.01, 0.05 and 0.10 Ni-doping are 0.0001 emu/g, 0.00125 emu/g, 0.0002 emu/g and 0.00015 emu/g respectively; whereas, the coercivity values are 70 Oe, 100 Oe, 200 Oe and 50 Oe respectively. Sambasivam et al. [74] and Eryong et al. [79] have also observed the weak ferromagnetism, termed as superparamagnetism, in Fe-doped ZnS nanoparticles caused due to small size of nanoparticles. Similar superparamagnetic behaviour has also been observed in literature in Co-doped ZnO nanoparticles due to small particle size [171, 172]. The magnetization increases as the Ni concentration is increased in ZnS lattice. As indicated in PL studies that the defects increase with increased doping concentrations, hence the magnetic behaviour may also be influenced by the increased Ni ions concentration. As in XRD spectra no extra phases of Ni, NiS or other impurities have been observed; hence, the magnetism induced is solely due to the Ni-doping. It has been observed that the saturation is exhibited at lower Ni ions concentrations; whereas, no saturation was observed at x = 0.10 Ni concentration. It has been reported in literature that at higher Ni-doping concentration, the distance between Ni-Ni ions is decreased, which leads to the non-saturation in the M-H curve [88].

### 3.1.2 Fe-doped ZnS nanoparticles

This section comprises the morphological, structural, optical and magnetic studies of Fe-doped ZnS nanoparticles. The $Zn_{1-x}Fe_xS$ (x = 0.00, 0.01, 0.05 and 0.10) nanoparticles have been

synthesized using technique as discussed in chapter 2. The properties have been analyzed using TEM, HRTEM, EDS, XRD, UV-Vis., PL and VSM techniques.

### 3.1.2.1 Morphological studies

Morphological analyses have been made using TEM and HRTEM images. The TEM and HRTEM images of $Zn_{1-x}Fe_xS$ (x = 0.00 and 0.10) nanoparticles are shown in Figure 3.8. It is clear that the Fe-doped ZnS nanoparticles are morphologically identical to the undoped counterparts.

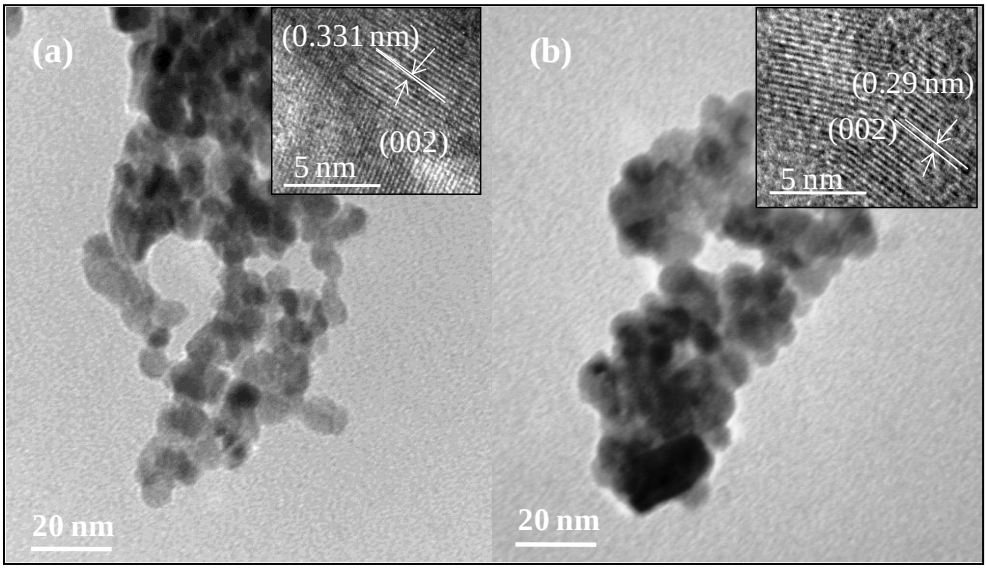


**Figure 3.8** TEM images of $Zn_{1-x}Fe_xS$ nanoparticles (a) x = 0.00 and (b) x = 0.10 (Inset: HRTEM images)

The TEM images indicate the average particle size as ~12 nm in case $Zn_{1-x}Fe_xS$ nanoparticles with almost spherical symmetry. The HRTEM images (Figure 3.7 inset) indicate the atomic spacing as 0.33 nm for undoped ZnS nanoparticles and 0.29 nm for doped counterpart. The slightly low atomic spacing in case of Fe-doped ZnS nanoparticles, due to the strain induced in ZnS lattice supports the insertion of Fe in ZnS lattice. These values accord well with d-spacing values of *(110)* plane in XRD spectra of standard ZnS [173].

### 3.1.2.2 Elemental studies

The doping percentage of doped Fe in ZnS nanoparticles has been confirmed by EDS analysis. The EDS spectra of $Zn_{1-x}Fe_xS$ (x = 0.00, 0.01, 0.05 and 0.10) nanoparticles are shown in Figure 3.9. The spectra obtained indicate the presence of Fe in ZnS matrix.

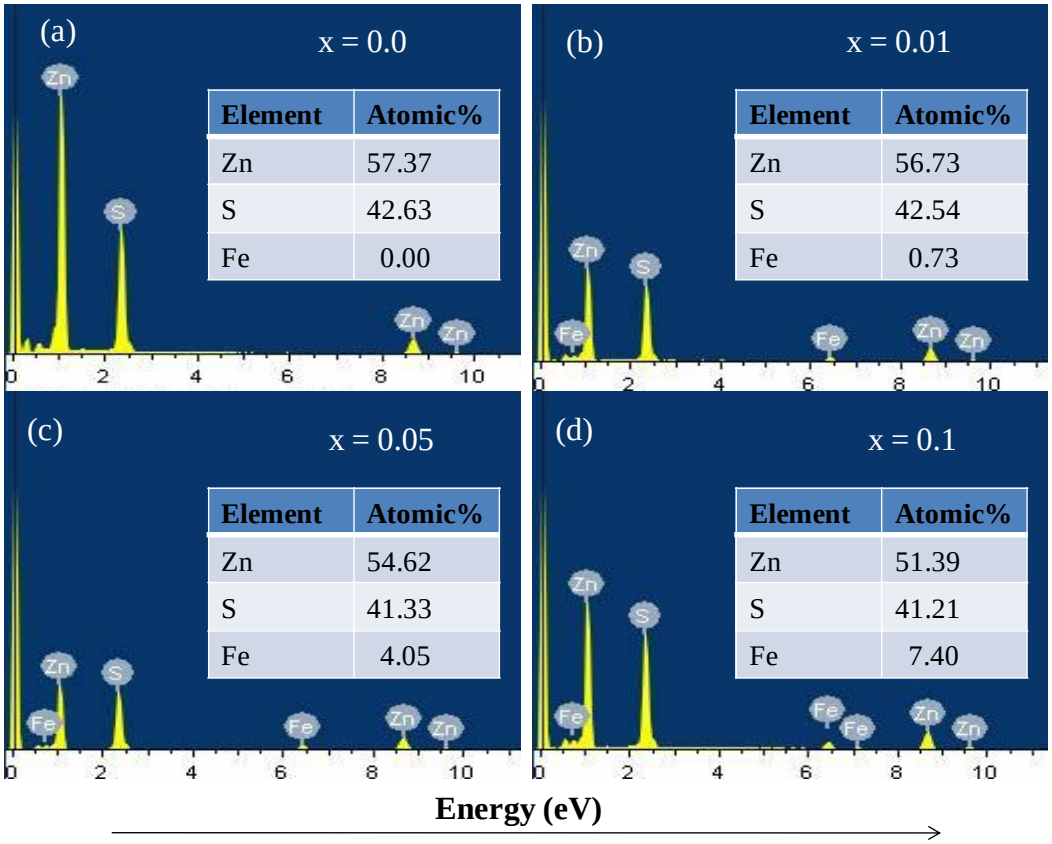


**Figure 3.9** EDS spectra of $Zn_{1-x}Fe_xS$ (a) x = 0.00 (b) x = 0.01 (c) x = 0.05 and x = 0.10 nanoparticles

Multiple peaks in EDS spectra for a particular element may be caused due to X-rays emission from different shells. The observed amount of Fe at x = 0.01, 0.05 and 0.1, doping concentrations is 0.73%, 4.05% and 7.40% respectively, indicating that the observed amount is less as compared to the actual doped amount. It may be attributed to extensive washing of samples leading to a decrease in observed percentage of doped Fe [173].

### 3.1.2.3 Structural studies

Structural properties and phase of $Zn_{1-x}Fe_xS$ (x = 0.00, 0.01, 0.05 and 0.10) nanoparticles have been determined using XRD technique. The XRD patterns have been shown in Figure 3.10. The XRD patterns exhibit broadening in the XRD peaks, indicating the nanometer regime of $Zn_{1-x}Fe_xS$ nanoparticles.

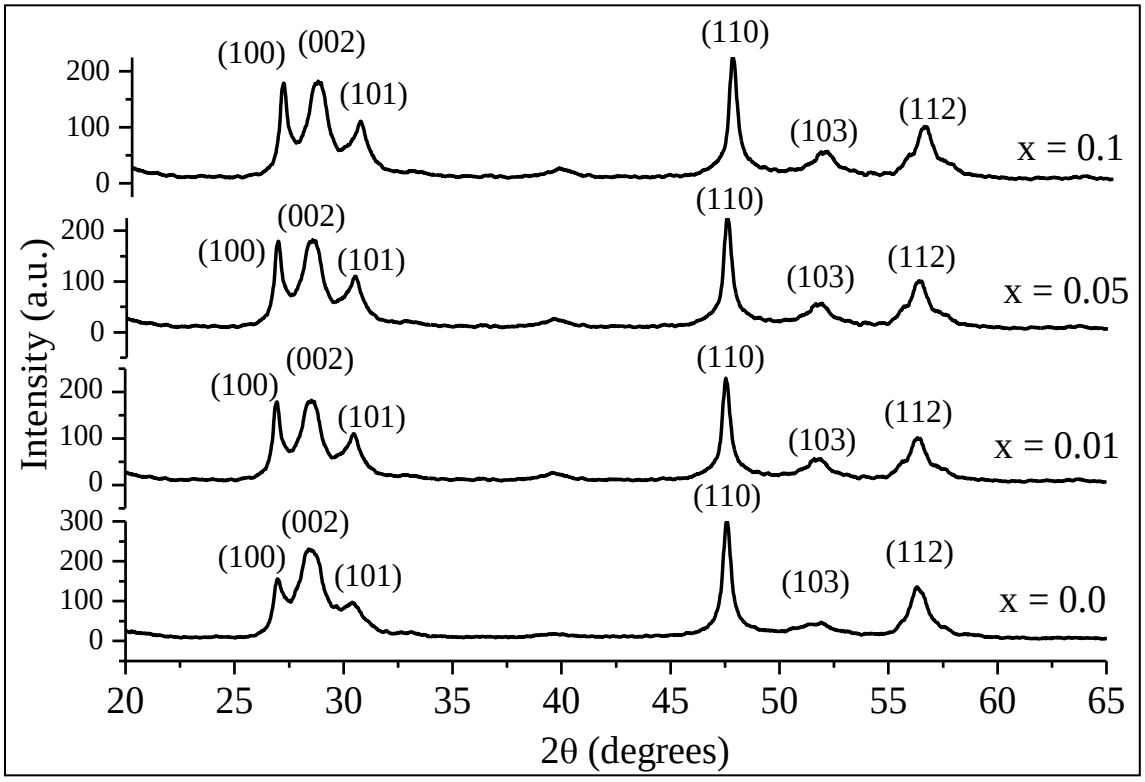


**Figure 3.10** XRD patterns of $Zn_{1-x}Fe_xS$ (x = 0.00, 0.01, 0.05 and 0.10) nanoparticles

The peaks are obtained at 27.011, 28.766, 30.521, 47.681, 51.971 and 56.651 corresponding to the (100), (002), (101), (110), (103) and (112) planes, which correspond to hexagonal crystal structure (JCPDS card No. 79-2204). No extra peak of impurity phase has been observed, indicating the single phase of all samples, which supports the substitution of Fe ions in ZnS lattice. The particle size of undoped (x = 0.00) ZnS nanoparticles as estimated from Scherrer's formula [157] is ~15 nm which accords well with TEM size. The particle size is found slightly reduced as the doping concentration is increased; it may be attributed to smaller ionic radii of Fe

ions as compared to ZnS ions. The intensity of the XRD peaks diminishes as the doping concentration is increased, which indicates the deterioration of structural quality of ZnS with Fe doping.

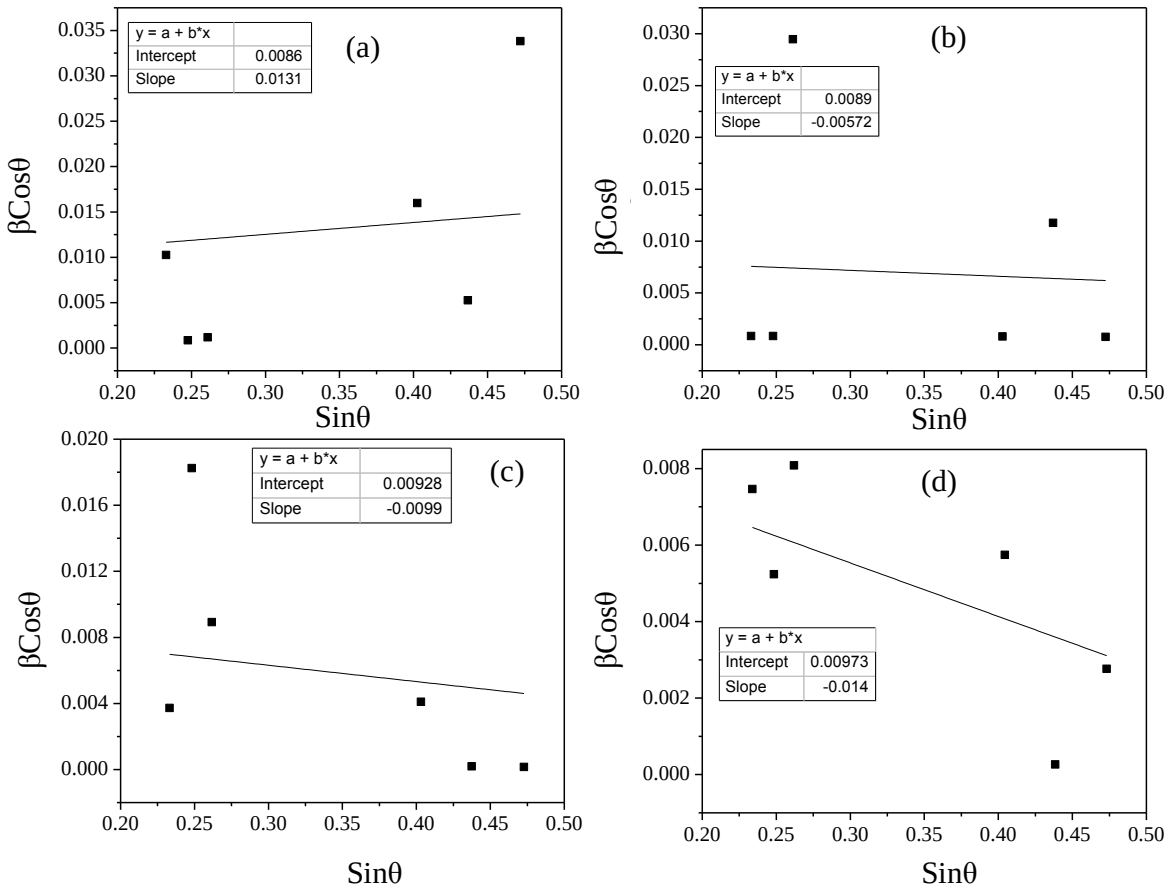


**Figure 3.11** W-H plots of $Zn_{1-x}Fe_xS$ nanoparticles at (a) x = 0.00, (b) x = 0.01, (c) x = 0.05, and (d) x = 0.10

**Table 3.2** Structural parameters of $Zn_{1-x}Fe_xS$ nanoparticles (*indicated few 2θ positions)

| Fe doping (x) | 2θ* | | | Lattice constant (Å) | d-spacing (Å) | Crystallite size (nm) | | Strain (ε) |
|---|---|---|---|---|---|---|---|---|
| | (002) | (110) | (112) | | | Scherrer's equation | W-H plot | |
| 0.00 | 28.34 | 47.21 | 56.14 | a = 3.84, c = 6.25 | 3.18 | 15.20 | 15.62 | 0.00327 |
| 0.01 | 28.38 | 47.27 | 56.19 | a = 3.81, c = 6.23 | 3.14 | 15.34 | 14.67 | -0.00142 |
| 0.05 | 28.47 | 47.33 | 56.31 | a = 3.77, c = 6.19 | 3.11 | 14.60 | 13.94 | -0.00247 |
| 0.10 | 28.50 | 47.46 | 56.42 | a = 3.75, c = 6.14 | 3.09 | 14.37 | 13.35 | -0.00350 |

The crystallite size and strain induced in the lattice have been calculated using W-H plots. W-H plots for different Fe concentrations (x = 0.00, 0.01, 0.05 and 0.10) have been plotted as shown in Figure 3.11. The βCosθ versus Sinθ plots again exhibit a negative slope indicating that lattice is under compressive strain. Different lattice parameters and strain induced at different Fe-doping concentrations are shown in Table 3.2. Clearly, as the Fe concentration is increased, the lattice parameters have been found slightly decreased, which indicates that the Fe-doped ZnS lattice is under compressive strain due to smaller radii of $Fe^{2+}$ ions as compared to $Zn^{2+}$ [173].

### 3.1.2.4 Optical properties

Optical studies are based on the UV-Vis and PL studies as presented below:

#### 3.1.2.4.1 UV-Vis. studies

The UV-Vis. spectra for $Zn_{1-x}Fe_xS$ (x = 0.00, 0.01, 0.05 and 0.10) nanoparticles have been recorded between 280-450 nm as shown in Figure 3.12.

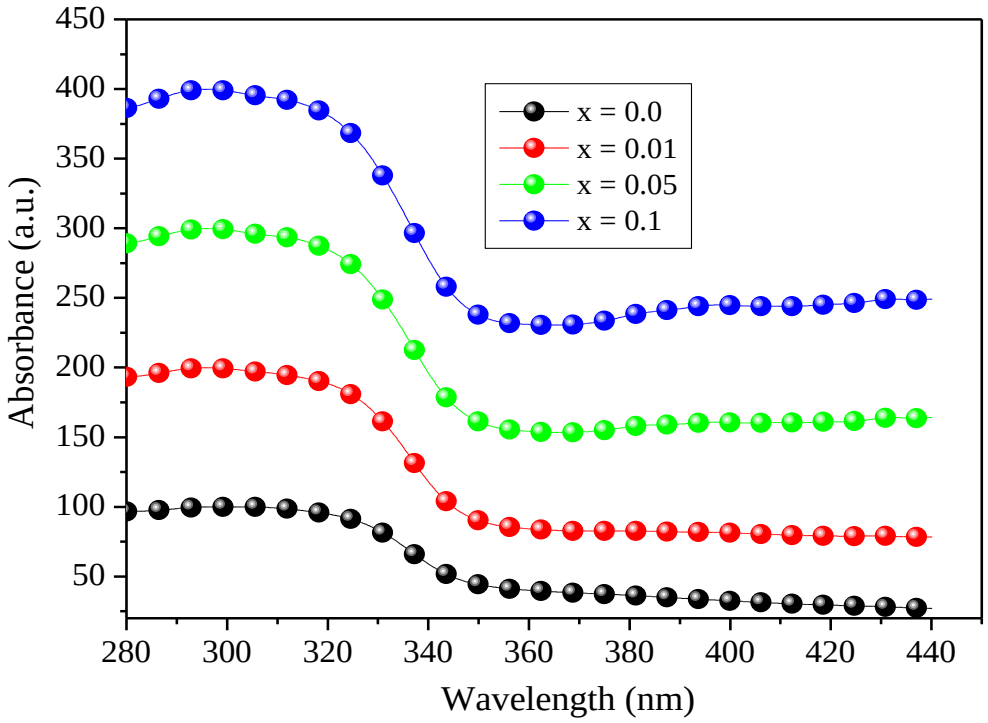


**Figure 3.12** UV-Vis. spectra of $Zn_{1-x}Fe_xS$ (x = 0.00, 0.01, 0.05, and 0.10) nanoparticles

The spectra indicating absorption edge at 319 nm in case of undoped ZnS nanoparticles, corresponding to a band gap of 3.88 eV - blue-shifted as compared to bulk ZnS (3.8 eV) - may be attributed to quantum confinement effects [166, 168]. The absorption edge is further blue-shifted in case of Fe-doped ZnS nanoparticles as compared to the undoped counterpart and it becomes more prominent as the dopant concentration is increased. The variation of absorption edge and corresponding change in energy band gap with Fe concentration in ZnS lattice is illustrated in Table 3.3.

**Table 3.3.** Variation of band gap with Fe concentration (x)

| Fe concentration (x) | Absorption edge (nm) | Band gap (eV) |
|---|---|---|
| 0.00 | 319 | 3.88 |
| 0.01 | 317 | 3.91 |
| 0.05 | 314 | 3.94 |
| 0.10 | 311 | 3.98 |

The blue-shift in absorption edge of Fe-doped ZnS nanoparticles as compared to undoped nanoparticles may be ascribed to the small size of $Fe^{2+}$ ions as compared to $Zn^{2+}$ ions. As the Fe doping concentration is increased the absorbance edge is again blue-shifted as compared to the undoped ZnS nanoparticles. It may be attributed to fact that the doped Fe ions are forming new energy levels in the ZnS energy band [173, 174]. The blue-shift may also be associated with the strain induced in ZnS lattice due to doping.

**3.1.2.4.2 PL studies**

The room temperature PL emission spectra of $Zn_{1-x}Fe_xS$ nanoparticles, obtained at excitation wavelength of 300 nm ($\lambda_{ex.}$ = 300 nm), recorded between 325-550 nm range, are shown in Figure 3.13. The emission spectra of $Zn_{1-x}Fe_xS$ (x = 0.00, 0.01, 0.05 and 0.10) nanoparticles exhibit two peaks, at 360 nm and 438 nm, respectively.

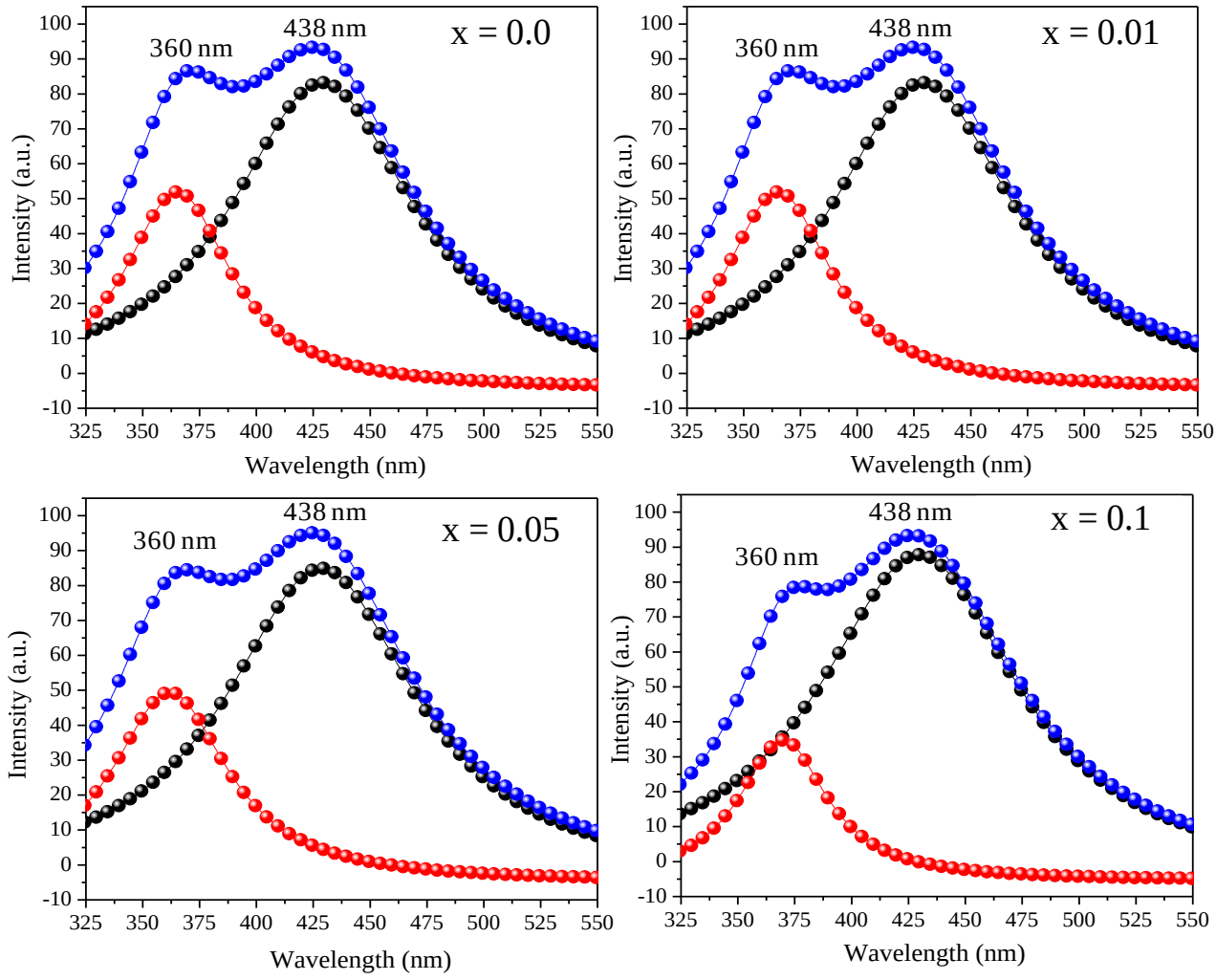


**Figure 3.13** PL spectra of $Zn_{1-x}Fe_xS$ (x = 0.00, 0.01, 0.05, and 0.10) nanoparticles

Wide peak at 360 nm may be associated band edge emission of ZnS; whereas, blue emission peak at 438 nm may be attributed to radiative recombination between sulphur vacancies related donor energy levels and purity of phase of host ZnS material. It has been observed that as the Fe concentration is increased, the corresponding PL intensity of ZnS nanoparticles is decreased, which indicates that $Fe^{2+}$ ions are acting as quenching centers [175]. In general in the PL process, an electron is stimulated from valence band of semiconductor, ZnS, to the conduction band which then decays via a normal recombination process to some defect or surface states existing within the valence and conduction bands [173]. In the Fe-doped ZnS, this electron can

occupy a tetrahedral cationic site and it may be captured by the $Fe^{2+}$ ions in intermediate state, leading to the decrease in PL intensity. The decrease in PL intensity at higher Fe concentration may also be attributed to decrease in defect states due to increased Fe concentration [74].

**3.1.2.5 Magnetic studies**

M-H curves of $Zn_{1-x}Fe_xS$ (x = 0.00, 0.01, 0.05 and 0.10) nanoparticles have been studied using VSM, recorded up to 1.5 T, as shown in Figure 3.14 (a, b). The M-H curves obtained indicate the magnetic behaviour induced in the Fe-doped ZnS nanoparticles with well resolved hysteresis loops, whereas, undoped ZnS nanoparticles indicate a diamagnetic type behaviour. The values of remanent magnetization at x = 0.01, 0.05 and 0.1 Fe-doping concentrations are 0.0005 emu/g, 0.0003 emu/g and 0.001 emu/g respectively, with low coercivity values. The increased ferromagnetic behaviour may be ascribed to the intrinsic coupling between the doped Fe atoms and not due to the aggregated Fe atoms in the ZnS lattice, as no secondary phases have been observed in XRD analysis. ZnS nanoparticles with x = 0.05 Fe-doping concentration exhibit a weak ferromagnetic or paramagnetic like behaviour [173]. Weak ferromagnetic character, in case of Ni-doped ZnS nanocrystals, has also been observed in literature [166]. Li et al. have reported a weak ferromagnetic character in x = 0.05 Fe-doped ZnS nanoparticles, termed as paramagnetic [176]. Bhattacharya et al. reported a weak ferromagnetic or superparamagnetic behaviour at same concentration, however, at lower temperature, 6 K [71]. The variation of magnetic moment (emu/g) and coercivity with Fe concentration has been depicted in Figure 3.13. Sambasivam et al. and Eryong et al. also reported the weak superparamagnetic character in Fe-doped ZnS nanoparticles, which is attributed to the small size of nanoparticles [74, 79]. The occurrence of superparamagnetism in other DMS materials has also been observed in the literature.

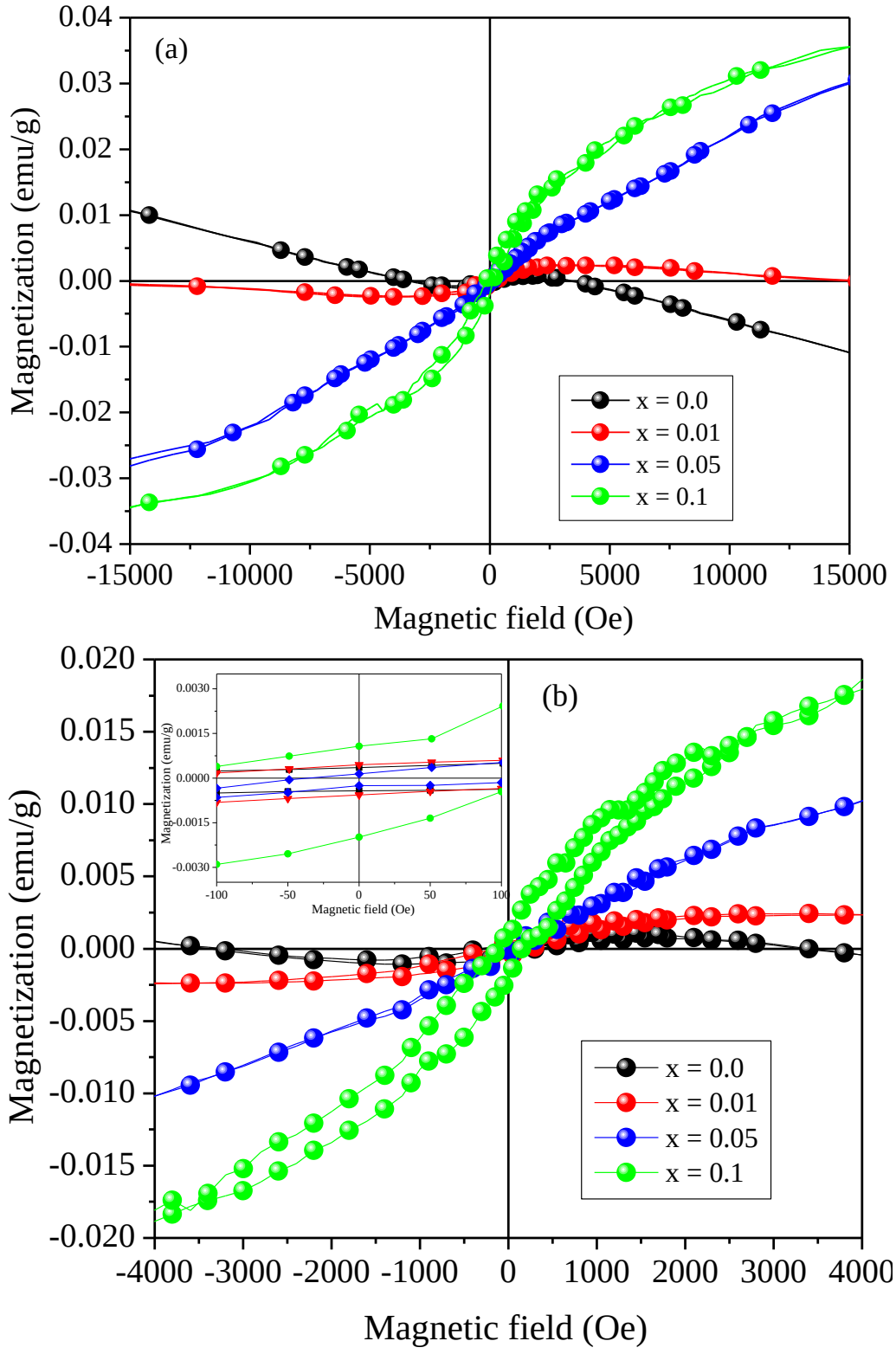


**Figure 3.14** M-H curves of $Zn_{1-x}Fe_xS$ (x = 0.00, 0.01, 0.05, and 0.10) nanoparticles (a) up to 1.5 T and (b) up to 4000 Oe [Inset: magnified M-H curves]

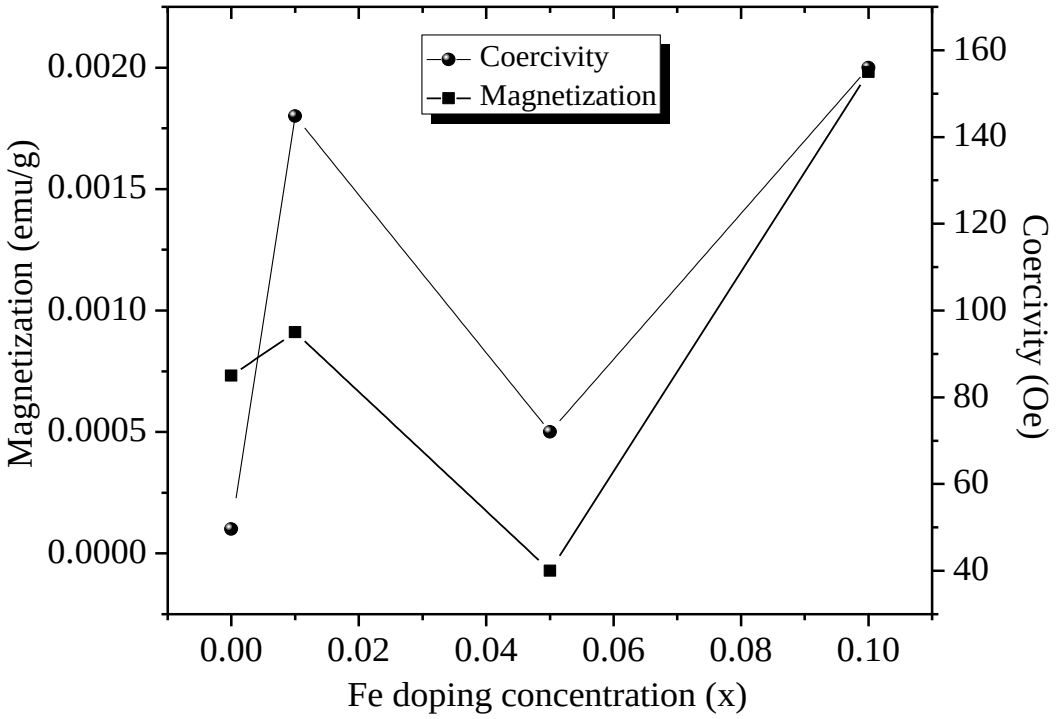


**Figure 3.15** Variation of magnetization and coercivity with Fe concentration

Norton et al. and Park et al. observed superparamagnetic character in Co-doped ZnO nanoparticles, associated with the small size of nanomaterials [171, 172]. Chen et al. observed the superparamagnetism, at high temperatures, in Mn-doped CdSe nanorods [177].

### 3.1.3 Co-doped ZnS nanoparticles

In this section, structural optical and magnetic properties of Co-doped ZnS nanoparticles with different Co concentrations (x = 0.00, 0.01, 0.05, and 0.1) have been studied. The $Zn_{1-x}Co_xS$ nanoparticles have been synthesized using technique as discussed in chapter 2. The solvent used in synthesizing these nanoparticles is ethanol. The resultant nanoparticles have been analyzed using TEM, HRTEM, EDS, XRD, UV-Vis., PL spectroscopy and VSM.

### 3.1.3.1 Morphological and elemental studies

Morphology of $Zn_{1-x}Co_xS$ nanoparticles have been studied using TEM images as shown in Figure 3.16. Size of $Zn_{1-x}Co_xS$ nanoparticles (x = 0.00 and 0.10) is found ~9 nm.

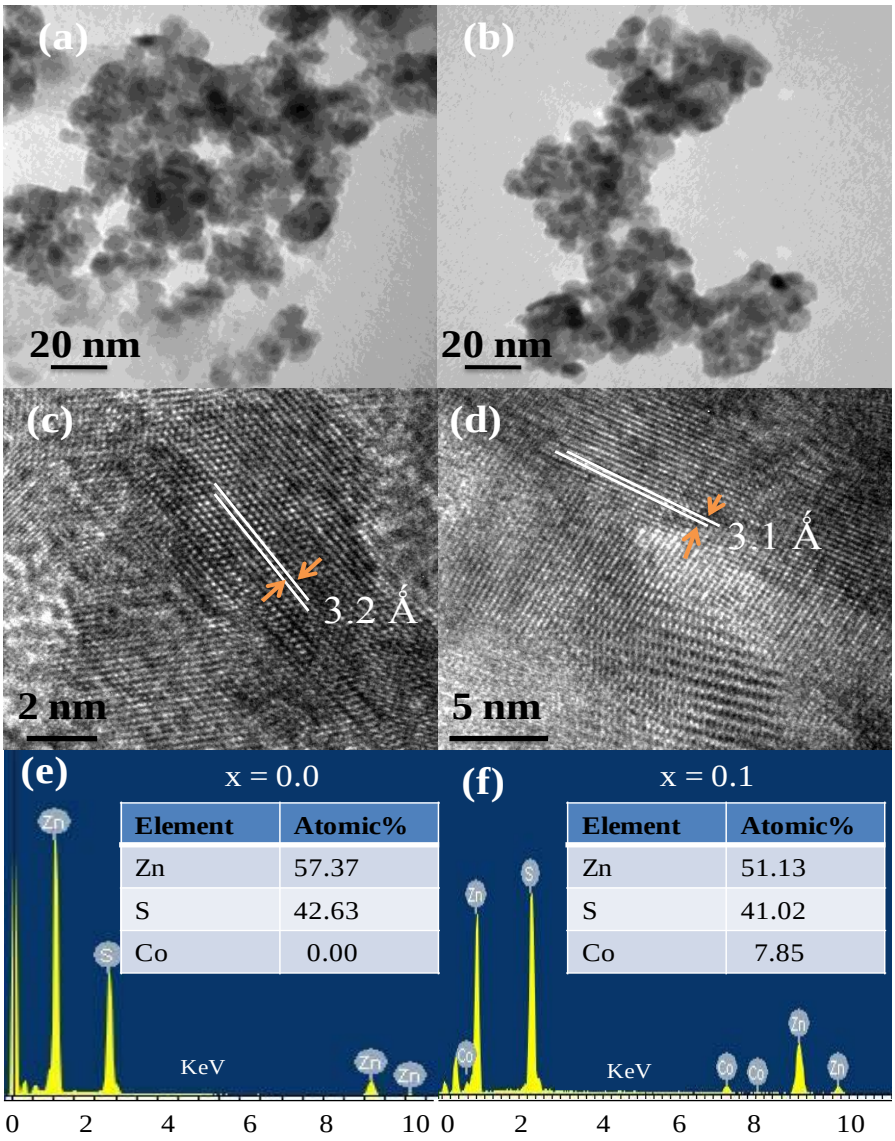


**Figure 3.16** TEM images of $Zn_{1-x}Co_xS$ nanoparticles at (a) x = 0.00 and (b) x = 0.10; HRTEM images at (c) x = 0.00 and (d) x = 0.10; EDS spectra at (e) x = 0.00 and (f) x = 0.10.

The nanoparticles with x = 0.00 and 0.10 have almost same size and morphology as indicated from images. The inter-atomic spacing values, as observed from HRTEM images in Figure 3.16 (c, d), have been found, 3.3 Å and 3.1 Å, for x = 0.00 and x = 0.10 concentrations, respectively.

The decrement in inter-atomic spacing values with Co-doping has been confirmed in XRD studies, which may be associated with strain induced in the ZnS lattice due to the different ionic radii of Co ions and ZnS ions. Figure 3.14 (e, f) shows the EDS spectra of $Zn_{1-x}Co_xS$ nanoparticles which indicates the presence of Co in the doped ZnS samples. The elemental composition of samples is illustrated in Table 3.4.

**Table 3.4** Elemental composition of $Zn_{1-x}Co_xS$ (x = 0.00, 0.01, 0.05 and 0.10) nanoparticles

| Co concentration (x) | Atomic% |
|---|---|
| 0.00 | Zn = 57.37, S = 42.63, Co = 0.00 |
| 0.01 | Zn = 55.40, S = 43.72, Co = 0.87 |
| 0.05 | Zn = 51.24, S = 44.74, Co= 4.02 |
| 0.10 | Zn = 51.13, S = 41.02, Co = 7.85 |

The observed doped amount of Co has been found to be less as compared to actual doped percentage, which again may be ascribed to the excessive washings of samples due to which the non-reactant Co particles may have been washed away [178].

### 3.1.3.2 Structural studies

Structural properties and phase analyses have been carried out using the XRD patterns as shown in Figure 3.17. Peaks have been obtained at 2θ = (111), (200), (220) and (311) corresponding to the Bragg's angles 28.65°, 33.05°, 47.95° and 57.13°, respectively, which accord well with the JCPDS data card (JCPDS 80-0020) indicating the cubic phase of the synthesized nanoparticles. Broadening in the XRD peaks indicate the nanometer regime of $Zn_{1-x}Co_xS$ nanoparticles. No extra peak of impurity phase or other compound has been observed in the XRD patterns, indicating the single phase of $Zn_{1-x}Co_xS$ nanoparticles, supporting the substitution of Co ions in ZnS lattice. The average particle size is estimated from Scherrer's formula has been found to be ~10.41 nm, which accords well with TEM size [157].

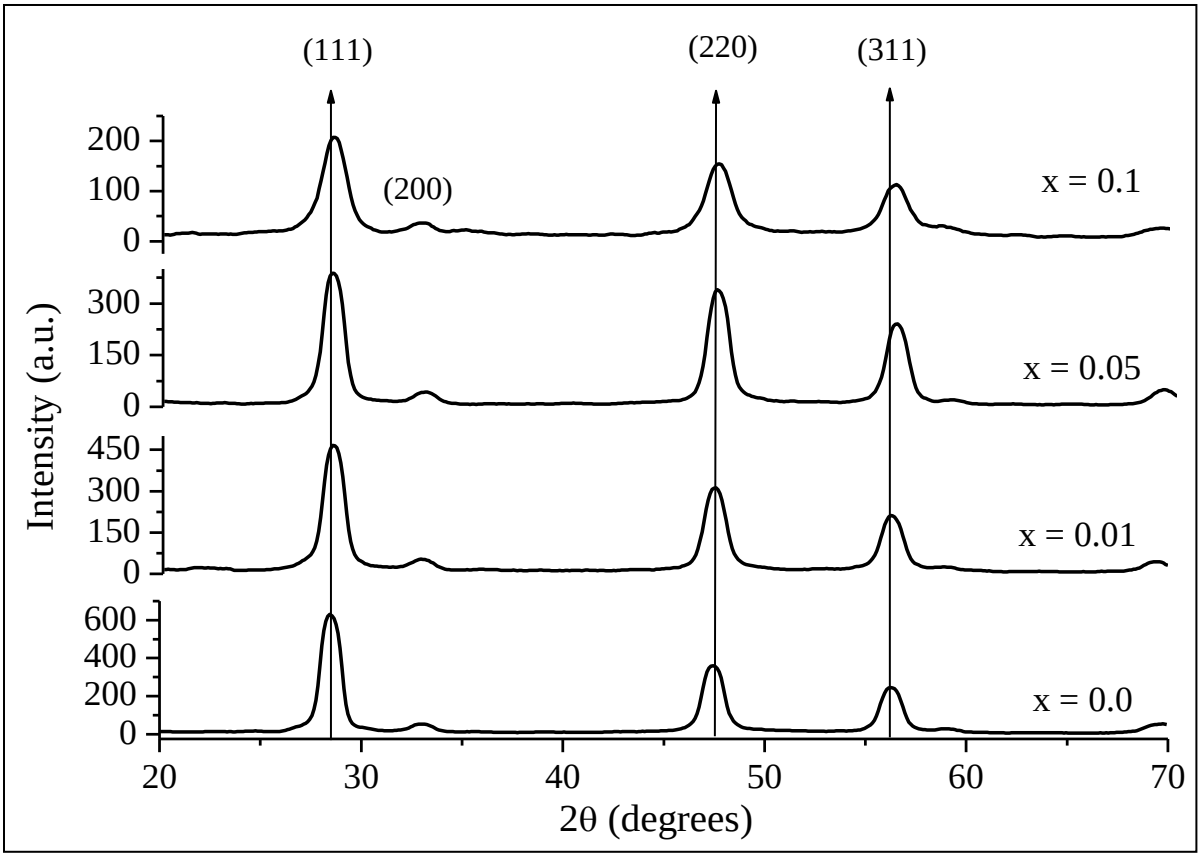


**Figure 3.17** XRD patterns of $Zn_{1-x}Co_xS$ (x = 0.00, 0.01, 0.05, and 0.10) nanoparticles

The intensity of the peaks is found reduced with increased Co doping concentration, indicating the deterioration of structural quality of ZnS. Shifting of XRD peaks towards higher Bragg's angles again support the doping of Co in ZnS [177]. The size and strain induced in the lattice have been obtained using W-H plots. W-H plots for different Co concentrations have been plotted as shown in Figure 3.18. W-H plots indicate a negative slope indicating compressive strain in the lattice due to Co doping. The slope is found increased as the doping concentration is increased indicating that lattice is under strain with increased doping concentration.

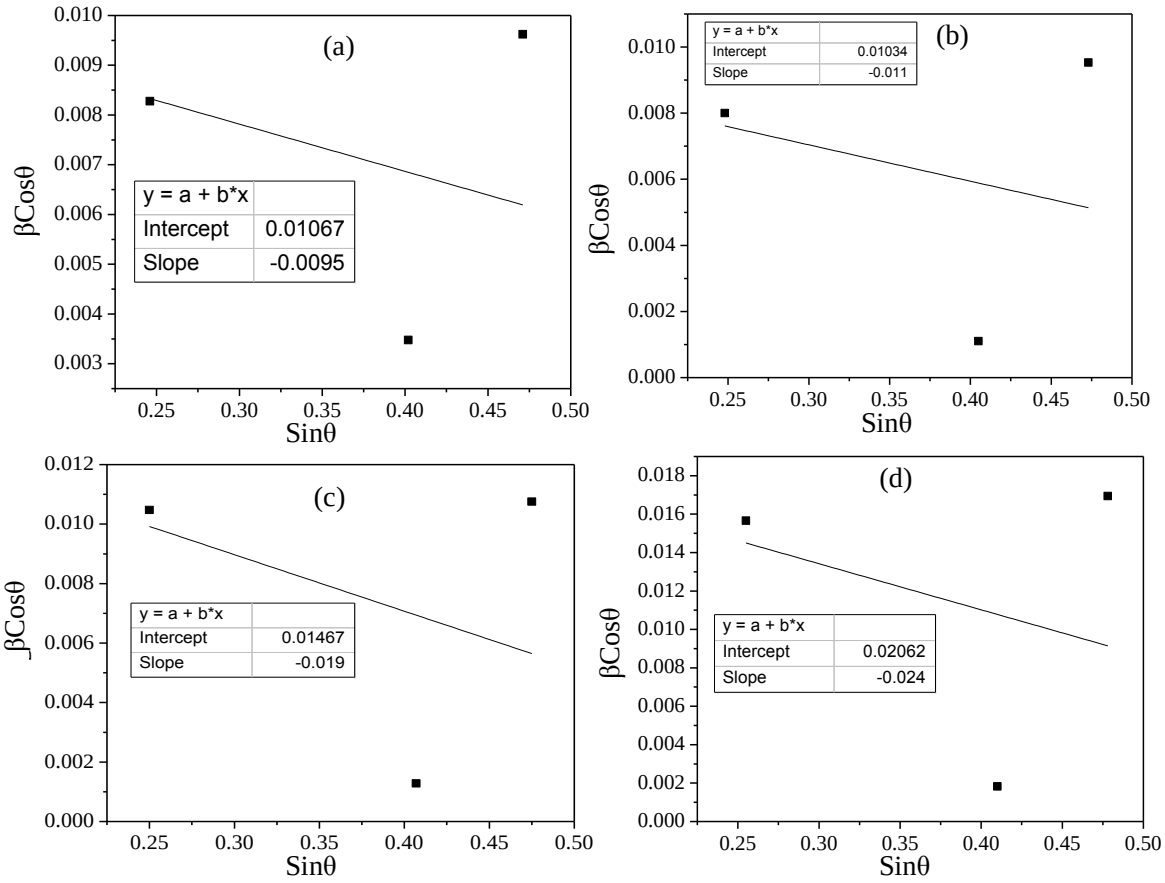


**Figure 3.18** W-H plots of $Zn_{1-x}Co_xS$ nanoparticles at (a) x = 0.00, (b) x = 0.01, (c) x = 0.05 and (d) x = 0.10

**Table 3.5** Structural parameters of $Zn_{1-x}Co_xS$ (x = 0.00, 0.01, 0.05, and 0.10) nanoparticles

| Co doping (x) | 2θ | | | Lattice constant (Å) | d-spacing (Å) | Crystallite size (nm) | | Strain (ε) |
|---|---|---|---|---|---|---|---|---|
| | (111) | (220) | (311) | | | Debye Scherrer's equation | W-H plot | |
| 0.0 | 28.29 | 47.25 | 56.28 | 5.45 | 3.15 | 10.41 | 10.03 | -0.0016 |
| 0.01 | 28.43 | 47.41 | 56.39 | 5.36 | 3.11 | 11.55 | 11.16 | -0.0027 |
| 0.05 | 28.51 | 47.43 | 56.54 | 5.31 | 3.10 | 10.36 | 9.45 | -0.0047 |
| 0.10 | 28.58 | 47.52 | 56.64 | 5.28 | 3.08 | 9.88 | 8.72 | -0.0060 |

Different lattice parameters along with the size and strain induced at different Fe-doping concentrations are presented in Table 3.5. Decrease in the lattice parameters may be ascribed to strain induced in ZnS lattice with insertion of Co ions in ZnS lattice as the ionic radii of Co ions differs from replacing Zn ions.

### 3.1.3.3 Optical studies

The optical properties have been analyzed using UV-Vis. and PL studies. The detailed optical properties of $Zn_{1-x}Co_xS$ nanoparticles are given below:

#### 3.1.3.3.1 UV-Vis. studies

UV-Vis. spectra of $Zn_{1-x}Co_xS$ nanoparticles have been shown in Figure 3.19. The spectra indicate blue shift in absorption edge in $Zn_{1-x}Co_xS$ nanoparticles as compared to bulk ZnS.

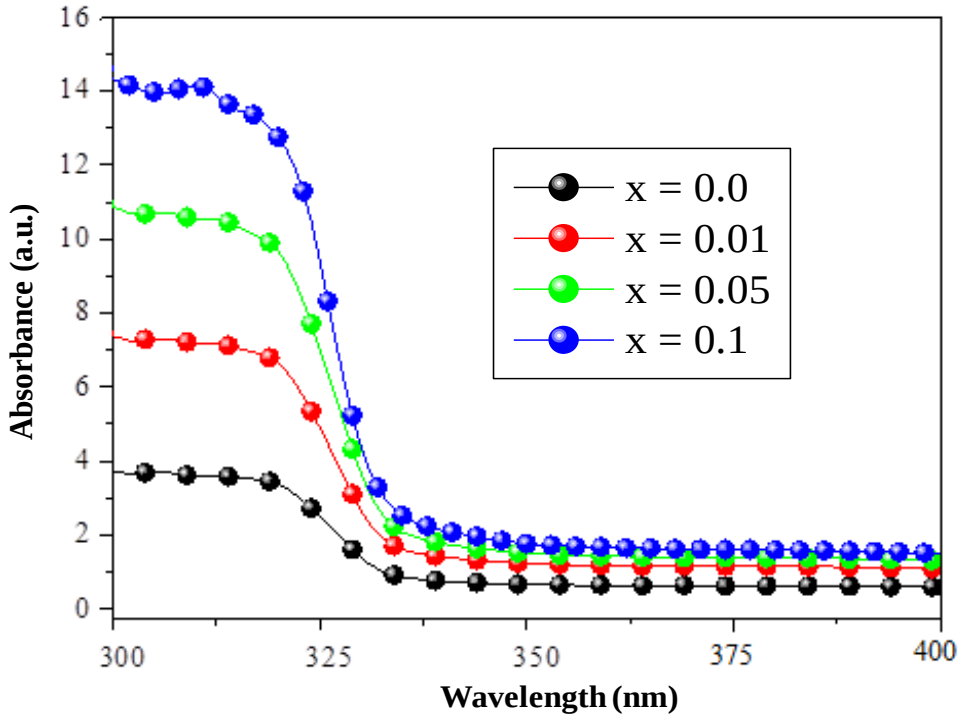


**Figure 3.19** UV-Vis. spectra of $Zn_{1-x}Co_xS$ (x = 0.00, 0.01, 0.05, and 0.10) nanoparticles

Maximum absorbance edge in case of undoped ZnS nanoparticles has been found at 320 nm, corresponding to the band gap of 3.86 eV - blue-shifted as compared to bulk ZnS. The blue-shift in undoped ZnS nanoparticles may be ascribed to quantum confinement effects [168]. Also, as the Co concentration in ZnS nanoparticles is increased, the absorbance edge is found to be blue-shifted as compared to the undoped ZnS nanoparticles. The maximum absorption edge appears at 313 nm for x = 0.10 Co-doped ZnS nanorods corresponding to a band gap of 3.95 eV. This

behaviour has been illustrated in Figure 3.20. The blue shift in Co-doped ZnS nanoparticles may be attributed to the fact that the radii of Co ions are smaller as compared to the replaced Zn ions. It may also be attributed to fact that the doped Fe ions are forming new energy levels in the ZnS energy band [178]. It again supports the replacement of Zn ions with doped Co ions in the ZnS lattice. The blue-shift may also be associated with the strain induced in ZnS lattice due to doping.

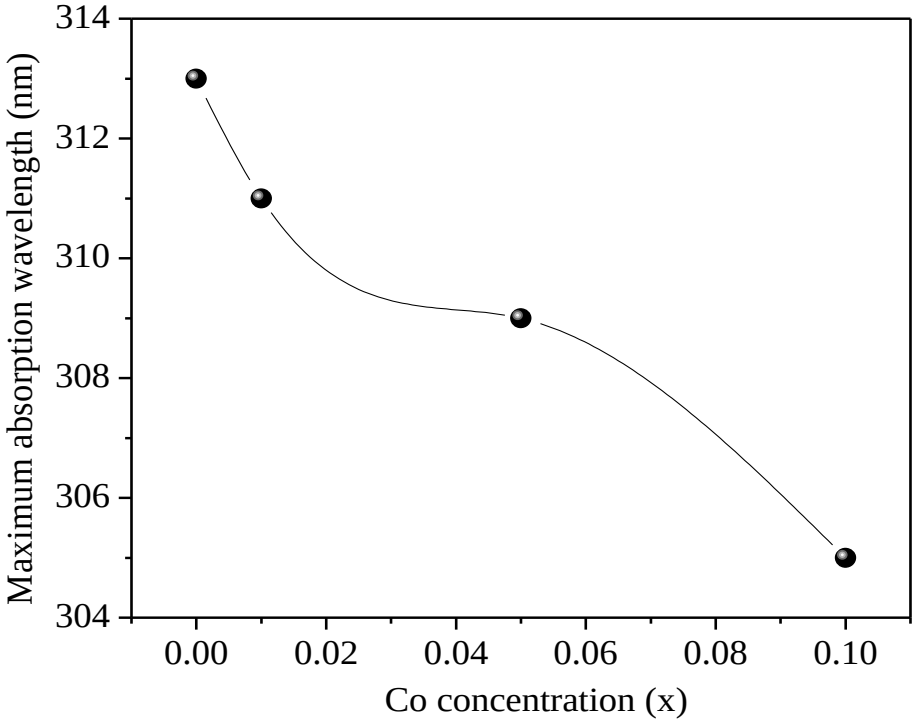


**Figure 3.20** Variation of maximum absorption with Co concentration

**3.1.3.3.2 PL studies**

The room temperature PL emission spectra obtained, at excitation wavelength of 280 nm ($\lambda_{ex.}$= 280 nm), recorded between 350-600 nm are shown in Figure 3.21. The spectra obtained indicate the peak centered at 450 nm and 525 nm due to blue and yellow emission respectively. Broad emission band exhibited at 450 nm may be ascribed to surface defect states originating due to sulphur vacancies [179]. The blue emission peak may ascribe to radiative recombination between sulphur vacancies related donor energy levels and purity phase of host ZnS material [180].

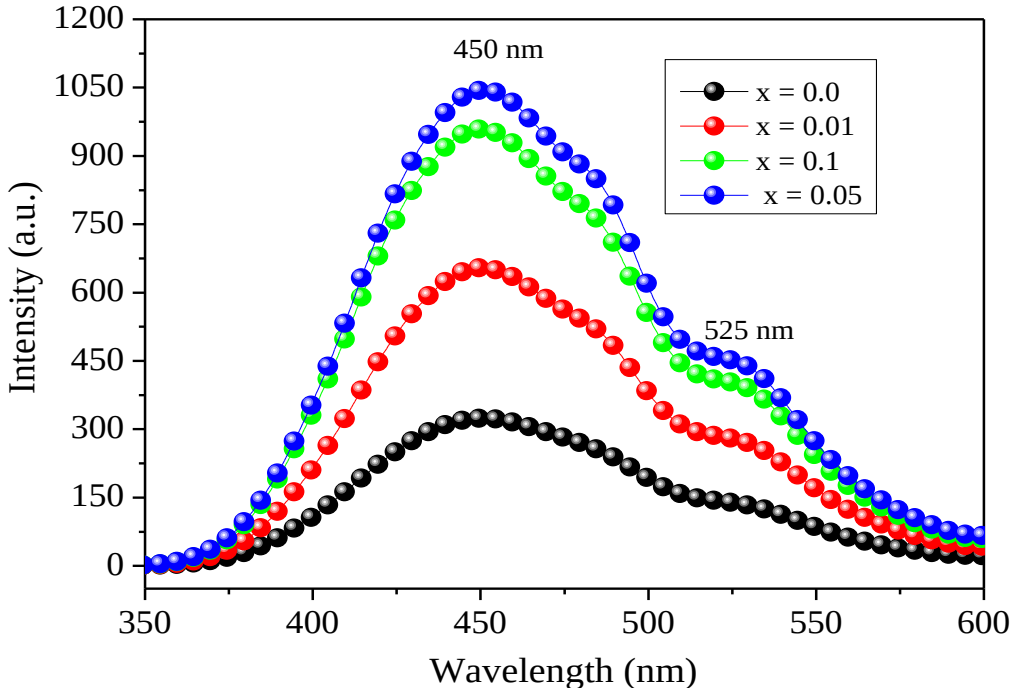


**Figure 3.21** PL spectra of $Zn_{1-x}Co_xS$ (x = 0.00, 0.01, 0.05, and 0.10) nanoparticles

Another peak centered at 525 nm may be associated with self activated zinc vacancies of synthesized ZnS nanoparticles [181]. The photoluminescence intensity increases with the doping of cobalt ions at x = 0.01 and x = 0.05 concentrations, but it reduces as the Co concentration is increased to x = 0.10. This behaviour has been demonstrated in Figure 3.19. The enhancement of photoluminescence intensity may be ascribed to creation of new radiation centers or size reduction caused due to Co doping [182]. As the Co concentration is increased up to x = 0.10, the doped Co ions interfere with the radiative recombination, which overshadows the effect of creating new radiation centers, resulting in the quenching of fluorescence intensity at higher doping concentrations [166, 170, 178].

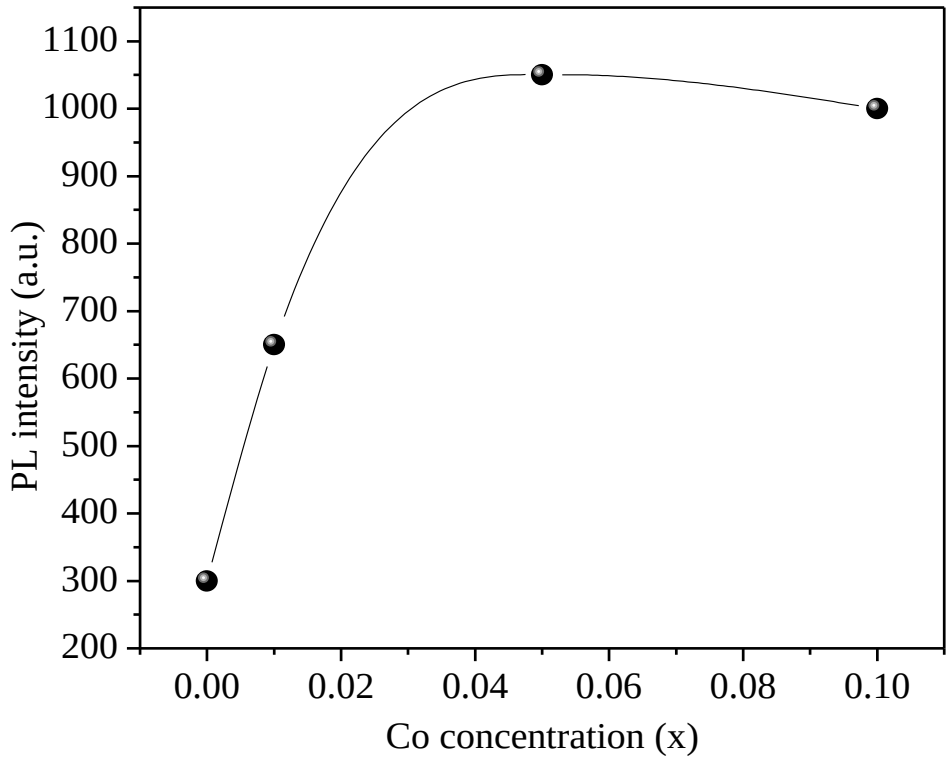


**Figure 3.22** Variation of PL intensity with Co concentration

### 3.1.3.4 Magnetic studies

Magnetic behaviour of Co-doped ZnS nanoparticles has been analyzed using M-H curves obtained using VSM up to 1.5 T. The M-H curves, obtained at room temperature, are shown in Figure 3.23 (a, b). The M-H curves indicate the magnetic behaviour induced in the $Zn_{1-x}Co_xS$ nanoparticles. Increase in Co concentration up to x = 0.10 induces increased ferromagnetic character at lower magnetic fields, however, no saturation has been observed till 1.5 T. The variation of coercivity and remanent values with Co concentrations has been illustrated in Figure 3.24. Decrease in coercivity values indicating the soft magnet character of the Co-doped ZnS nanoparticles. The retentivity is reduced at x = 0.01 Co concentration, but, as the Co concentration is increased to x = 0.05 and 0.10, a substantial increase has been observed in retentivity of ZnS nanoparticles as compared to x = 0.01 Co concentration.

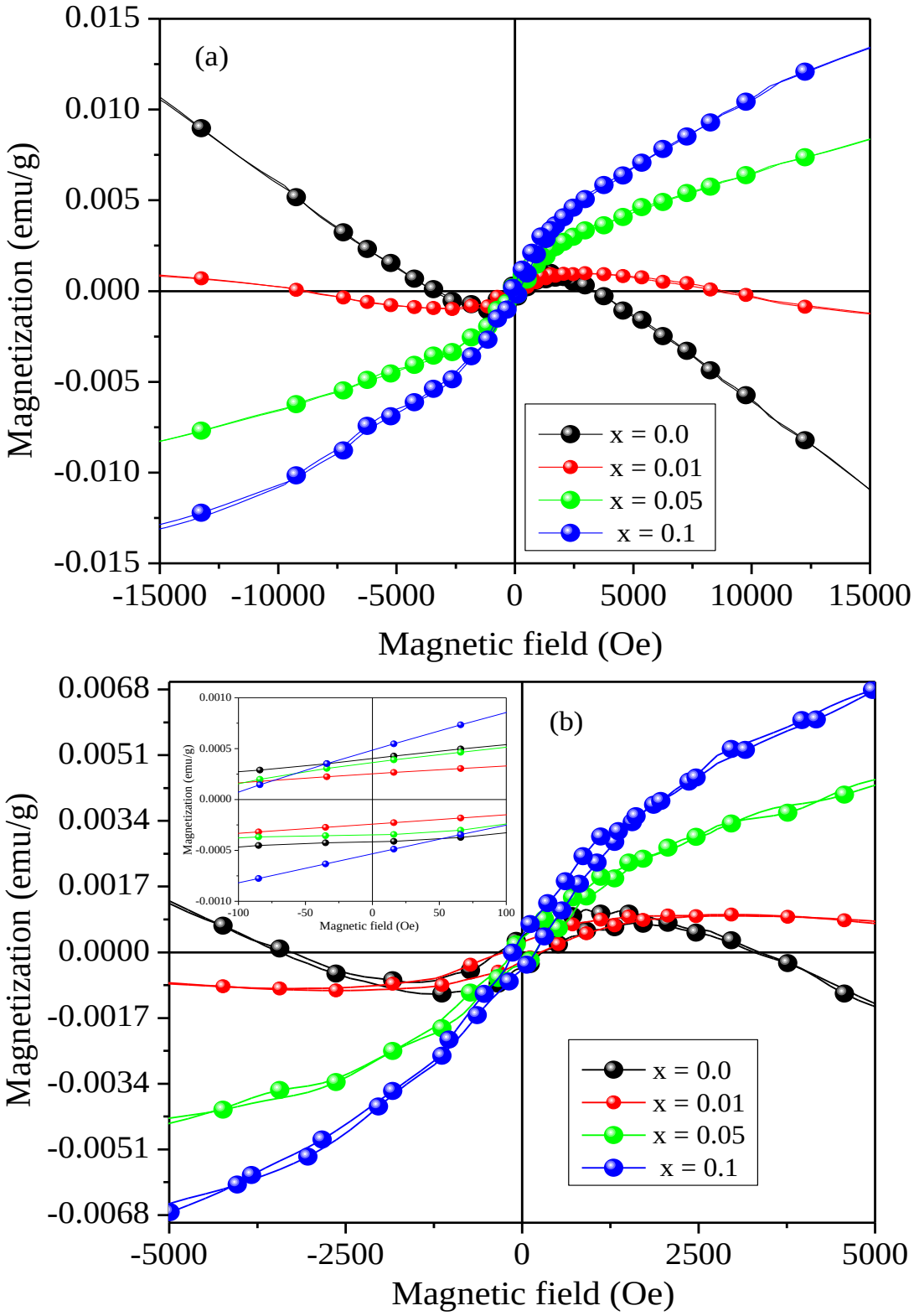


**Figure 3.23** M-H curves of $Zn_{1-x}Co_xS$ (x = 0.00, 0.01, 0.05, and 0.10) nanoparticles (a) up to 1.5 T and (b) up to 5000 Oe [Inset: magnified view of M-H curves]

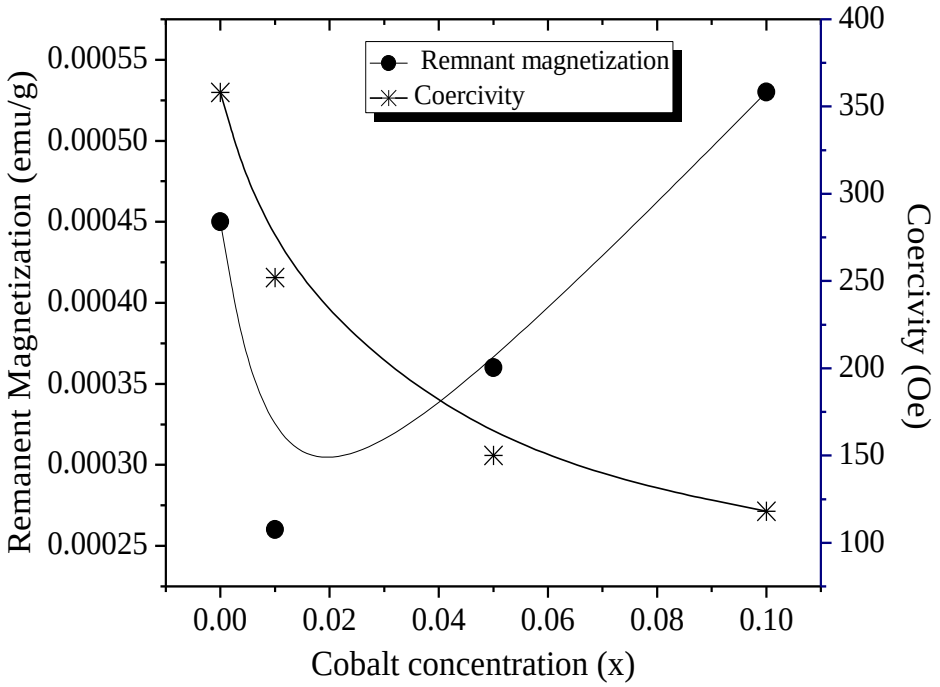


**Figure 3.24** Variation of remanent magnetization and coercivity with Co concentration in ZnS nanoparticles

The indication of ferromagnetic character with the insertion of Co ions in ZnS matrix supports the presence of Co in ZnS matrix. The induced ferromagnetism at lower concentration may be associated with super-exchange interaction between the doped $Co^{2+}$ ions whereas, at higher Co concentrations it may be ascribed to direct exchange as the distance between moments is reduced at higher concentrations [27]. The possibility of magnetism due to aggregated Co atoms can be ruled out as no secondary phases have been observed in XRD analysis [178]. The room temperature ferromagnetism may be ascribed to the sulphur vacancies and zinc interstitials [183, 184]. The results obtained contradict the earlier reports, where it has been found that the ferromagnetic character is decreased with increased cobalt ions concentrations due to antiferromagnetic interactions [76]. However, in some reports, at higher Co ions concentrations, a ferromagnetic behaviour is observed at room temperature [185].

To summarize, Table 3.6 provides a comparative chart of properties of Ni, Fe and Co-doped ZnS nanoparticles at different transition metals concentrations.

**Table** 3.6 Comparative chart of various properties of (Ni, Fe, Co)-doped ZnS nanoparticles

| **Sample** | **Ni-ZnS** | | | | **Fe-ZnS** | | | | **Co-ZnS** | | | |
|---|---|---|---|---|---|---|---|---|---|---|---|---|
| **Doping (x)** **Properties** | 0.00 | 0.01 | 0.05 | 0.10 | 0.00 | 0.01 | 0.05 | 0.10 | 0.00 | 0.01 | 0.05 | 0.10 |
| **Solvent** | De-ionized water | | | | EN and ethylene glycol (1:5) | | | | Ethanol | | | |
| **Average size (nm)** | ~5 | | | | ~12 | | | | ~10 | | | |
| **Doping (%) observed** | 0.0 | 0.82 | 3.72 | 7.06 | 0.0 | 0.73 | 4.05 | 7.40 | 0.0 | 0.87 | 4.02 | 7.85 |
| **Structure** | Cubic | | | | Hexagonal | | | | Cubic | | | |
| **Band gap (eV)** | 3.90 | 3.94 | 4.0 | 4.06 | 3.88 | 3.91 | 3.94 | 3.98 | 3.86 | 3.89 | 3.92 | 3.95 |
| **PL intensity (w.r.t. undoped)** | - | Increase | Decrease | Decrease | - | Decrease | Decrease | Decrease | - | Increase | Increase | Decrease |
| **Magnetiza -tion (emu/g)** | 0.002 | 0.0033 | 0.0052 | 0.0178 | 0.002 | 0.006 | 0.031 | 0.038 | 0.002 | 0.03 | 0.01 | 0.014 |

### 3.2 Transition metals doped ZnS nanorods

#### 3.2.1 Undoped and Ni-doped ZnS nanorods

This section deals with the morphological, structural, optical and magnetic properties of $Zn_{1-x}Ni_xS$ (x = 0.00, 0.01, 0.05 and 0.10) nanorods. The Ni-doped ZnS nanorods have been synthesized as discussed in chapter 2. The synthesized nanorods have been analyzed using TEM, HRTEM, EDS, XRD, UV-Vis., PL spectroscopy and VSM techniques.

##### 3.2.1.1 Morphological studies

The undoped ZnS nanorods (x = 0.00) and $Zn_{1-x}Co_xS$ (x = 0.10) samples indicate cylindrical nanorods as shown in Figure 3.25(a) and Figure 3.25(b) respectively.

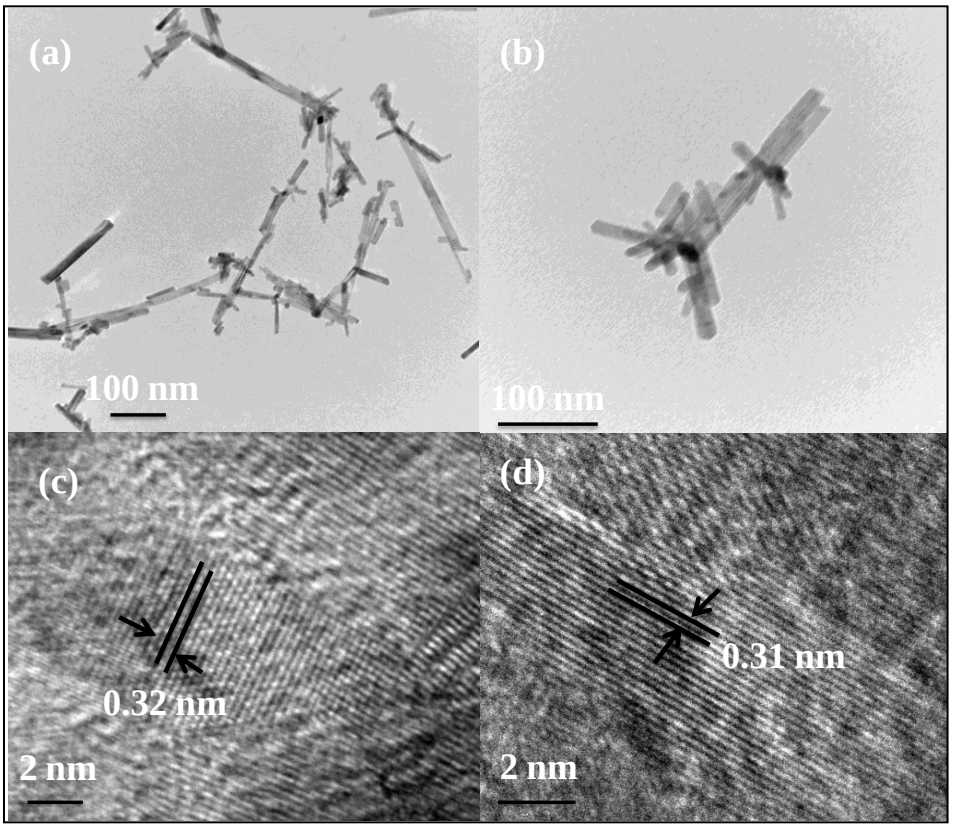


**Figure 3.25** TEM images of $Zn_{1-x}Ni_xS$ nanorods (a) x = 0.00 (b) x = 0.10; HRTEM images of (c) x = 0.00 and (d) x = 0.10 Ni concentrations

The variation in length ranges between 50-300 nm and diameter ~10 nm. TEM images indicate that morphologically the undoped and Ni-doped ZnS nanorods are similar [177]. HRTEM

images of undoped and Ni-doped ZnS nanorods have been shown in Figure 3.25 (c, d). The HRTEM images indicate sharp lattice fringes in undoped and Ni-doped ZnS nanorods indicate high crystalline nature of synthesized nanorods. Lattice spacing values, 0.32 nm and 0.31 nm, for undoped and Ni doped ZnS nanorods, accord well with (002) plane of standard ZnS JCPDS card no. 36-1450.

### 3.2.1.2 Elemental studies

EDS analysis has been performed to confirm the presence of Ni in ZnS nanorods samples. The EDS patterns exhibiting the elements present in undoped and doped ZnS nanorods are shown in Figure 3.26. Inspecting the spectra, it has been observed that Ni is present in the doped ZnS nanorods; however, the observed amount is less than the actual doped amount [186].

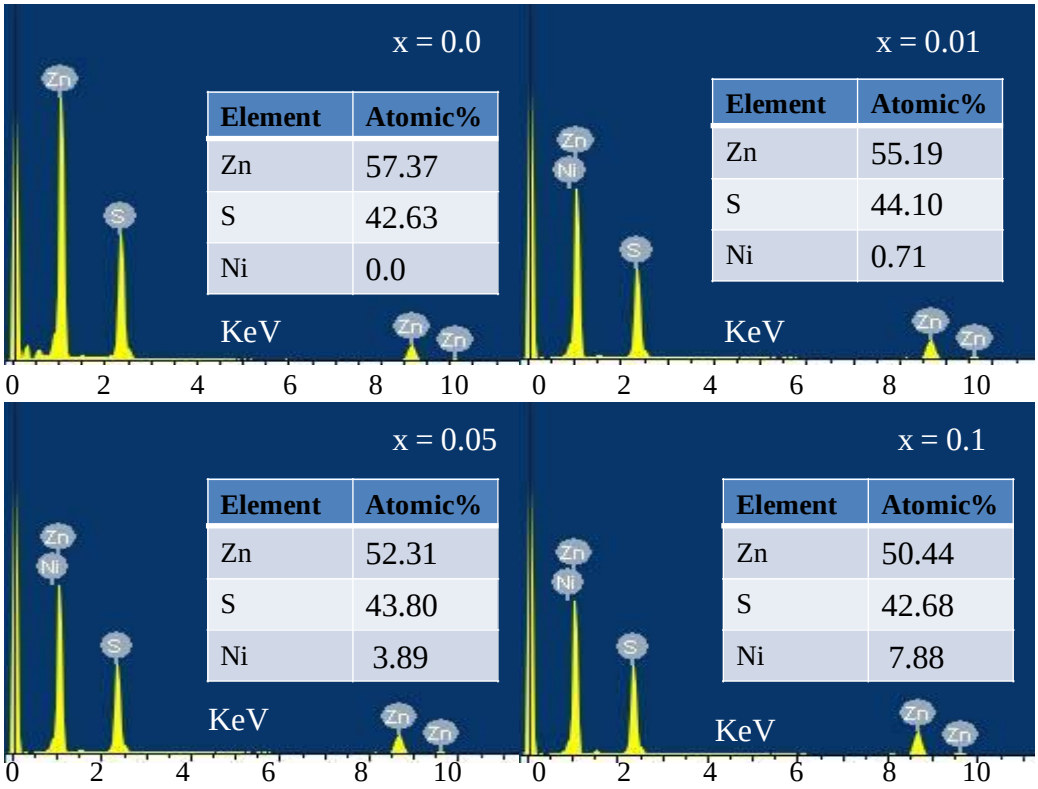


**Figure 3.26** EDS patterns of $Zn_{1-x}Ni_xS$ (x = 0.00, 0.01, 0.05 and 0.10) nanorods

In case of x = 0.00, 0.01, 0.05, and 0.10 Ni-concentrations, the observed amount of Ni has been found to be 0.71%, 3.89% and 7.88%, respectively, as shown in Table 3.7.

**Table 3.7** Elemental distribution in $Zn_{1-x}Ni_xS$ (x = 0.00, 0.01, 0.05 and 0.10) nanorods

| Ni concentration (x) | Elemental composition |
|---|---|
| 0.00 | Zn = 57.37, S = 42.63, Ni = 0.00 |
| 0.01 | Zn = 55.19, S = 44.10, Ni = 0.71 |
| 0.05 | Zn = 52.31, S = 43.80, Ni = 3.89 |
| 0.10 | Zn = 50.44, S = 42.68, Ni = 7.88 |

The reason for the decrease in observed Ni content may be due to the fact that Ni atoms, not substituted in the ZnS lattice or non-reacted, may have been washed away during the washing of samples.

### 3.2.1.3 Structural studies

The XRD patterns of undoped and Ni-doped nanorods are shown in Figure 3.27. The diffraction peaks have been observed at 2θ = 26.5°, 28.8°, 30.54°, 39.77°, 47.6°, 51.83° and 56.45° corresponding to the planes (100), (002), (101), (102), (110), (103), and (112) respectively. These planes can be indexed to wurtzite phase (JCPDS card no. 36-1450) with lattice parameters, a = 3.86 and, c = 6.30 in case of undoped ZnS nanorods. No extra peaks of secondary phases have been indicated in Ni-doped samples, supporting that the dopant, Ni, has been substituted in the ZnS lattice [186]. The XRD peaks have been found shifted slightly towards higher Bragg's angles. The preferential growth direction about a plane can be obtained by calculating the texture coefficient by using the equation [187]:

$$TC(hkl) = \frac{I(hkl)}{I'(hkl)}\left[\frac{1}{n}\Sigma\frac{I(hkl)}{I'(hkl)}\right]^{-1}$$

where, *TC(hkl)* is the texture coefficient along *(hkl)* plane, $I'(hkl)$ is intensity of standard JCPDS peaks, *I(hkl)* is the intensity of corresponding observed XRD peaks, and '*n*' is the number of peaks in the XRD patterns.

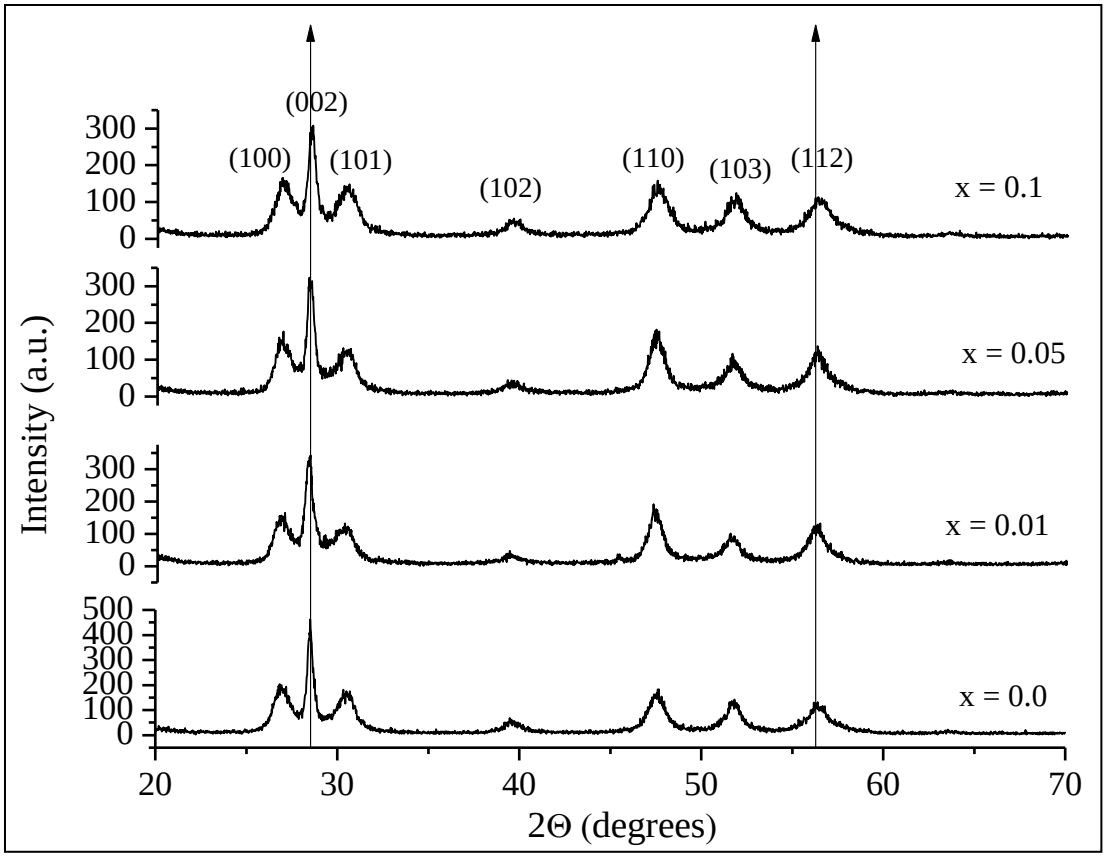


**Figure 3.27** XRD patterns of $Zn_{1-x}Ni_xS$ (x = 0.000, 0.01, 0.05 and 0.1) nanorods

From calculations, it has been observed that the value of *TC(002)* is maximum, indicating it to be a preferred direction of growth. For wurtzite structure, the lattice parameters have been calculated using the raltion:

$$\frac{1}{d^2} = \frac{4}{3}\left[\frac{h^2 + hk + k^2}{a^2}\right] + \frac{l^2}{c^2}$$

where, (hkl) are Miller indices, 'd' is interplanar spacing. W-H plots for undoped and Ni-doped ZnS nanorods have been shown in Figure 3.28. W-H plots indicate negative slopes in all samples which again indicate that in case of Ni-doped ZnS nanorods the lattice is under compressive strain.

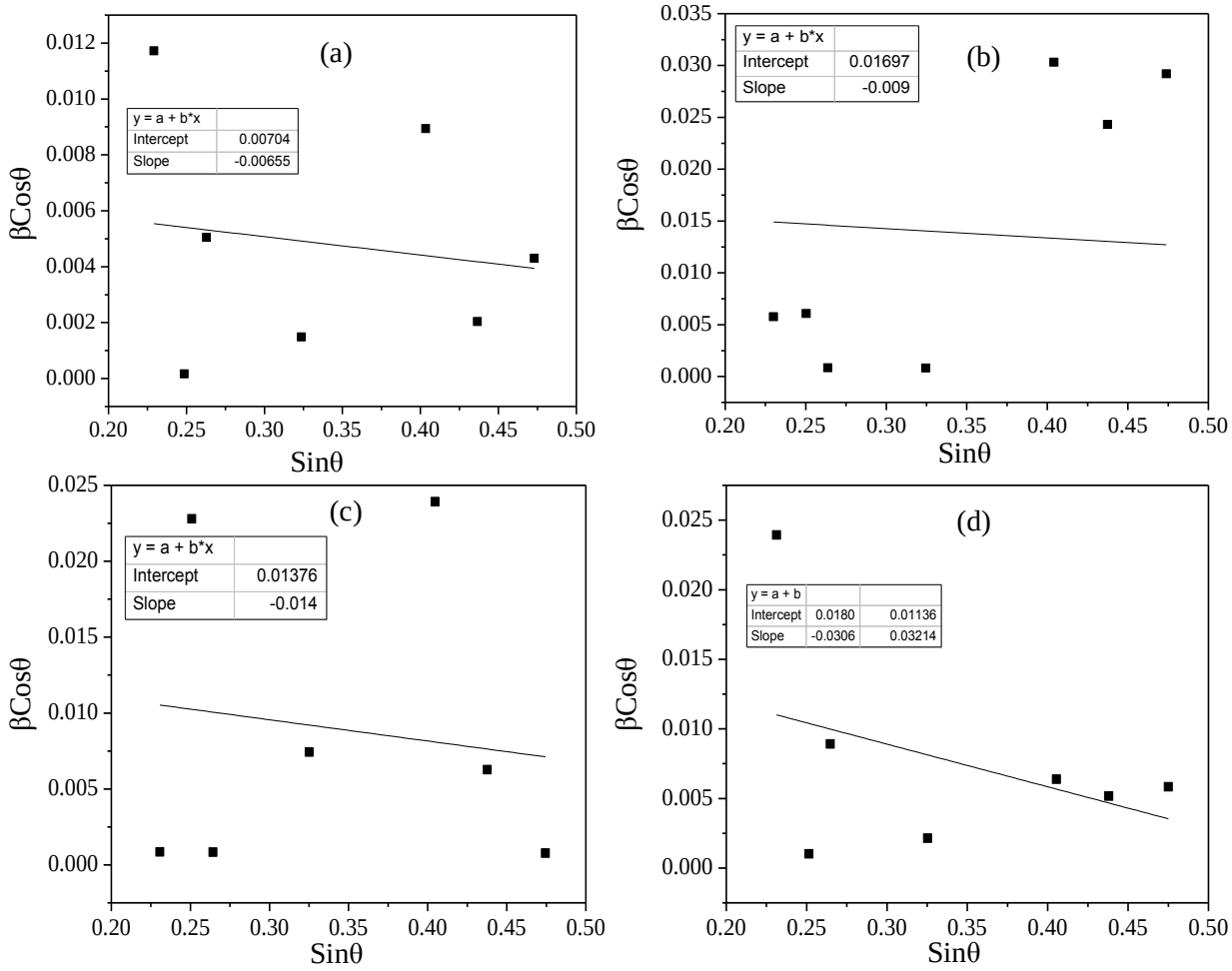


**Figure 3.28** W-H plots of $Zn_{1-x}Ni_xS$ nanorods at (a) x = 0.00 (b) x = 0.01, (c) x = 0.05 and (d) x = 0.10

Various structural parameters calculated are shown in Table 3.8.

**Table 3.8** Structural parameters of $Zn_{1-x}Ni_xS$ nanorods (*indicated few 2θ positions)

| Ni doping (x) | 2θ* | | | Lattice constant (Å) | d-spacing (Å) | Crystallite size (nm) | | Strain (ε) |
|---|---|---|---|---|---|---|---|---|
| | (002) | (110) | (112) | | | Scherrer's equation | W-H plot | |
| 0.00 | 28.34 | 47.21 | 56.14 | a = 3.86, c = 6.30 | 3.15 | 20.88 | 19.69 | -0.0012 |
| 0.01 | 28.38 | 47.27 | 56.19 | a = 3.82, c = 6.28 | 3.14 | 18.78 | 18.21 | -0.0022 |
| 0.05 | 28.47 | 47.33 | 56.31 | a = 3.80, c = 6.26 | 3.13 | 14.14 | 13.16 | -0.0034 |
| 0.10 | 28.50 | 47.46 | 56.42 | a = 3.74, c = 6.18 | 3.10 | 12.86 | 11.60 | -0.0052 |

From Table 3.8, it is clear that as the doping concentration is increased, there results a slight shift in the peak position in case of Ni-doped nanorods, and the values of lattice constants also register a decreasing trend, indicating that the Ni ions replaced the Zn ions in the lattice. Reduced lattice parameters and shifting of XRD towards higher Bragg's angles may be attributed to smaller ionic radii of Ni atoms replacing the comparatively larger Zn ions in the ZnS lattice; hence lattice is under compressive strains [186].

#### 3.2.1.4 Optical studies

The optical properties have been analyzed using UV-Vis. and PL studies. The detailed optical properties of $Zn_{1-x}Ni_xS$ (x = 0.00, 0.01, 0.05 and 0.10) nanorods are given below:

##### 3.2.1.4.1 UV-Vis. studies

The UV-Vis. spectra of $Zn_{1-x}Ni_xS$ (x = 0.00, 0.01, 0.05 and 0.10) nanorods have been recorded between 300-450 nm range. The UV-Vis. patterns obtained are shown in Figure 3.29.

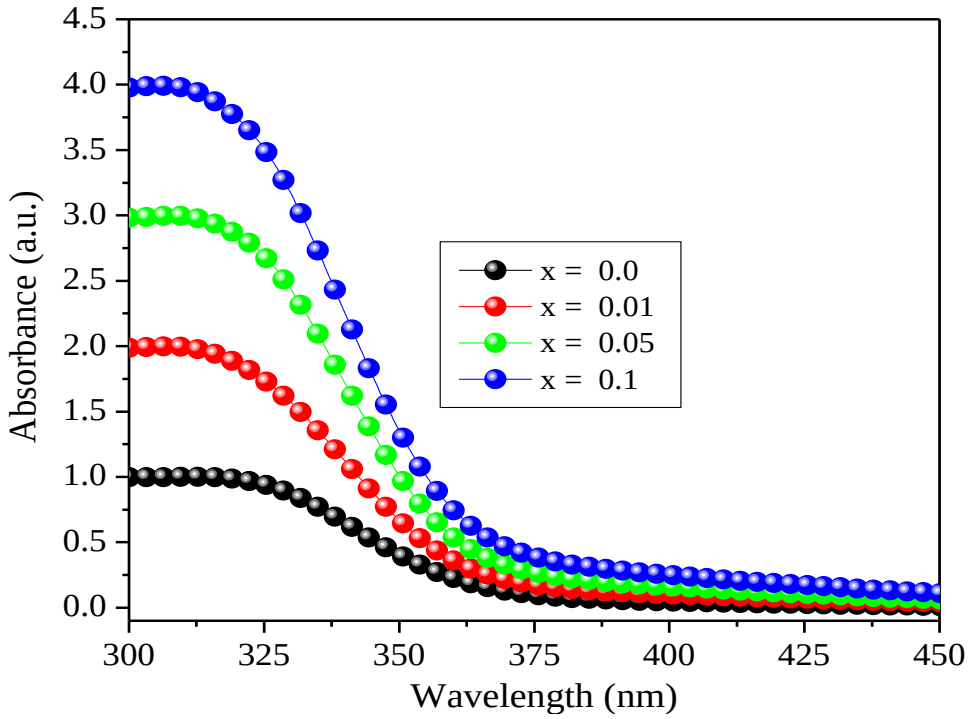


**Figure 3.29** UV-Vis. spectra of $Zn_{1-x}Ni_xS$ (x = 0.00, 0.01, 0.05 and 0.10) nanorods

Maximum absorbance recorded at 325 nm, in case of undoped ZnS nanorods, corresponding to the band gap of 3.81 eV, blue-shifted as compared to bulk counterpart. Further, as the Ni-doping is increased, the absorbance edge is blue-shifted as compared to undoped ZnS counterparts. The absorption in case of x = 0.01, 0.05 and 0.1 Ni concentration has been at 320 nm, 316 nm and 311 nm corresponding to the band gaps of 3.87 eV, 3.93 eV and 3.98 eV, respectively. The blue shift in Ni-doped nanorods may be ascribed to the lower ionic radius of Ni ions as compared to the replaced Zn ions in host ZnS, as we assume that Ni ions, having smaller ionic radii, have replaced the Zn ions, leading to smaller size of doped ZnS or it may be associated with creation of energy levels within the ZnS band gap. Sambasivam et al. in case of Fe-doped ZnS nanoparticles and Feng et al. in Fe-doped ZnS thin films have reported similar observations [74, 188]. Increase in band gap with the Ni doping, again supports the substitution of Ni ions in the ZnS lattice [186]. The blue-shift may also be associated with the strain induced in ZnS lattice due to doping.

**3.2.1.4.2 PL studies**

The PL emission spectra, recorded between 325-550 nm, obtained at excitation wavelength of 300 nm ($\lambda_{ex.}$= 300 nm), are shown in Figure 3.30. The spectra depict two main peaks, at 340 nm and 435 nm, in undoped and Ni-doped ZnS nanorods. The peak at 340 nm may be attributed to wide band edge emission and blue emission at 435 nm may be attributed to self activated luminescence and recombination of carriers between sulphur vacancies related donor and valence bands [186]. The blue emission band in Ni-doped ZnS nanorods may also be attributed to the transition from the conduction band of ZnS to an intermediate state of Ni which lies between the conduction band and valence band of ZnS [189]. The PL intensity reduces in Ni-doped ZnS nanorods as compared to undoped counterpart.

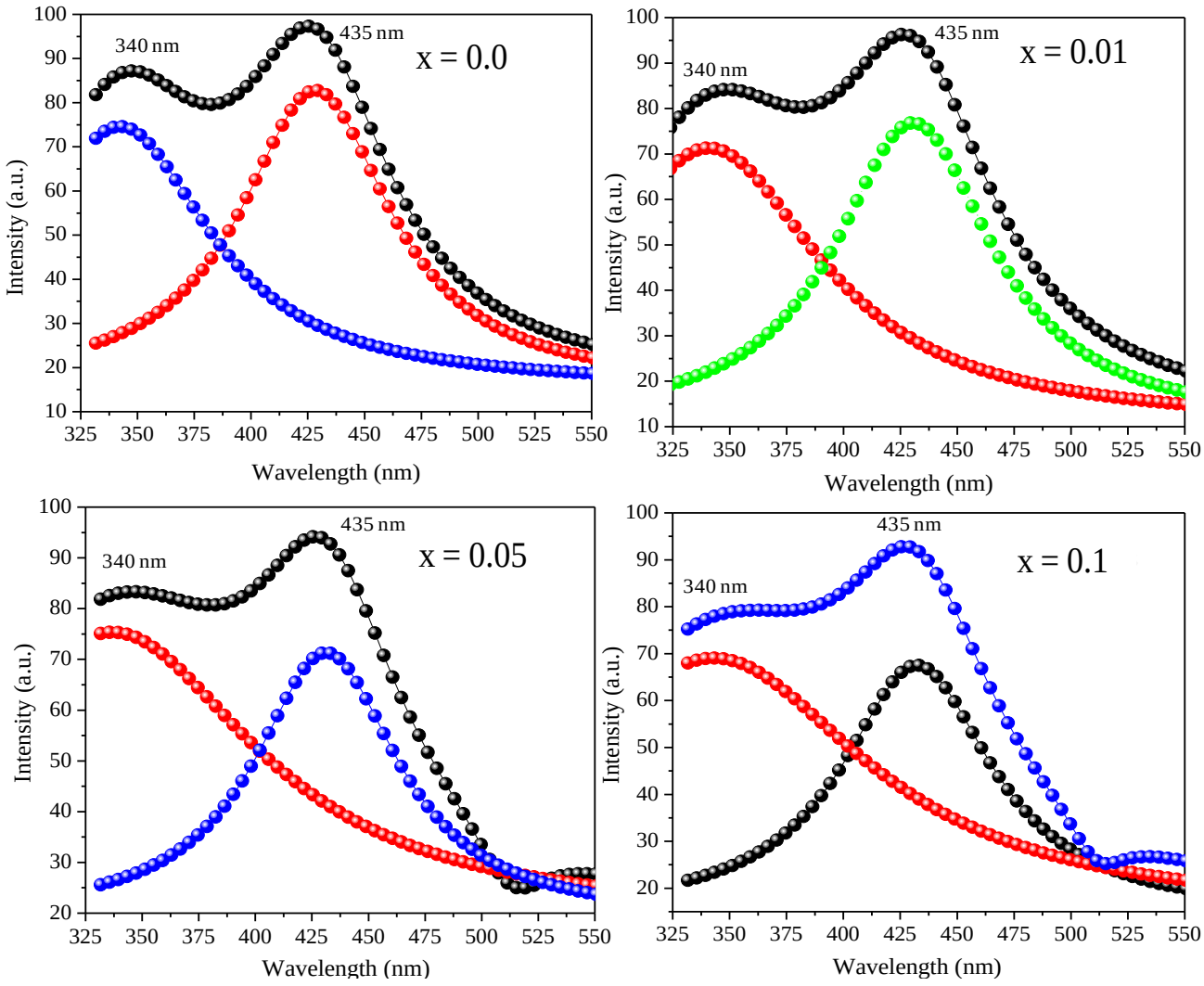


**Figure 3.30** PL spectra of $Zn_{1-x}Ni_xS$ (x = 0.00, 0.01, 0.05 and 0.10) nanorods

The PL intensity registers a quenching with increased Ni concentrations from x = 0.00 to 0.1. Observations of photoluminescence intensity quenching have been reported in the literature in case of doped ZnS nanostructures. It may be attributed to the fact that doped transition metals act as electron trapping centers, resulting into non-radiative recombination. Hence, as the concentration of transition metal is increased the electron trapping centers also increase, resulting in non-radiative recombination, leading to subsequent quenching in PL intensity [190, 191].

### 3.2.1.5 Magnetic studies

Magnetic properties of $Zn_{1-x}Ni_xS$ (x = 0.00, 0.01, 0.05 and 0.10) nanorods have been studied using

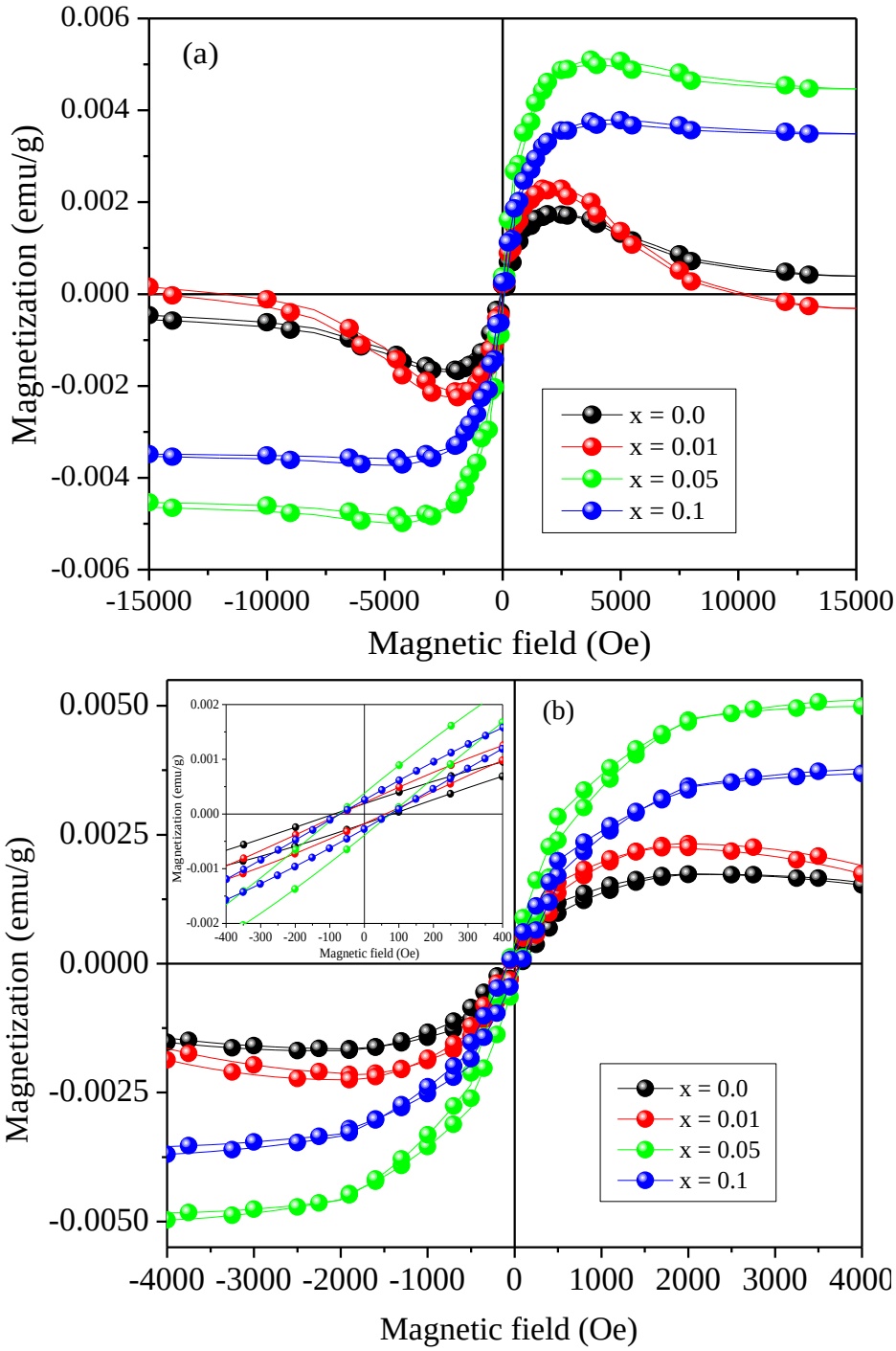


**Figure 3.31** M-H curves of $Zn_{1-x}Ni_xS$ (x = 0.00, 0.01, 0.05 and 0.10) nanorods (a) up to 1.5 T and (b) up to 4000 Oe [Inset: magnified view of M-H curves]

VSM. The M-H curves obtained at room temperature are shown in Figure 3.31 (a, b). It has been observed that in addition to Ni-doped ZnS nanorods, the undoped ZnS nanorods also exhibit ferromagnetic like behaviour. As the Ni concentration increase, the magnetization registers an increase indicating that magnetism caused is due to Ni in ZnS matrix. The ferromagnetic character in undoped ZnS nanorods may be ascribed to the Zn vacancies [192]. The enhanced ferromagnetic character may be ascribed to the substitution of Ni in ZnS lattice, but not due to Ni clusters or other compounds e.g. NiS, as in XRD spectra, no such secondary phases have been observed. The observed values of retentivity for x = 0.01, 0.05 and 0.1 concentrations are 0.00025 emu/g, 0.0005 emu/g and 0.0004 emu/g respectively and that of coercivity are 80.0 Oe, 105.0 Oe and 85.0 Oe respectively. Increase in Ni-doping concentration up to x = 0.05, increases the magnetization with increased magnetic field. The induced magnetism with high carrier concentration may be ascribed to the hybridization between the transition metal atoms and S atoms of ZnS lattice [193]. The ferromagnetism may be ascribed to exchange interactions between the dopant atoms [78, 194]. However, the saturation magnetization reduces as Ni-doping concentration is increased to x = 0.10. Variation of magnetization with doping concentration has been illustrated in Figure 3.32. Sambasivam et al. also observed similar trend in Fe-doped ZnS nanoparticles. It has been observed that with increase in Fe-doping concentration, the magnetization reduces at higher concentrations [74]. Decrease in magnetization at x = 0.10 Ni-doping concentration may be attributed to more grain boundaries [195]. The probability of inducing grain boundaries are high at increased doping of external agents i.e. Ni. In literature, decrease in magnetization at higher concentration has been associated with the super-exchange interaction caused due to increase in nearest neighbour antiferromagnetic coupling of Ni ion pairs in doped ZnS nanorods [175].

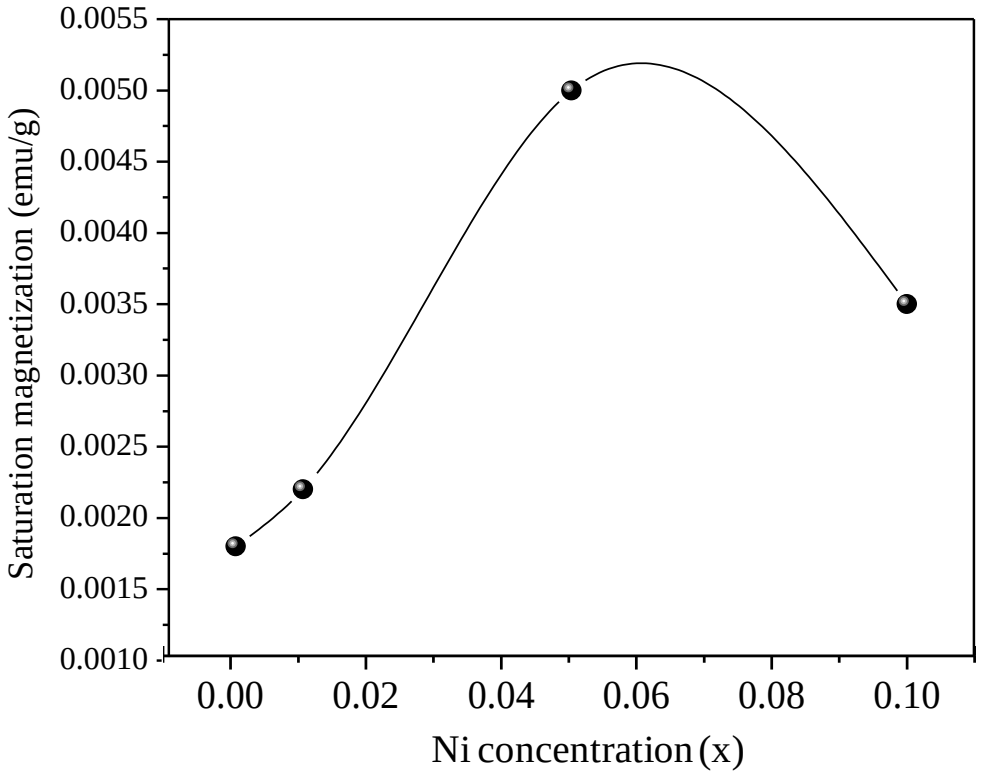


**Figure 3.32** Variation of saturation magnetization with Ni-doping concentration

The antiferromagnetic coupling is enhanced at higher concentrations due to increased number of doped Ni ions, leading to suppression in magnetization.

### 3.2.2 Fe-doped ZnS Nanorods

This section deals with the morphology, structure, optical and magnetic analysis of $Zn_{1-x}Fe_xS$ (x = 0.00, 0.01, 0.05 and 0.10) nanorods. The properties of $Zn_{1-x}Ni_xS$ (x = 0.00, 0.01, 0.05 and 0.10) nanorods have been analyzed using TEM, HRTEM, EDS, XRD, UV-Vis., PL and VSM techniques.

#### 3.2.2.1 Morphology and elemental studies

The morphology of $Zn_{1-x}Fe_xS$ (x = 0.00 and 0.10) nanorods have been studied using TEM and HRTEM images. The images obtained are shown in Figure 3.33. It is clear that Fe-doped ZnS nanorods (x = 0.10) have identical morphology when compared with undoped counterparts (x =

0.00). The average diameter of nanorods has been found to be ~10 nm and length varying between 50-400 nm.

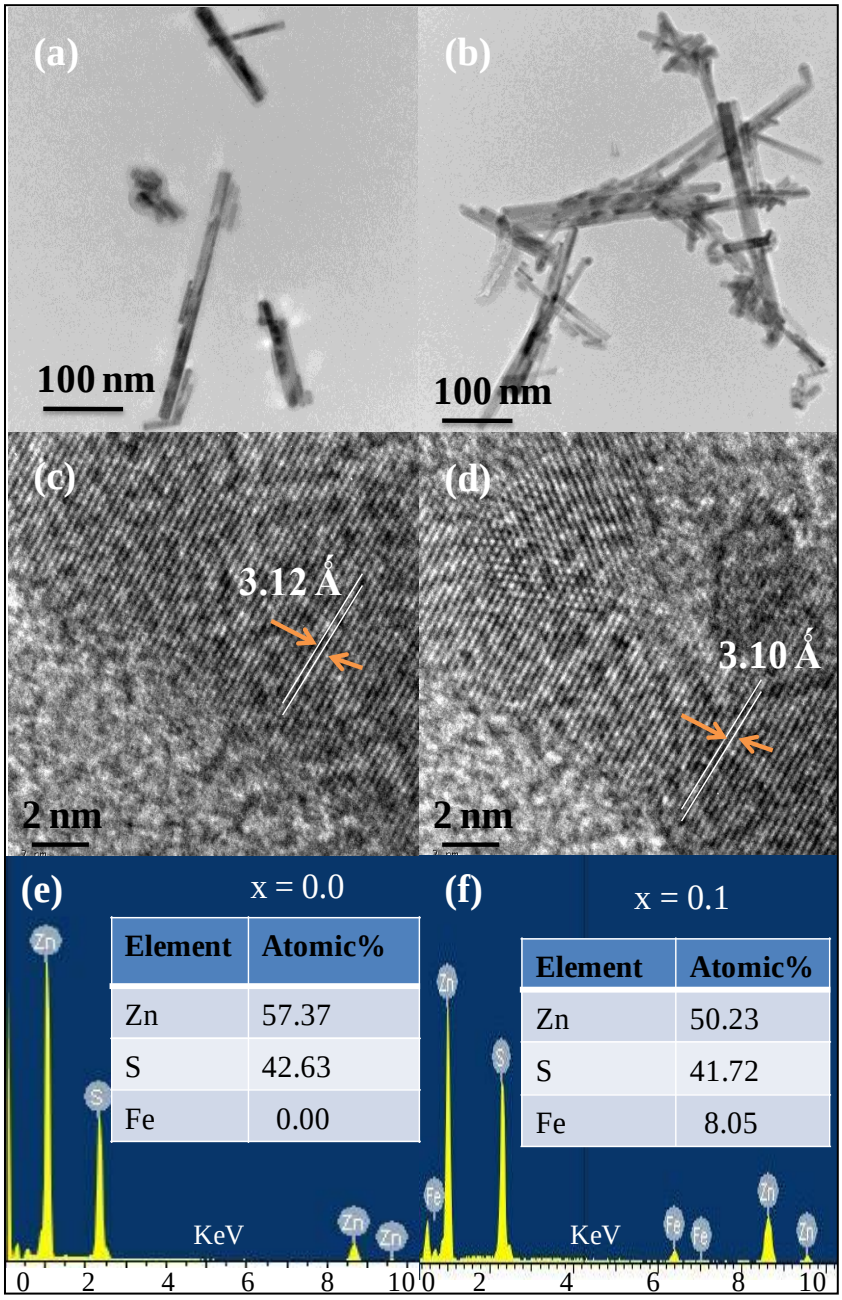


**Figure 3.33** TEM images of $Zn_{1-x}Fe_xS$ nanorods (a) x = 0.00 and (b) x = 0.10; HRTEM images (c) x = 0.00 and (d) x = 0.10; EDS spectra (e) x = 0.00 and (f) x = 0.10

The HRTEM images, Figure 3.33(c, d), indicate sharp lattice fringes with atomic spacing of 3.12 Å and 3.10 Å for x = 0.00 and 0.1, respectively. These values match with (002) plane of standard

ZnS (JCPDS card no. 36-1450). Clearly, the atomic spacing of Fe-doped ZnS nanorods is slightly less as compared to the undoped counterpart. The observed atomic spacing values, of undoped and doped ZnS nanorods, accord well with d-spacing values of (002) plane as obtained from XRD spectra and decrement may be caused due to the strain induced in ZnS lattice [196]. To confirm the presence of Fe in ZnS samples, the elemental analysis has been made on the basis of EDS spectra. The EDS spectra for $Zn_{1-x}Fe_xS$ (x = 0.00 and 0.10) nanorods are indicated in Figure 3.33 (e, f). The detailed elemental analysis of $Zn_{1-x}Fe_xS$ (x = 0.00, 0.01, 0.05 and 0.10) nanorods is shown in Table 3.9.

**Table 3.9** Elemental composition of $Zn_{1-x}Fe_xS$ (x = 0.00, 0.01, 0.05, and 0.10) nanorods

| Fe concentration (x) | Atomic% |
|---|---|
| 0.00 | Zn = 57.37, S = 42.63, Fe = 0.00 |
| 0.01 | Zn = 56.72, S = 42.44 , Fe = 0.84 |
| 0.05 | Zn = 54.24, S = 41.81, Fe = 3.95 |
| 0.10 | Zn = 50.23, S = 41.72 , Fe = 8.05 |

The undoped ZnS samples indicate the presence of Zn and S atoms; whereas, the doped ZnS samples indicate the presence of Fe; however, the observed Fe amount is lower than the actual doped amount, which may be associated with the removal of Fe during the extensive washing of the ZnS samples [196].

### 3.2.2.2 Structural studies

The structural properties have been analyzed using XRD patterns. The XRD patterns of $Zn_{1-x}Fe_xS$ (x = 0.00, 0.01, 0.05 and 0.10) nanorods are shown in Figure 3.34. The diffraction peaks have been observed at $2\theta$ = 26.5°, 28.8°, 30.5°, 39.8°, 47.6°, 51.8° and 56.5° corresponding to the peaks (100), (002), (101), (102), (110), (103), and (112) respectively. These peaks can be indexed to wurtzite phase (JCPDS card no. 36-1450).

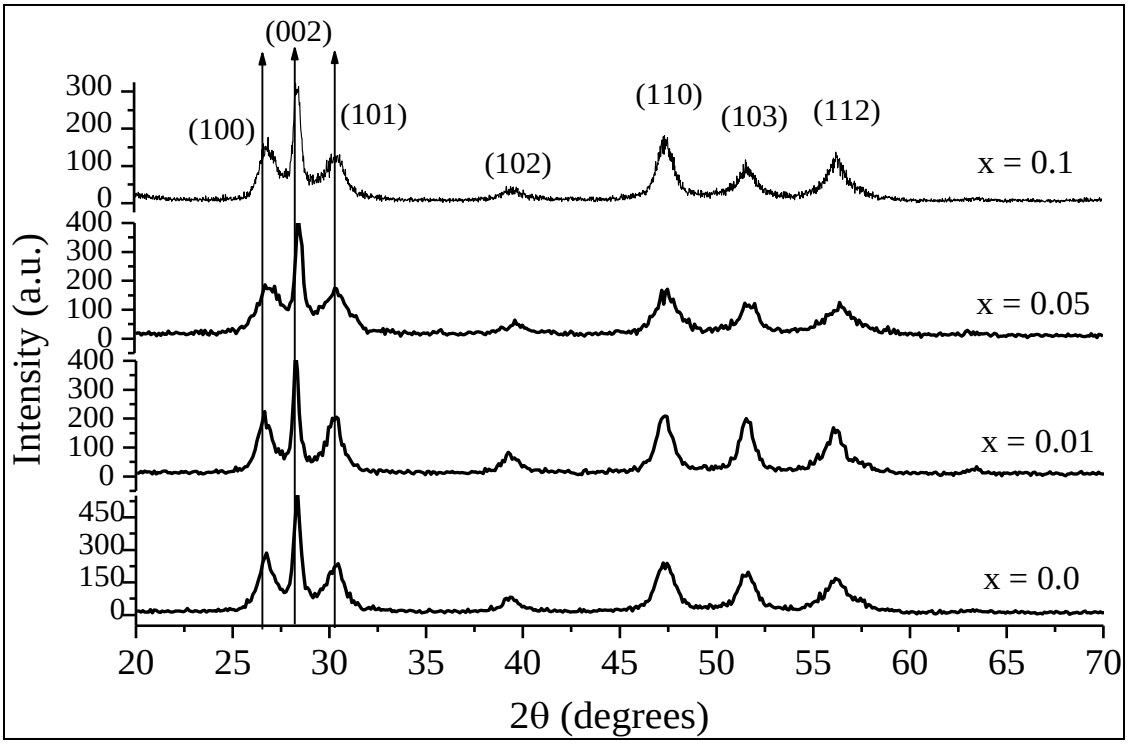


**Figure 3.34** XRD patterns of $Zn_{1-x}Fe_xS$ (x = 0.00, 0.01, 0.05 and 0.10) nanorods

No extra peaks of secondary phases have been observed in case of Fe-doped samples, which supports that Fe has been substituted in the ZnS lattice. Clearly, there is a slight shift in the peak position towards a higher diffraction angles as the concentration is increased, which may be ascribed to smaller ionic radius of $Fe^{2+}$ as compared to $Zn^{2+}$. The preferred orientation of a particular crystal plane has been determined by texture coefficient [187]. It has been observed that the value of *TC(002)* is maximum, indicating *(002)* plane as preferred direction of growth. W-H plots for undoped and Fe-doped ZnS nanorods have been shown in Figure 3.35. Plots again indicate negative slopes in all samples which again show that in case of Fe-doped ZnS nanorods the lattice is under compressive strain.

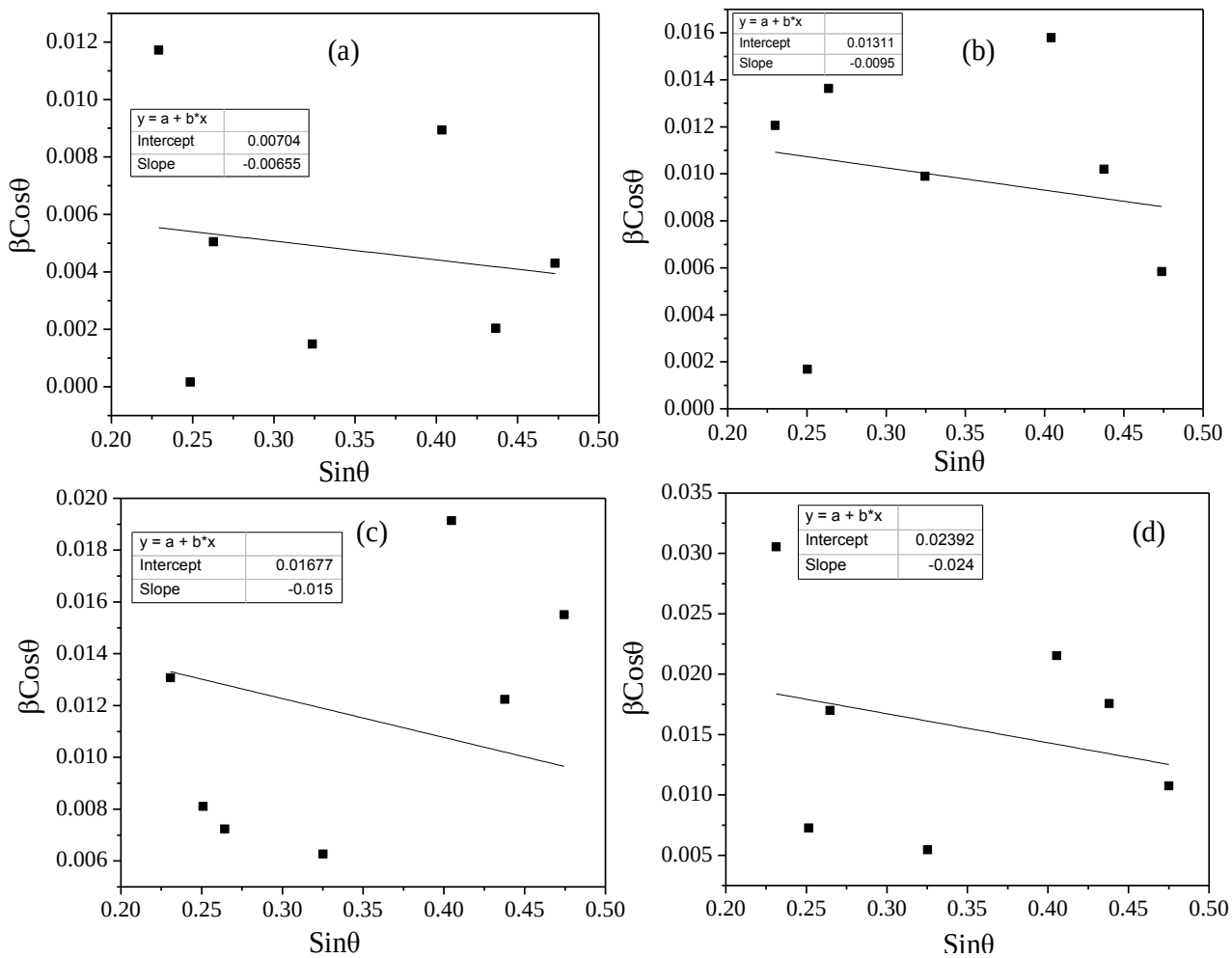


**Figure 3.35** W-H plots of $Zn_{1-x}Fe_xS$ nanorods at (a) x = 0.00 (b) x = 0.01, (c) x = 0.05, and (d) x = 0.10

The lattice parameters, crystallite sizes and strain induced are presented in Table 3.10.

**Table 3.10** Structural parameters of $Zn_{1-x}Fe_xS$ nanorods (*indicated few 2θ positions)

| Fe doping (x) | 2θ* | | | Lattice constant (Å) | d-spacing (Å) | Crystallite size (nm) | | Strain |
|---|---|---|---|---|---|---|---|---|
| | (002) | (110) | (112) | | | Scherrer's equation | W-H plot | |
| 0.00 | 28.34 | 47.21 | 56.14 | a = 3.86, c = 6.30 | 3.15 | 10.57 | 10.11 | -0.0012 |
| 0.01 | 28.41 | 47.34 | 56.21 | a = 3.83, c = 6.29 | 3.13 | 10.22 | 9.65 | -0.0023 |
| 0.05 | 28.48 | 47.45 | 56.33 | a = 3.82, c = 6.27 | 3.10 | 9.54 | 8.76 | -0.0037 |
| 0.10 | 28.61 | 47.60 | 56.45 | a = 3.81, c = 6.23 | 3.09 | 8.32 | 7.41 | -0.0060 |

It has been observed that as the Fe concentration is increased, the lattice parameters are slightly decreased, which indicates that the Fe-doped ZnS structure is under compressive strain due to different ionic radii of Fe ions as compared to replaced Zn ions. The *d*-spacing values decrease with increased Fe concentrations. These results accord well with HRTEM observations [196]. The strain induced increases as the Fe concentration is increased.

### 3.2.2.3 Optical studies

Optical properties of $Zn_{1-x}Fe_xS$ (x = 0.00, 0.01, 0.05 and 0.10) nanorods comprise UV-Vis. and PL studies. The detailed discussions of UV-Vis. and PL studies are given below:

#### 3.2.2.3.1 UV-Vis. studies

The absorption spectra of $Zn_{1-x}Fe_xS$ (x = 0.00, 0.01, 0.05 and 0.10) nanorods, recorded in 250-400 nm range, have been shown in Figure 3.36.

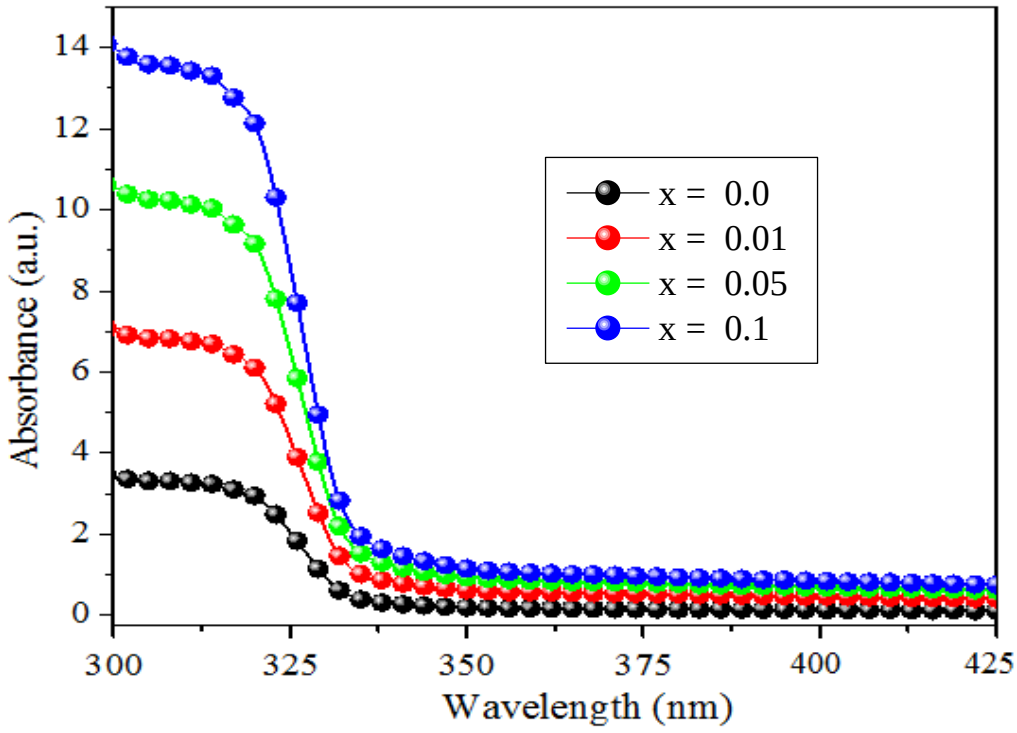


**Figure 3.36** UV-Vis. spectra of $Zn_{1-x}Fe_xS$ (x = 0.00, 0.01, 0.05, and 0.10) nanorods

It is clear that maximum absorbance wavelength ($\lambda_{max}$) appears at 320 nm, 318 nm, 315 nm and 310 nm for x = 0.000, 0.01, 0.05, and 0.10 Fe concentration, respectively, indicating a blue-shift as compared to the bulk counterpart. The blue-shift continues as the dopant concentration is increased from x = 0.00 to 0.1. Blue-shift in undoped nanorods as compared to bulk ZnS may be ascribed to quantum confinement effects [166], whereas, the blue shift in absorption edge of Fe-doped ZnS nanorods may be attributed to the smaller radii of Fe ions as compared to the replaced Zn ions in ZnS lattice. Similar observations have been reported in literature in Fe-doped ZnS thin films and nanorods [74, 188, 196]. The blue shifting of absorption edge with Fe concentration has been summarized in Table 3.11.

**Table 3.11** Variation of band gap with Fe concentration (x)

| **Fe concentration (x)** | $\lambda_{max}$ **(nm)** | **Band gap (eV)** |
|---|---|---|
| 0.00 | 320 | 3.87 |
| 0.01 | 318 | 3.89 |
| 0.05 | 315 | 3.93 |
| 0.10 | 310 | 4.00 |

In literature, the cause of blue-shifting in band gap with external doping has also been associated with the formation of new energy levels by the dopant ions in the host semiconductor [174]. The blue-shift may also be associated with the strain induced in ZnS lattice due to doping.

**3.2.2.3.2 PL studies**

The PL emission spectra, obtained at excitation wavelength $\lambda_{ex.}$ = 300 nm, are shown in Figure 3.37. The two wide peaks at 447 nm and 533 nm have been obtained, indicating the blue and green emission respectively. The blue emission peak at 447 nm may ascribe to radiative recombination between sulphur vacancies related donor energy levels and purity phase of host ZnS material [196].

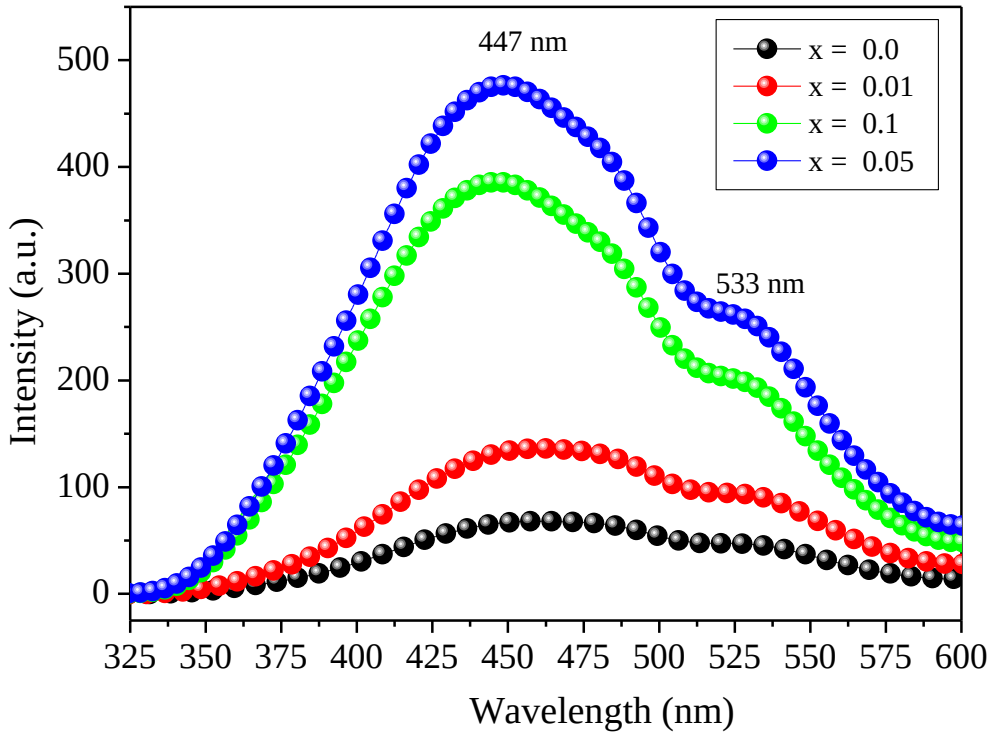


**Figure 3.37** PL spectra of $Zn_{1-x}Fe_xS$ (x = 0.00, 0.01, 0.05, and 0.10) nanorods

Green emission peak at 533 nm may be associated to defects e.g. sulphur or zinc vacancies [100]. The PL intensity increases with increased Fe concentration up to 0.05. As the Fe concentration is increased further up to x = 0.10, quenching in PL intensity is observed. The higher PL intensity at lower doping concentration may be associated to the fact that at lower concentration (x = 0.00, 0.01 and 0.05) dopant may find a vacancy at interstitial sites or at the lattice position, leading to the creation of new radiation centers, resulting an increase in PL intensity [169, 186]. As the Fe concentration is increased further up to x = 0.10, the doped Fe ions interfere with the radiative recombination which overshadows the effect of creating new radiation centers, hence resulting in the quenching of fluorescence intensity at higher doping concentrations. Similar observations have been reported earlier in the literature with Ni-doping in ZnS nanorods [54, 186].

### 3.2.2.4 Magnetic studies

The M-H curves obtained up to 2 T, at room temperature, are shown in Figure 3.38. The curves indicate that undoped (x = 0.00) ZnS nanorods exhibit a diamagnetic character, whereas, the Fe-doped ZnS (x = 0.01, 0.05 and 0.1) nanorods exhibit ferromagnetic character up to 5000 Oe. As the magnetic field is increased further up to 2 T, there is a sharp decrease in the magnetization and diamagnetic character appears to be induced. M-H curves exhibit remanent magnetization of 0.00034 emu/g, 0.0013 emu/g, 0.002 emu/g and 0.0016 emu/g for x = 0.00, 0.01, 0.05 and 0.10 Fe concentrations with corresponding saturation magnetization of 0.0025 emu/g, 0.0065 emu/g, 0.012 emu/g and 0.0095 emu/g, respectively. The small coercivity in all samples indicates the soft magnetic behaviour. The M-H curves indicate that ferromagnetism becomes more prominent as the Fe concentration is increased up to x = 0.05. This behaviour clearly indicates that insertion of Fe ions in ZnS matrix induces a ferromagnetic character in the doped ZnS nanorods [196]. The ferromagnetic behaviour may be thought of due to the aggregated Fe atoms in the ZnS lattice, but this possibility can be ruled out as no secondary phases have been observed in XRD spectra. As the Fe-doping concentration is increased further to x = 0.10, the saturation magnetization is found reduced. The ferromagnetism at lower concentration may be ascribed to the intrinsic coupling between the doped Fe-Fe atoms [183]. As the concentration is further increased to x = 0.10, the Fe-Fe distance in the ZnS matrix is reduced, leading to antiferromagnetic interaction, which may cause a decrease in the magnetization. Similar observations have been reported in literature in case of Ni-doped and Co-doped ZnS nanoparticles. It has been stated that reduced magnetization arises due to the competition between antiferromagnetic and ferromagnetic ordering [76, 166].

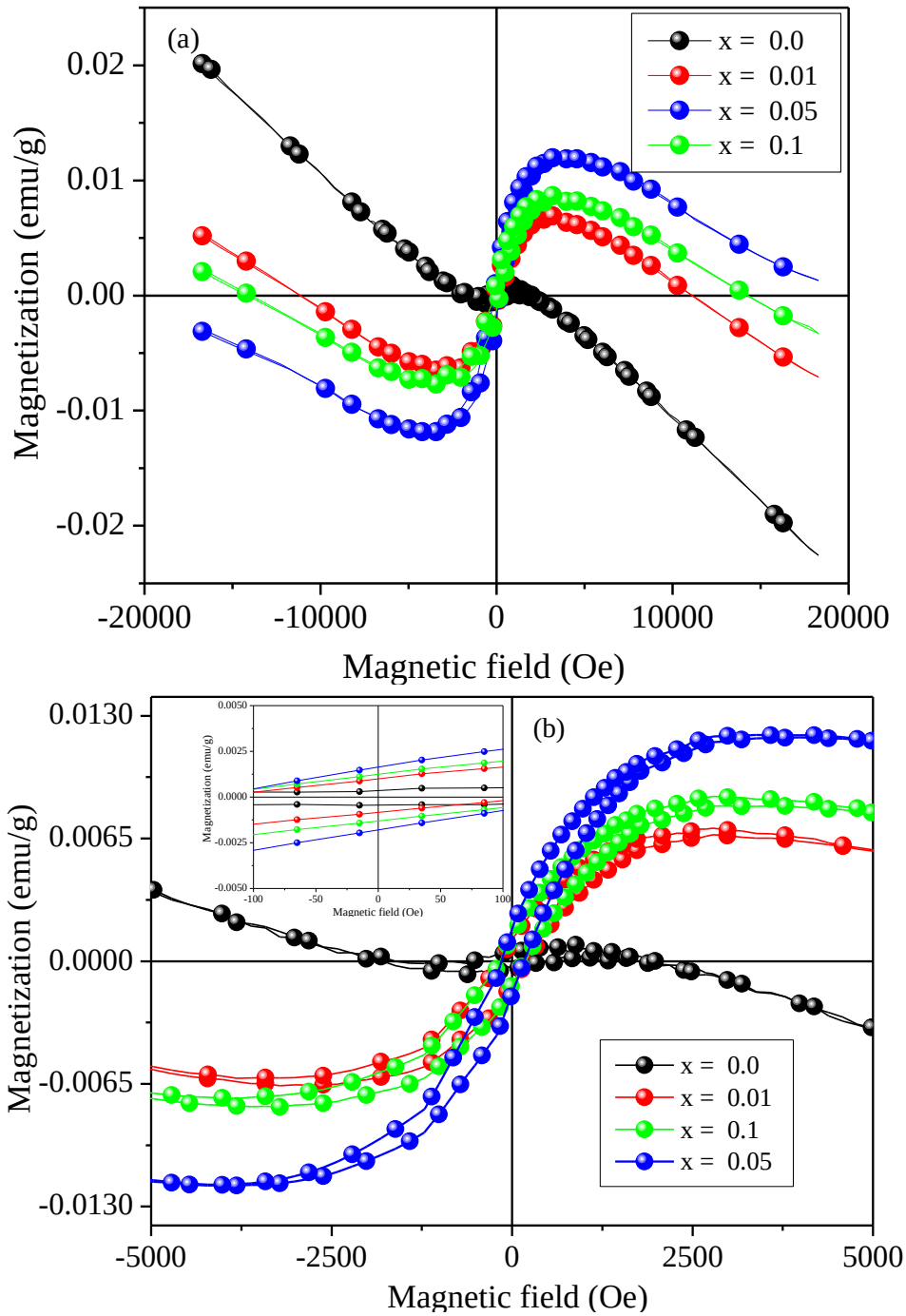


**Figure 3.38** M-H curves of $Zn_{1-x}Fe_xS$ (x = 0.00, 0.01, 0.05 and 0.10) nanorods (a) up to 2 T and (b) up to 5000 Oe range [inset: magnified view of M-H curves].

### 3.2.3 Co-doped ZnS nanorods

In this section, morphological, structural, optical and magnetic properties of $Zn_{1-x}Co_xS$ (x = 0.00, 0.01, 0.05 and 0.10) nanorods have been discussed. The investigations of different properties have been made for Co-doping concentrations, x = 0.00, 0.01, 0.05 and 0.10 respectively.

#### 3.2.3.1 Morphological studies

The morphology of the $Zn_{1-x}Co_xS$ (x = 0.00, 0.01, 0.05 and 0.10) nanorods has been analyzed using TEM. TEM images for $Zn_{1-x}Co_xS$ (x = 0.00 and 0.10) nanorods are shown in Figure 3.39 (a, b). TEM images indicate 1-D cylindrical nanorods with varied length raging between 50-250 nm and diameter ~10 nm. It has been observed that $Zn_{1-x}Co_xS$ (x = 0.00 and 0.10) nanorods have similar cylindrical morphology. HRTEM images as shown in Figure 3.39 (c, d), $Zn_{1-x}Co_xS$ (x = 0.00 and 0.10), exhibit the inter-atomic spacing values as 3.3 Å and 3.1 Å, respectively. The reduced inter-atomic spacing values have been confirmed in XRD studies [197]. EDS spectra have been recorded to identify the elements present in undoped and doped ZnS samples. EDS spectra, shown in Figure 3.39 (e, f), confirm the presence of Co in the doped ZnS nanorods samples. The atomic content of various elements in undoped and Co-doped ZnS nanorods have been tabulated in Table 3.12.

**Table 3.12** Elemental composition of $Zn_{1-x}Co_xS$ (x = 0.00, 0.01, 0.05, and 0.10) nanorods

| Co concentration (x) | Atomic% |
|---|---|
| 0.00 | Zn = 57.37, S = 42.63, Co = 0.00 |
| 0.01 | Zn = 57.08, S = 42.11 , Co = 0.81 |
| 0.05 | Zn = 54.17, S = 41.85, Co = 3.98 |
| 0.10 | Zn = 51.19, S = 41.40 , Co = 7.41 |

From Table 3.12, it is clear that the observed doped amount of Co is less as compared to actual doped concentration which may ascribe to the repeated washings with water and acetone which might have washed away the non-reacted Co content [197].

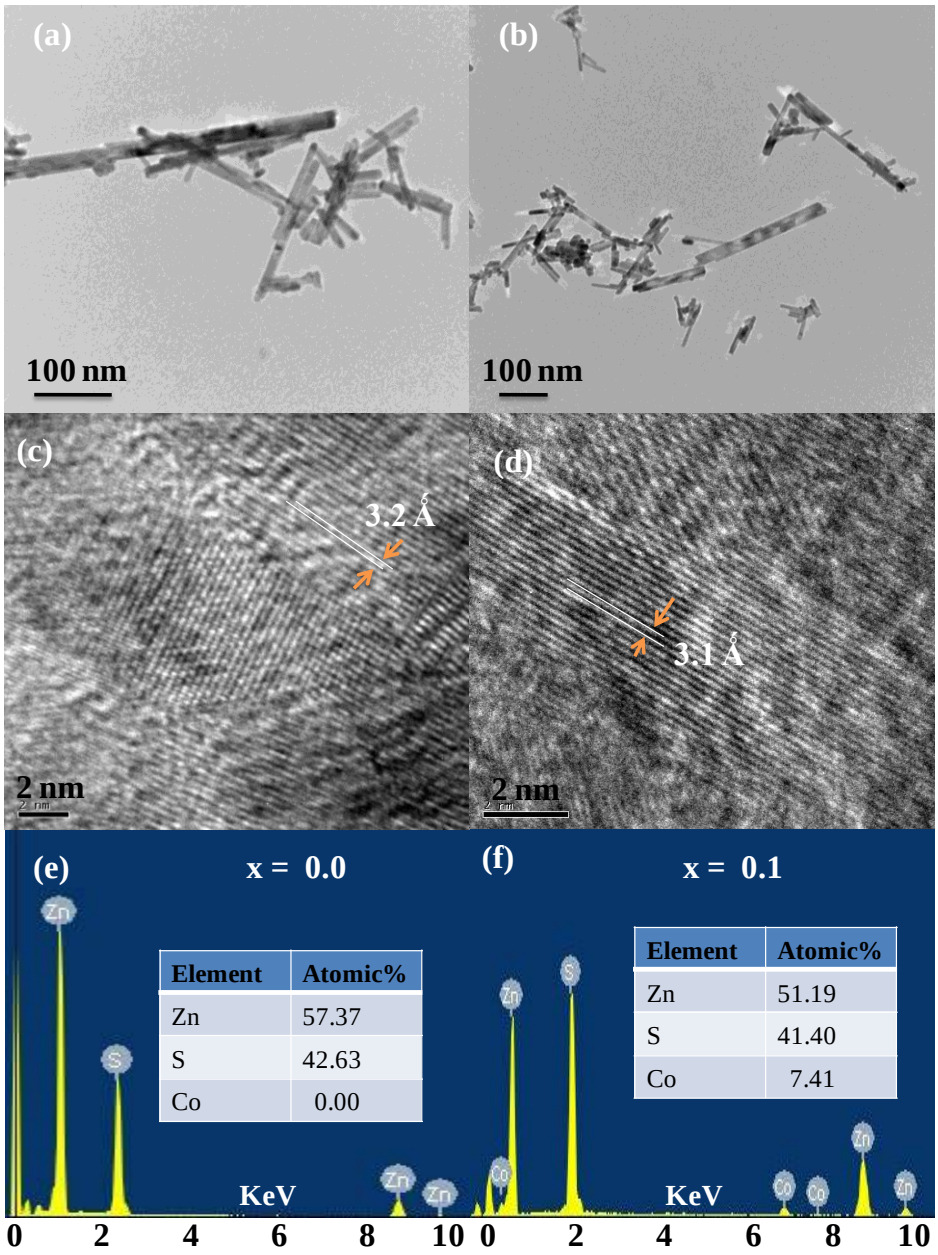


**Figure 3.39** TEM images of $Zn_{1-x}Co_xS$ (x = 0.00, 0.01, 0.05 and 0.10) nanorods at (a) x = 0.00 (b) x = 0.10; HRTEM images of (c) x = 0.00 (d) x = 0.10; EDS spectra of (e) x = 0.00 (f) x = 0.10

### 3.2.3.2 Structural studies

The structural properties of $Zn_{1-x}Co_xS$ (x = 0.00, 0.01, 0.05 and 0.10) nanorods have been analyzed using the XRD spectra. The XRD patterns of undoped and doped ZnS nanorods are shown in Figure 3.40. The diffraction peaks have been observed at 2θ = 26.5°, 28.8°, 30.54°,

39.77°, 47.6°, 51.83° and 56.45° corresponding to, respectively, the peaks (100), (002), (101), (102), (110), (103), and (112). These peaks can be indexed to wurtzite phase (JCPDS card no. 36-1450). No extra peaks of secondary phases have been observed in case of Co-doped samples, which supports that Co has been substituted in the ZnS host lattice. The preferred orientation of particular crystal planes has been observed by determining the texture coefficient, *TC(hkl)*.

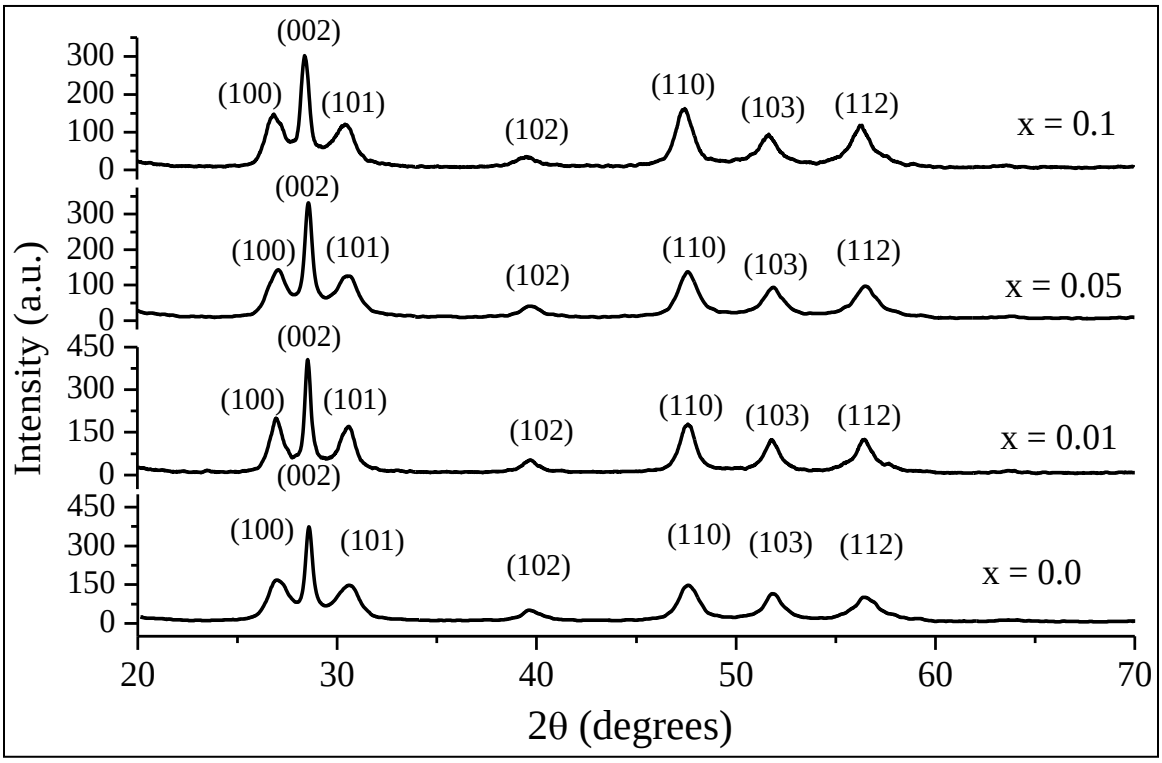


**Figure 3.40** XRD patterns of $Zn_{1-x}Co_xS$ (x = 0.00, 0.01, 0.05 and 0.10) nanorods

It is found that the value of '*TC(002)*' is maximum, indicating *(002)* plane as preferred direction of growth. W-H plots for undoped and Fe-doped ZnS nanorods have been shown in Figure 3.41. Plots again indicate negative slopes in doped ZnS nanorods which again show that in case of Co-doped ZnS nanorods the lattice is under compressive strain. The strain increases with doping concentration.

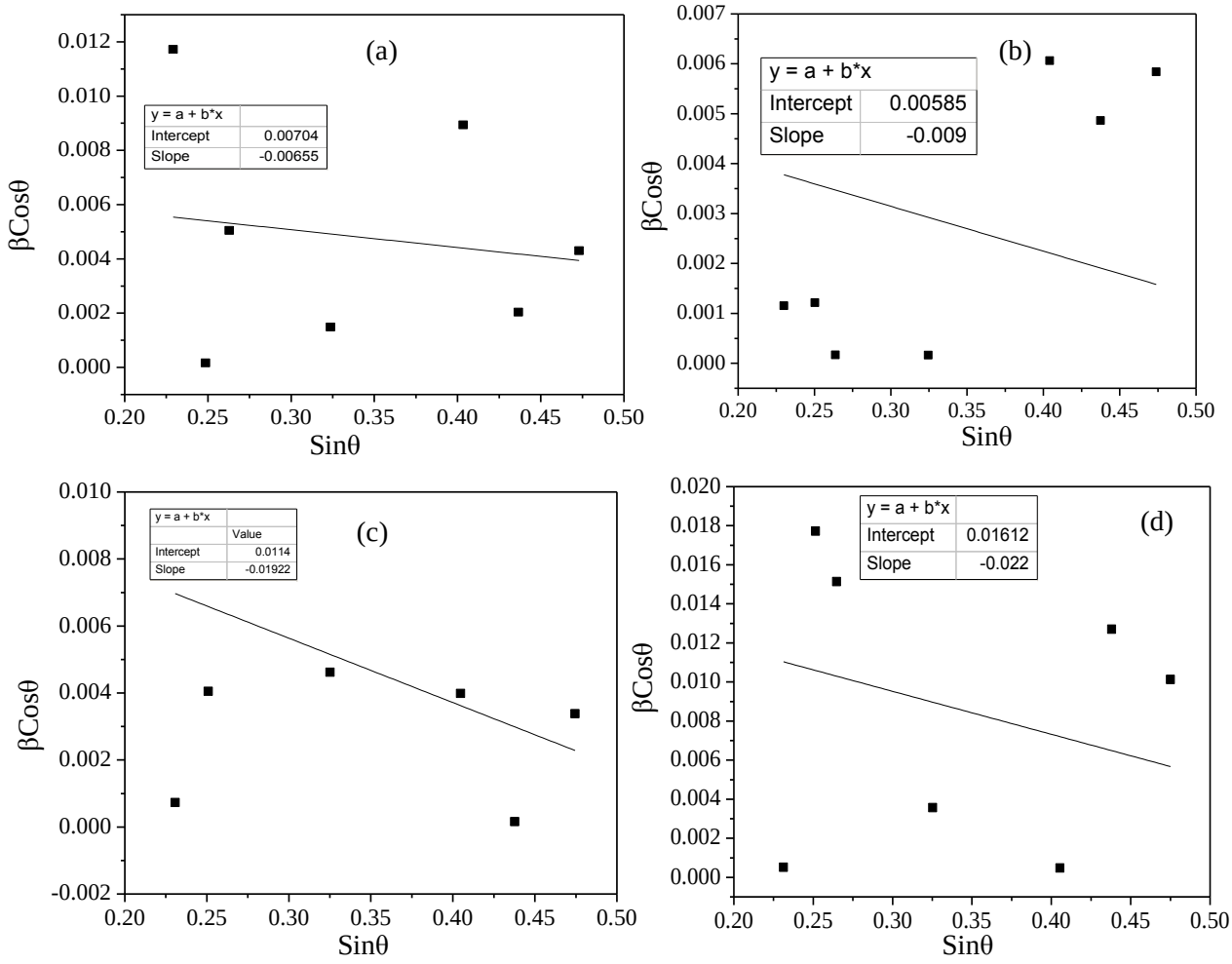


**Figure 3.41** W-H plots of $Zn_{1-x}Co_xS$ nanorods at (a) x = 0.00 (b) x = 0.01, (c) x = 0.05 and (d) x = 0.10

Lattice parameters including sizes and strain induced in lattice are shown in Table 3.13.

**Table 3.13** Structural parameters of $Zn_{1-x}Co_xS$ nanorods (*indicated few 2θ positions)

| Co doping (x) | 2θ* | | | Lattice constant (Å) | d-spacing (Å) | Crystallite size (nm) | | Strain (ε) |
|---|---|---|---|---|---|---|---|---|
| | (002) | (110) | (112) | | | Scherrer's equation | W-H plot | |
| 0.0 | 28.34 | 47.21 | 56.14 | a = 3.86, c = 6.30 | 3.15 | 10.57 | 10.11 | -0.0012 |
| 0.01 | 28.35 | 47.43 | 56.32 | a = 3.82, c = 6.22 | 3.12 | 14.24 | 13.70 | -0.0022 |
| 0.05 | 28.48 | 47.55 | 56.43 | a = 3.79, c = 6.17 | 3.09 | 13.14 | 12.16 | -0.0048 |
| 0.10 | 28.61 | 47.67 | 56.50 | a = 3.76, c = 6.12 | 3.08 | 11.02 | 9.61 | -0.0055 |

Table 3.13 indicate that there is a slight shift in the peak position towards a higher diffraction angle as the Co concentration is increased, supporting the doping of Co ions in ZnS lattice, may be ascribed to smaller ionic radius of $Co^{2+}$ as compared to $Zn^{2+}$. It has been observed that as the Co concentration is increased, the lattice parameters are found reduced, indicating that the Co-doped ZnS structure is under compressive strain due to the smaller ionic radii of Co ions as compared to the replaced Zn ions. The reduced d-spacing values corroborate with HRTEM analysis.

### 3.2.3.3 Optical studies

The optical studies have been analyzed on the basis of the spectra obtained using UV-Vis. and PL spectroscopy.

#### 3.2.3.3.1 UV-Vis. studies

UV-Vis. spectra of $Zn_{1-x}Co_xS$ (x = 0.00, 0.01, 0.05, and 0.10) nanorods have been shown in Figure 3.42.

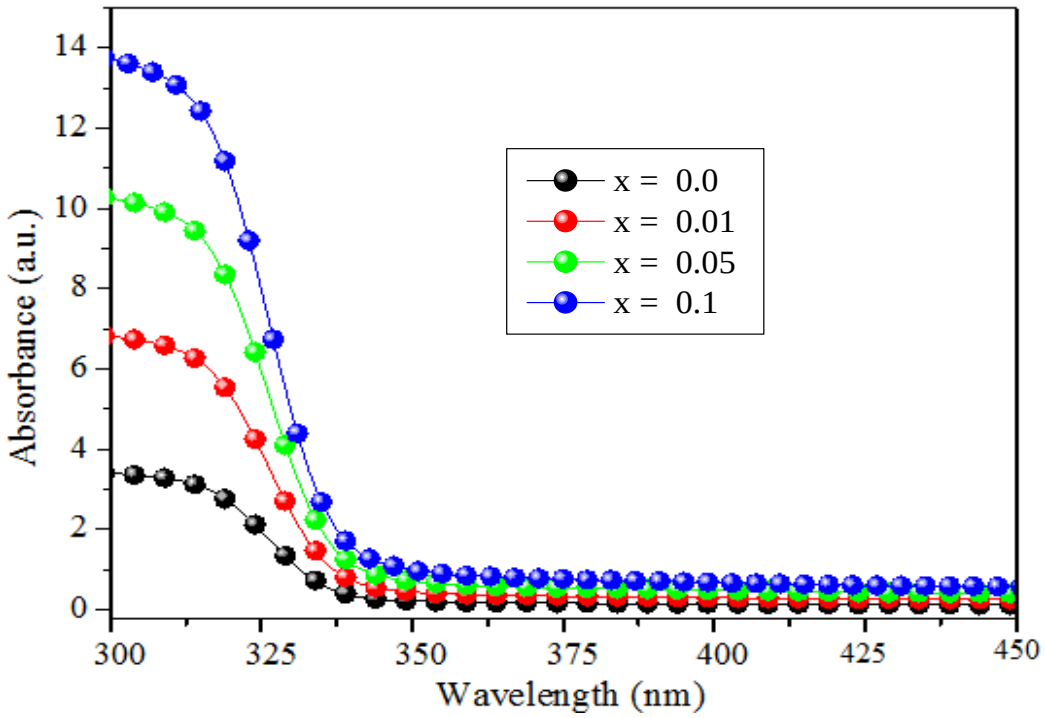


**Figure 3.42** UV-Vis. spectra of $Zn_{1-x}Co_xS$ (x = 0.00, 0.01, 0.05, and 0.10) nanorods

In case of $Zn_{1-x}Co_xS$ (x = 0.00) nanorods maximum absorbance has been observed has at 312 nm, corresponding to the band gap of 3.98 eV, blue shifted as compared to bulk counterpart [197]. This blue-shift in may be ascribed to quantum confinement effects [198]. As Co doping concentration is increased in ZnS matrix the maximum absorbance again found blue-shifted as compared to the undoped ZnS nanorods. The maximum absorbance in case of x = 0.10 Co concentration has been found to be 304 nm. The blue-shifting of absorption edge at different Co concentration has been summarized in Table 3.14.

**Table 3.14** Variation of band gap with Co concentration (x)

| Co concentration (x) | Absorption edge (nm) | Band gap (eV) |
|---|---|---|
| 0.00 | 312 | 3.98 |
| 0.01 | 310 | 4.00 |
| 0.05 | 308 | 4.03 |
| 0.10 | 305 | 4.07 |

The blue shift in absorption edge of Co-doped ZnS nanorods may ascribe to the smaller ionic radii of $Co^{2+}$ as compared to the replaced $Zn^{2+}$. As the Co concentration in ZnS matrix is increased the absorbance edge is further blue shifted as compared to the undoped ZnS nanorods which may be attributed to fact that the doped Co is forming new energy levels within the ZnS energy band [174, 197]. The blue-shift may also be associated with the strain induced in ZnS lattice due to doping.

**3.2.3.3.2 PL studies**

The PL emission spectra of $Zn_{1-x}Co_xS$ (x = 0.00, 0.01, 0.05, and 0.10) nanorods, obtained at excitation wavelength of 300 nm ($\lambda_{ex.}$ = 300 nm), are shown in Figure 3.43. The emission spectra exhibit two peaks, positioned at 422 nm and 485 nm. The 422 nm peak is analogous to the blue emission and 485 nm peak originates due to bluish-green emission. The blue emission peak at 422 nm may ascribe to radiative recombination between sulphur vacancies related donor

energy levels and purity of phase of host ZnS material, whereas, the peak at 485 nm may be attributed to surface zinc ions or associated defects [175].

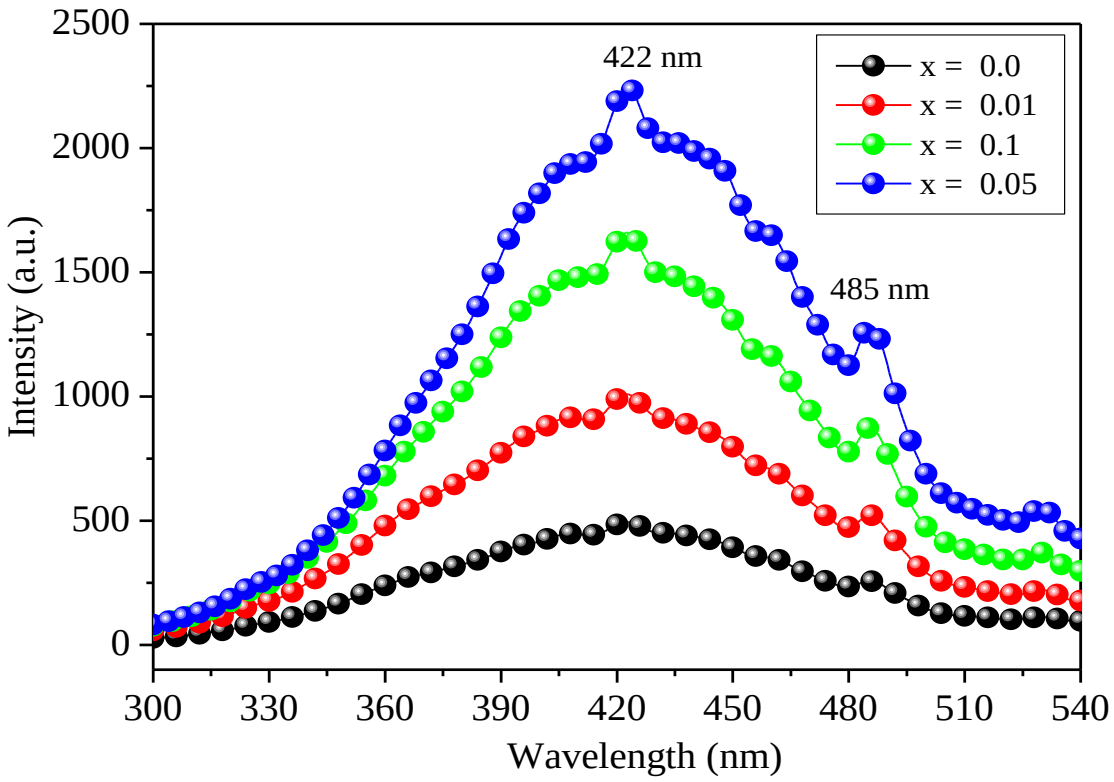


**Figure 3.43** PL spectra of $Zn_{1-x}Co_xS$ (x = 0.00, 0.01, 0.05 and 0.10) nanorods

The PL intensity increases as the Co concentration is increased up to x = 0.05. Further increase in Co concentration up to x = 0.10 leads to quenching in the PL intensity. The increase in PL intensity from x = 0.00 to 0.1 Co concentration may be attributed to the fact that at lower concentration the dopant may find a vacancy at interstitial sites or at the lattice position which may create new radiation centers, resulting in increased intensity [166, 169]. As the concentration is increased to x = 0.10, the doped Co ions interfere with the radiative recombination process, which diminishes the effect of creating new radiation centers, resulting in the quenching of fluorescence intensity at higher doping concentrations. The schematic energy level diagram of ZnS nanorods is illustrated in Figure 3.44.

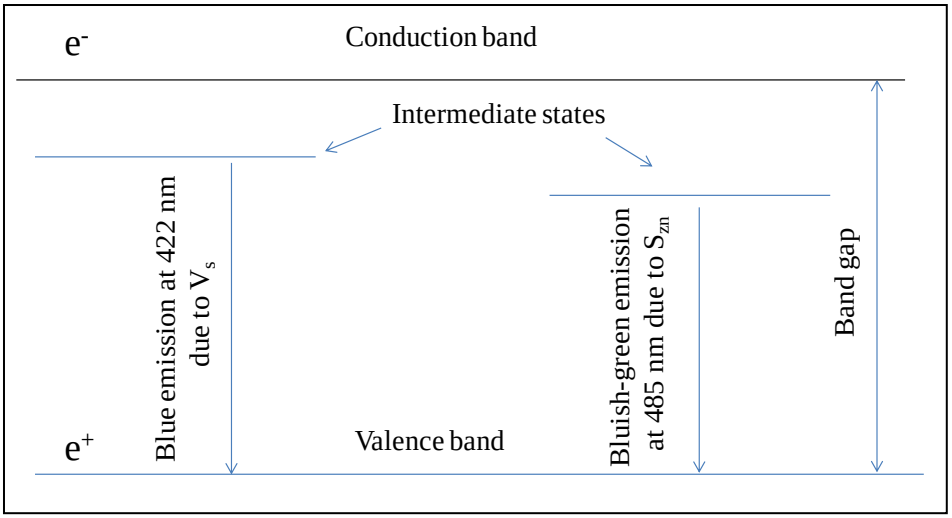


**Figure 3.44** Schematic energy level diagram indicating emission mechanism in doped ZnS nanorods: $V_s$ = sulphur vacancy, $S_{zn}$ = surface zinc ions

Similar behaviour has been observed in Ni-doped ZnS nanostructures [166]. It has been observed that PL intensity is increased at lower Ni concentrations, but, it is decreased at higher Ni concentrations [166, 170]. Some reports available in the literature have observed a sharp decrease in the PL intensity with the increased Co concentrations in ZnS lattice. It has been proposed that the Co atoms act as electron trapping centers that result in the non-radiative recombination [175].

**3.2.3.4 Magnetic studies**

The magnetic properties of $Zn_{1-x}Co_xS$ (x = 0.00, 0.01, 0.05 and 0.10) nanorods have been studied by analysing M-H curves obtained using VSM at room temperature (300 K) up to 1.75 T. The M-H curves of $Zn_{1-x}Co_xS$ (x = 0.00, 0.01, 0.05 and 0.10) nanorods are shown in Figure 3.39 (a, b). The magnetic profiles obtained indicate that undoped ZnS nanorods exhibit a diamagnetic character. Similar to bulk ZnS, the diamagnetic character in undoped ZnS nanorods have been observed [199, 200]. As the Co doping concentration in ZnS matrix is increased from x = 0.00 to 0.10, magnetic moment (emu/g) is increased with strong saturation magnetization.

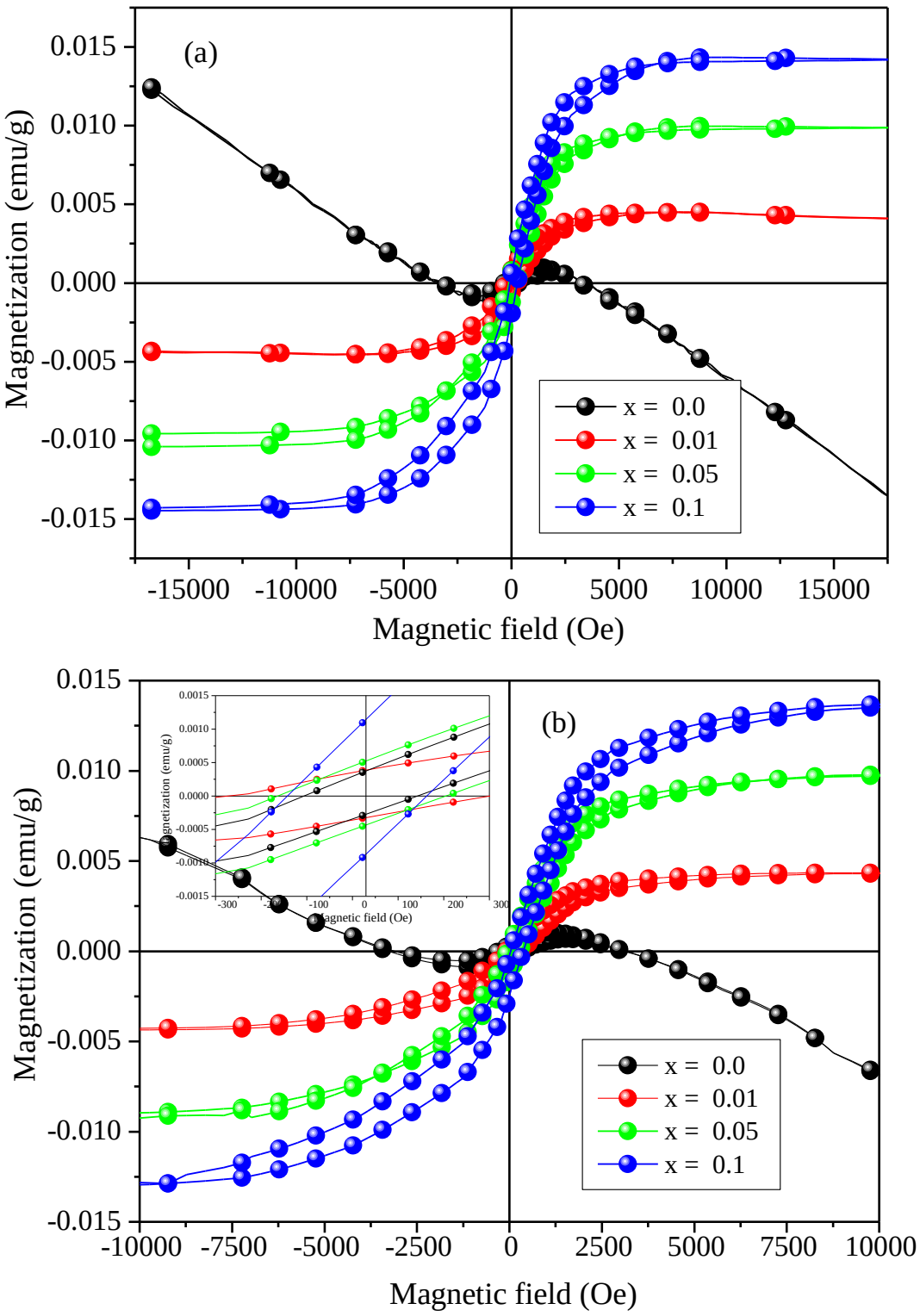


**Figure 3.45** M-H curves of $Zn_{1-x}Co_xS$ (x = 0.00, 0.01, 0.05 and 0.10) nanorods (a) up to 1.75 T and (b) up to 10000 Oe [inset: magnified view of M-H curves]

The curves indicate the remanent magnetization values of 0.0005 emu/g, 0.00077 emu/g, 0.0015 emu/g and 0.002 emu/g for x = 0.00, 0.01, 0.05 and 0.10 Co concentrations, respectively, and the corresponding coercivity values are- 380 Oe, 210 Oe, 155 Oe and 115 Oe, respectively. The reduced coercivity values again indicate soft magnetic nature of the Co-doped ZnS nanorods. Similar trend in coercivity values has been reported earlier in literature in case of Co-doped ZnS nanoparticles [76]. The strong ferromagnetic character in Co-doped ZnS nanorods may be ascribed to the exchange interaction between the localized '*d*' spins of the Co ions and free delocalized carriers which increases with increase in Co concentration [201]. The variation of coercivity and remanent magnetization with cobalt concentration has been illustrated in Figure 3.46. The saturation magnetization increases linearly as the Co concentration in ZnS lattice is increased.

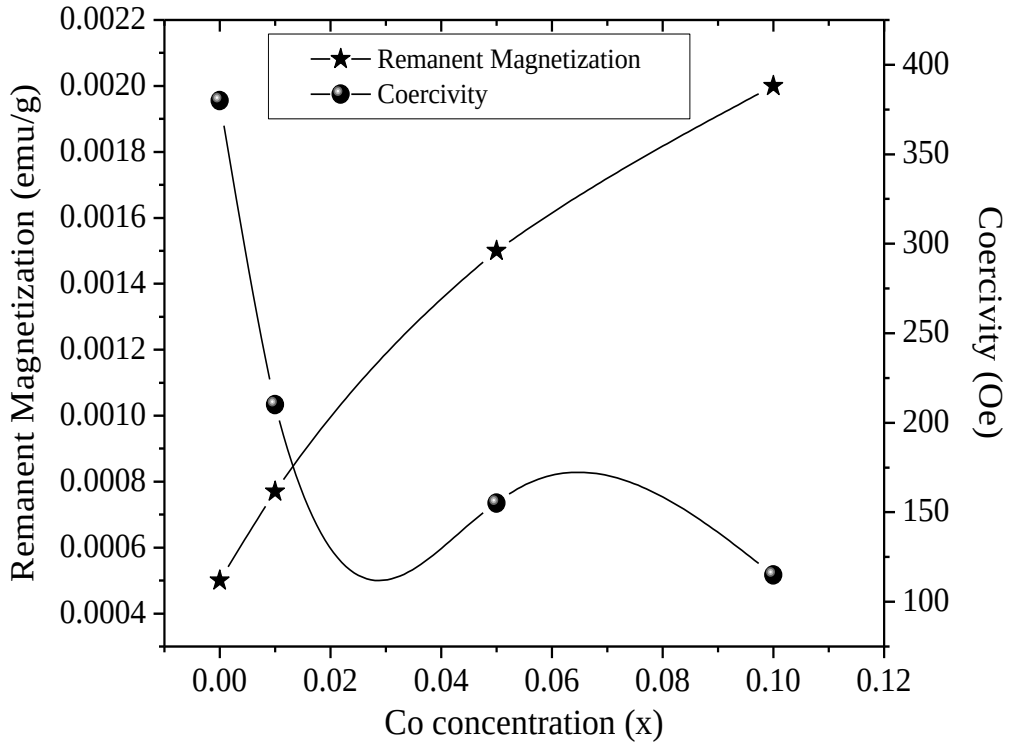


**Figure 3.46** Variation of remanent magnetization and coercivity with cobalt concentration

This behaviour indicates that insertion of Co ions in ZnS matrix induces a ferromagnetic character in the doped ZnS nanorods, which may be ascribed to the intrinsic coupling between the doped Co ions and not due to the clustered Co atoms in the ZnS lattice, as no secondary phases have been observed in XRD analysis [183, 197]. Ferromagnetic character has also been reported in the literature in Cr-doped ZnS nanoparticles, however, ferromagnetism has been found reduced with increased Cr concentrations. This behaviour has been ascribed to Cr-Cr interactions in ZnS nanoparticles [81, 201]. It is important to note in this case that the saturation is observed in Co-doped nanorods, but no such saturation is observed in Ni-doped or Fe-doped ZnS nanorods. Zhang et al. reported similar trend in Co-doped ZnO nanoparticles. It has been found that intrinsic ferromagnetism is observed when ZnO nanoparticles are doped with Co, however, no evidence of intrinsic ferromagnetism when doped with Fe [202].

To summarize, various properties of different transition metals-doped ZnS nanorods have been compared in Table 3.15.

**Table 3.15** Comparative chart of various properties of (Ni, Fe, Co)-doped ZnS nanorods

| **Sample** | **Ni-ZnS** | | | | **Fe-ZnS** | | | | **Co-ZnS** | | | |
|---|---|---|---|---|---|---|---|---|---|---|---|---|
| **Doping (x)** **Properties** | 0.00 | 0.01 | 0.05 | 0.10 | 0.00 | 0.01 | 0.05 | 0.10 | 0.00 | 0.01 | 0.05 | 0.10 |
| **Solvent** | EN+ de-ionized water | | | | EN+ de-ionized water | | | | EN+ de-ionized water | | | |
| **Size (nm)** | Diameter ~10 nm, length 50-300 nm | | | | Diameter ~10 nm, length 50-400 nm | | | | Diameter ~10 nm, length 50-400 nm | | | |
| **Doping (%) observed** | 0.0 | 0.71 | 3.89 | 7.88 | 0.0 | 0.84 | 3.95 | 8.05 | 0.0 | 0.81 | 3.98 | 7.41 |
| **Structure** | Hexagonal | | | | Hexagonal | | | | Hexagonal | | | |
| **Band gap (eV)** | 3.81 | 3.87 | 3.93 | 3.98 | 3.87 | 3.89 | 3.93 | 4.0 | 3.98 | 4.0 | 4.03 | 4.07 |
| **PL intensity (w.r.t. undoped)** | - | Decrease | Decrease | Decrease | - | Increase | Decrease | Decrease | - | Increase | Decrease | Decrease |
| **Magnetization (emu/g)** | 0.002 | 0.003 | 0.0055 | 0.0045 | 0.002 | 0.008 | 0.01 | 0.014 | 0.002 | 0.0045 | 0.012 | 0.015 |

# Chapter 4

# Conclusions

# Chapter 4

# Conclusions

*This chapter summarizes the present thesis work. The summary of main results, in case of nanoparticles as well as nanorods, has been presented along with the comparison of different properties of ZnS nanostructures at different dopant concentrations. The future scope of the present research work has also been envisioned.*

## 4.1 Conclusions

In the present thesis, transition metals (Ni, Fe and Co)-doped ZnS nanostructures have been studied in detail. The current work has been divided into two parts:

I. *Ni, Fe, and Co-doped ZnS nanoparticles*

II. *Ni, Fe, and Co-doped ZnS nanorods*

The main outcomes of the research work in each case, with different dopants, have been summarized below:

### 4.1.1 Ni-doped ZnS nanoparticles

- Ni-doped ZnS nanoparticles have been synthesized using reflux technique.
- Morphology wise undoped and Ni-doped ZnS nanoparticles, size ~5 nm, have been found identical as revealed from TEM images.
- The EDS spectra indicate the presence of Zn, S atoms in undoped samples, whereas doped samples indicate Zn, S and Ni atoms presence. The observed amount of dopant, Ni, is found less as compared to the actual doped Ni.

- The XRD spectra of undoped and Ni-doped ZnS nanoparticles indicate cubic structure of synthesized nanocrystals. The broadening of XRD peaks indicates the nanometer regime of the synthesized nanocrystals.
- XRD patterns of Ni-doped ZnS nanoparticles indicate no separate peaks of Ni impurity phase, which indicate that Ni has been inserted in the ZnS matrix.
- The reduction in lattice parameters in case of Ni-doped ZnS nanoparticles may be ascribed to compressive strain induced due to the replacement of Zn heavier ions with lighter Ni ions. W-H plots exhibit negative slope indicating that lattice is under compressive strain. The strain increases as the Ni-doping concentration is increased.
- The UV-Vis. spectra exhibited the absorption edge at 320 nm for undoped ZnS nanocrystals corresponding to a band gap of 3.87 eV, blue-shifted as compared to bulk ZnS due to quantum confinement effects. Blue-shift also observed as the dopant concentration is increased. For x = 0.10 Ni-doping the band gap found is 4.06.
- The blue-shift may also be associated with the strain induced in ZnS lattice due to doping.
- The PL spectra indicate two broad peaks centered at 360 nm and 435 nm.
- The PL intensity increases with x = 0.01 Ni doping, but as the Ni-doping concentration is increased to x = 0.05 and 0.1, the intensity is found to decrease.
- Undoped ZnS nanocrystals (x = 0.00) and x = 0.01 Ni concentration exhibit a weak ferromagnetic magnetic behaviour, whereas x = 0.05, and 0.10 Ni concentrations indicate highly ferromagnetic behaviour.

### 4.1.2 Fe-doped ZnS nanoparticles

- Undoped and Fe-doped ZnS nanoparticles have been synthesized using chemical synthesis route using ethanol as solvent.
- The TEM images indicate the average particle size as ~12 nm in case undoped and Fe-doped ZnS nanoparticles.
- EDS spectra revealed that the observed amount of Fe in x = 0.0, 0.01, 0.05, and 0.1 Fe-doped samples is 0.73%, 4.05% and 7.40%, respectively, indicating that the observed amount is less as compared to the actual doped amount.
- The XRD patterns exhibit broadening in the XRD peaks, indicating the nanometer regime of undoped and Fe-doped ZnS nanoparticles.
- The undoped and doped ZnS nanoparticles have cubic structure. W-H plots exhibit negative slope indicating that lattice is under compressive strain. The strain increases as the Fe-doping concentration is increased.
- The intensity of the XRD peaks reduces as the Fe-doping concentration is increased, indicating the deterioration of structural quality of ZnS with Fe-doping.
- As Fe concentration is increased, the lattice parameters have also been found slightly decreased, which indicates that the Fe-doped ZnS lattice is under compressive strain due to smaller radii of $Fe^{2+}$ ions as compared to $Zn^{2+}$.
- The UV-Vis. spectra indicate absorption edge at 321 nm in case of undoped ZnS nanoparticles, corresponding to a band gap of 3.86 eV, blue-shifted as compared to bulk ZnS, may be attributed to quantum confinement effects. The Fe-doped ZnS nanoparticles exhibit blue shift with increased Fe concentration as compared to undoped counterpart.

- The emission spectra of undoped and Fe-doped ZnS nanoparticles exhibit two peaks, at 360 nm and 438 nm.
- As Fe concentration in ZnS lattice is increased, the corresponding PL intensity of ZnS nanoparticles is decreased, indicating that $Fe^{2+}$ ions act as quenching centers.
- The Fe-doped ZnS nanoparticles indicate the magnetic behaviour with well resolved hysteresis loops, whereas undoped ZnS nanoparticles indicate diamagnetic character.
- ZnS nanoparticles with x = 0.05 Fe-doping concentration exhibit a weak ferromagnetic behaviour.

### 4.1.3 Co-doped ZnS nanoparticles

- Undoped and Co-doped ZnS nanoparticles have been synthesized via low temperature solvothermal technique using ethanol as solvent.
- TEM images reveal the estimated size of undoped and Co-doped ZnS nanoparticles ~10 nm. The sharp inter-atomic spacing values indicate high crystallanity of synthesized nanoparticles. EDS patterns of Co-doped ZnS nanoparticles confirm the presence of Co in ZnS samples.
- The observed doped amount of Co is found less as compared to actual doped amount, may be ascribed to the excessive washings of samples.
- Undoped and Co-doped ZnS nanoparticles indicate the cubic phase. Broadening in the XRD peaks indicate the nanometer regime of undoped and Co-doped ZnS nanoparticles.
- XRD peak positions shift towards higher Bragg's angles as the Co-doping concentration is increased. Lattice parameters are also found reduced with increased Co-doping concentration, indicating that the ZnS lattice is under compressive strain due to smaller radii of Co ions as compared to Zn ions.

- W-H plots exhibit negative slope indicating that lattice is under compressive strain. The strain increases as the Co-doping concentration is increased.
- The UV-Vis. spectra indicate blue shift in absorption edge in undoped and Co-doped ZnS nanoparticles when compared with bulk counterpart.
- The spectra obtained indicate the peak centered at 450 nm and 525 nm due to blue and yellow emission respectively.
- The PL intensity increases with the doping of cobalt ions up to x = 0.01 and 0.05 concentrations, but it reduces as the Co concentration is increased to 0.1.
- Undoped ZnS nanoparticles exhibit a mixed ferromagnetic character at lower magnetic field and diamagnetic character at higher field. As the Co concentration is increased to x = 0.01, M-H curves of ZnS nanoparticles indicate saturated ferromagnetic character, and diamagnetic character is induced at higher magnetic field.
- Further increase in Co concentration to x = 0.05 and 0.1 induces increased ferromagnetic character at lower magnetic fields and paramagnetic behaviour as the field is increased and no saturation has been observed till 15k Oe.
- The induced ferromagnetism may be ascribed to the intrinsic coupling between the doped Co atoms and not due to the aggregated Co atoms in the ZnS lattice, as no secondary phases have been observed in XRD analysis.

### 4.1.4 Ni-doped ZnS nanorods

- Undoped and Ni-doped ZnS nanorods have been synthesized using solvothermal chemical synthesis route.

- The morphology of the undoped and Ni-doped ZnS nanorods, analyzed using TEM, revealed high quality 1-D cylindrical nanorods with variable size. The variation in length ranges between 50-300 nm and diameter ~10 nm.
- EDS analysis confirms that Ni is present in the doped ZnS nanorods, however the observed amount is less than the actual doped amount.
- Undoped and Ni-doped ZnS nanorods exhibit wurtzite phase.
- No extra peaks of secondary phases have been indicated in Ni-doped samples, supporting that the dopant has been inserted a ZnS lattice and it doesn't form clusters outside ZnS.
- Texture coefficient, *TC(hkl)*, is maximum for *(002)* plane, indicating it to be a preferred direction of growth.
- Lattice parameters of Ni-doped ZnS nanorods found decreased when compared with undoped counterpart, supporting that the Ni atoms replaced the Zn atoms in the lattice.
- W-H plots exhibit negative slope indicating that lattice is under compressive strain. The strain increases as the Ni-doping concentration is increased.
- Maximum absorbance recorded at 325 nm in case of undoped ZnS nanorods, corresponding to the band gap of 3.81 eV, blue-shifted as compared to bulk counterpart. Further, as the Ni-doping is increased, the absorbance edge is blue-shifted as compared to undoped ZnS counterparts.
- The blue shift in Ni-doped nanorods may be ascribed to the lower ionic radius of Ni as compared to the replaced Zn in host ZnS lattice or The blue-shift may also be associated with the strain induced in ZnS lattice due to doping.
- The spectra depict two main peaks, at 340 nm and 438 nm, in undoped and Ni-doped ZnS nanorods. The peak at 340 nm may be attributed to wide band edge emission and blue

emission at 438 nm may be attributed to self activated luminescence and recombination of carriers between sulphur vacancies related donor and valence bands.

- The PL intensity has been observed to be reduced in Ni-doped ZnS nanorods as compared to undoped counterpart. The PL intensity also registers a quenching with increased Ni concentrations from x = 0.01 to 0.1.
- Undoped and Ni-doped ZnS nanorods exhibit ferromagnetic like behaviour.
- Increase in Ni-doping concentration up to x = 0.05, increases the magnetization with increased magnetic field. However, the saturation magnetization reduces as Ni-doping concentration is increased further up to x = 0.10.
- Decrease in magnetization at higher concentration may ascribe to super-exchange interaction caused due to increase in nearest neighbour antiferromagnetic coupling of Ni ion pairs in doped ZnS nanorods.

### 4.1.5 Fe-doped ZnS nanorods

- Undoped and Fe-doped ZnS nanorods have been synthesized using low temperature solvothermal chemical route, en and water mixture (1:1) has been used as solvent.
- The estimated average diameter of nanorods, as analyzed using TEM, has been found to be ~10 nm, length varying between 50-400 nm. The atomic-spacing of Fe-doped ZnS nanorods is slightly less as compared to the undoped counterpart.
- The undoped ZnS samples indicate the presence of Zn and S atoms; whereas, the doped ZnS samples indicate the presence of Fe; however, the observed Fe amount is lower than the actual doped amount.

- The XRD peaks can be indexed to wurtzite phase of undoped and Fe-doped ZnS nanorods. No extra peaks of secondary phases have been observed in case of Fe-doped samples, which support that Fe has been substituted in the ZnS lattice.
- Texture coefficient, *TC(hkl)*, is maximum for *(002)* plane, indicating it to be a preferred direction of growth.
- As the Fe concentration in ZnS matrix is increased, the lattice parameters are slightly decreased, which indicates that the Fe-doped ZnS structure is under compressive strain due to different ionic radii of Fe ions as compared to replaced Zn ions. The *d*-spacing values decrease with increased Fe concentrations.
- W-H plots exhibit negative slope indicating that lattice is under compressive strain. The strain increases as the doping concentration is increased.
- The absorption spectra of undoped and Fe-doped ZnS nanorods indicate absorbance edge blue-shift as compared to the bulk counterpart and *w.r.t.* undoped counterpart.
- PL spectra indicate two wide peaks, 447 nm and 533 nm, indicating the blue and green emission respectively.
- The PL intensity increases with increased Fe concentration up to x = 0.05. As the Fe concentration is increased further up to x = 0.10, quenching in PL intensity is observed.
- M-H curves indicate that undoped ZnS nanorods exhibit a diamagnetic character, whereas, the Fe-doped ZnS nanorods exhibit ferromagnetic character up to 5000 Oe.
- As the magnetic field is increased further up to 2 T, there is a sharp decrease in the magnetization and diamagnetic character appears to be induced. Small coercivity values of all samples indicate the soft magnetic behaviour of doped ZnS nanorods.

- The M-H curves indicate that ferromagnetism becomes more prominent as the Fe concentration is increased up to x = 0.05.
- As the Fe-doping concentration is increased further to x = 0.10, the saturation magnetization is found reduced. The ferromagnetism at lower concentration may be ascribed to the intrinsic coupling between the doped Fe-Fe atoms. As the concentration is further increased to x = 0.1, the Fe-Fe distance in the ZnS matrix is reduced, leading to antiferromagnetic interaction, which may cause a decrease in the magnetization.

### 4.1.6 Co-doped ZnS nanorods

- The undoped and Co-doped ZnS nanorods have been synthesized using en and water mixture (1:1) as solvent.
- TEM images indicate 1-D structure of undoped and Co-doped ZnS nanorods with varied length raging between 50-300 nm and diameter ~10 nm.
- HRTEM images indicate reduced inter-atomic spacing in case of Co-doped ZnS nanorods as compared to undoped counterpart. EDS spectra identify Co in doped ZnS samples.
- The XRD peaks indicate the wurtzite phase of undoped and Co-doped ZnS nanorods.
- No extra peaks of secondary phases have been observed in case of Co-doped samples, which supports that Fe has been substituted in the ZnS lattice.
- Texture coefficient, *TC(hkl),* is maximum for *(002)* plane, for all samples indicating it to be a preferred direction of growth.
- A slight shift in the peak position towards a higher diffraction angle and reduced peaks intensity with increased Co concentration indicate insertion of Co ions in ZnS lattice.
- W-H plots exhibit negative slope indicating that lattice is under compressive strain. The strain increases as the Co-doping concentration is increased.

- UV-Vis. spectra of undoped and Co-doped ZnS nanorods are blue-shifted as compared to bulk counterpart.
- Blue-shifting in Co-doped ZnS samples as compared to undoped counterpart may be attributed to formation of new energy levels by doped Co within the ZnS energy band or The blue-shift may also be associated with the strain induced in ZnS lattice due to doping.
- The emission spectra of undoped and Co-doped ZnS exhibit two peaks, positioned at 422 nm and 485 nm.
- The 422 nm peak is analogous to the blue emission and 485 nm peak originates due to bluish-green emission. The blue emission peak at 422 nm may ascribe to radiative recombination between sulphur vacancies related donor energy levels and purity of phase of host ZnS material, whereas, the peak centred at 485 nm may attributed to surface zinc ions.
- The PL intensity increases as the Co concentration is increased up to x = 0.05. Further increase in Co concentration to x = 0.10, leads to quenching in the PL intensity.
- As the Co concentration is increased to x = 0.10, the doped Co ions interfere with the radiative recombination process, which diminishes the effect of creating new radiation centers, resulting in the quenching of fluorescence intensity at higher doping concentrations.
- The undoped ZnS nanorods exhibit a diamagnetic character. As the Co-doping concentration in ZnS matrix is increased from x = 0.0 to 0.10, magnetic moment is increased with strong saturation magnetization.

- The strong ferromagnetic character in Co-doped ZnS nanorods may be ascribed to the exchange interaction between the localized *'d'* spins of the Co ions and free delocalized carriers which increases with increase in Co concentration.
- Ferromagnetic saturation in the Co-doped ZnS nanorods may be ascribed to the intrinsic coupling between the doped Co ions.
- As no extra peaks have been observed in XRD spectra of Co-doped ZnS nanorods, hence it is assumed that the saturation magnetization is solely due to doped cobalt ions incorporated in ZnS lattice.

## 4.2 Future scope of research work

- Present research work analyses the properties of ZnS nanostructures at different dopant concentrations at room temperature. This study can be extended to low temperatures as well as high temperatures.
- The properties of doped ZnS nanostructures can be studied at the transition metals concentrations beyond x = 0.10.
- More sophisticated techniques like, X-ray photoelectron spectroscopy (XPS) and X-rays absorption spectroscopy (XAS) can be utilized for understanding the host and guest elements interactions.
- The study can be extended to rare earth-doped ZnS nanostructures.

# References


[1] R.P. Feynman, There's Plenty of Room at the Bottom, Miniaturization, H. D. Gilbert, ed., Reinhold Publishing, New 1961 pp. 282-296.

[2] K.E. Drexler, Molecular engineering: An approach to the development of general capabilities for molecular manipulation, Proc. Natl. Acad. Sci. **78**, (1981) 5275-5278.

[3] A. Gruverman, A. Kholkin, Nanoscale ferroelectric: processing, characterization and future trends, Rep. Prog. Phys. **69**, (2006) 2443-2474.

[4] N. Aggarwal, J. Sood, T. Kumar, Anisotropic diffusion of a fluid confined to different geometries at nano- scale, Nanotechnology **18**, (2007) 335707.

[5] C.P. Sibu, S.R. Kumar, P. Mukundan, K.G.K. Warrier, Structural modifications and associated properties of lanthanum oxide doped sol gel nano sized titanium oxide, Chem. Mater. **14**, (2002) 2876-2881.

[6] D. Demirskyi, D. Agrawal, A. Ragulya, Tough ceramics by microwave sintering of nanocrystalline titanium diboride ceramics, Ceramic Intnl. **40**, (2014) 1303-1310.

[7] C.F. Chau, S.H. Wu, G.C. Yen, The development of regulations for food nanotechnology, Trends. Food. Sci. Tech. **18**, (2007) 269-280.

[8] R. R. Schaller, Moore's law: past, present and future, IEEE, Spectrum **34,** (1997) 52-59.

[9] J.K. Furdyna, Dilute magnetic semiconductors, J. Appl. Phys. **64**, (1988) R29.

[10] M.L. Steigerwald, L.E. Brus, Semiconductor crystallites: a class of large molecules, Acc. Chem. Res. **23**, (1990) 183-186.

[11] D. Kim, K.D. Min, J. Lee, J.H. Park, J.H. Chun, Influences of surface capping on particle size and optical characteristics of ZnS:Cu nanocrystals, Mater. Sci. Eng. B **131**, (2006) 13.

[12] Y. Wang, N. Herron, Nanometer-sized semiconductor clusters: materials synthesis, quantum size effects, and photophysical properties, J. Phys. Chem. **95**, (1991) 525.

[13] V.L. Colvin, M.C. Schlamp, A.P. Alivisatos, Light-emitting-diodes made from cadmium selenide nanocrystals and a semiconducting polymer, Nature **370**, (1994) 354.

[14] Y. Okada, N.J. Ekins-Daukes, T. Kita, R. Tamaki, M. Yoshida, A. Pusch, O. Hess, C.C. Phillips, D. J. Farrell, K. Yoshida, N. Ahsan, Y. Shoji, T. Sogabe, J.-F. Guillemoles, Intermediate band solar cells: Recent progress and future directions, Appl. Phys Rev. 2, (2015) 021302.

[15] D. Garcia-Alonso, S. E. Potts, C.A.A. van Helvoirt, M.A. Verheijena, W.M.M. Kessels, Atomic layer deposition of B-doped ZnO using triisopropyl borate as the boron precursor and comparison with Al-doped ZnO, J. Mater. Chem. C **3**, (2015) 3095.

[16] D. Sharma, D. Mohan, Photorefractive parameters in GaAs:Cr with externally applied magnetic field, Optik - International Journal for Light and Electron Optics **124**, (2013) 4557-4560.

[17] S. Rani, D. Mohan, N. Kishore, Study of optical phase conjugation in amorphous $Zn_x$–$S_y$–$Se_{100-x-y}$ chalcogenide thin films using degenerate four-wave mixing, Spectrochim. Acta Mol. Biomol. Spectrosc. **118**, (2014) 733-736.

[18] M. Okutan, S.E. San, E. Basaran, F. Yakuphanoglu, Determination of phase transition from nematic to isotropic state in carbon nano-balls' doped nematic liquid crystals by electrical conductivity-dielectric measurements, Phys. Lett. A **339**, (2005) 461-465.

[19] J.D. Bryan, D.R. Gamelin, Doped semiconductor nanocrystals: synthesis, characterization, physical properties, and applications, Prog. Inorg. Chem. **54**, (2005) 47-126.

[20] K.P. Bhatti, S. Chaudhary, D.K. Pandya, S.C. Kashyap, Intrinsic and extrinsic origin of room temperature ferromagnetism in ZnO:Co (5 at. %), J. Appl. Phys. **101**, (2007) 103919.

[21] Y. Shon, S. Lee, H.C. Jeon, C.S. Park, T.W. Kang, J.S. Kimb, E.K. Kimb, C.S. Yoon, Y. Kim, The study of structural, optical, and magnetic properties of undoped and p-type GaN implanted with Mn+ (10 at.%), Mater. Sci. Eng. B **146**, (2008) 196-199.

[22] S.C. Kashyap, K. Gopinadhan, P.K. Pandya, S. Chaudhary, A study of room-temperature ferromagnetism in transition metal and fluorine-doped spray-pyrolyzed $SnO_2$ thin films, J. Magn. Magn. Mat. **321**, (2009) 957.

[23] W.C. Chueh, A.H. McDaniel, M.E. Grass, Y. Hao, N. Jabeen, Z. Liu, S.M. Haile, K.F. McCarty, H. Bluhm, F. El Gabaly, Highly enhanced concentration and stability of reactive Ce3+ on doped CeO2 surface revealed in operando, Chem. Mater. **24**, (2012) 1876.

[24] I. Garg, H. Sharma, N. Kapila, K. Dharamvir, V.K., Jindal, Transition metal induced magnetism in smaller fullerenes (Cn for $n \leq 36$), Nanoscale **3**, (2011) 217-224.

[25] W. Li, S.K. Karna, H. Hsu, Chi-Yen Li, Chi-Hung Lee, R. Sankar, F.C. Chou, Development of a ferromagnetic component in the superconducting state of Fe-excess $Fe_{1.12}Te_{1-x}Se_x$by electronic charge redistribution, Sci. Rep. **5**, (2015) 10951.

[26] K. Sato, P.H. Dederichs, H. Katayama-Yoshida, J. Kudrnovsky, Exchange interactions in diluted magnetic semiconductors, J. Phys.: Condens. Matter **16**, (2004) S5491-S5497.

[27] C. Zener, Interaction between the d-shells in the transition metals, Phys. Rev. **81**, (1951) 440.

[28] M.A. Ruderman, C. Kittel, Indirect exchange coupling of nuclear magnetic moments by conduction electrons, Phys. Rev. **96**, (1954) 99.

[29] K. Yosida, Magnetic properties of Cu-Mn alloys, Phys. Rev. **106**, (1957) 893.

[30] T. Dietl, H. Ohno, F. Matsukura, J. Cibert, D. Ferrand, Zener model description of ferromagnetism in Zinc-blende magnetic semiconductors, Science **287**, (2000) 1019.

[31] J.M.D. Coey, M. Venkatesan, C.B. Fitzgerald, Donor impurity band exchange in dilute ferromagnetic oxides, Nat. Mater. **4**, (2005) 173-179.

[32] T. Sidot, Recherches sur la crystallisation de quelque sulphures métalliques et sur les propriétés de la blende hexagonale, Comptes .Rend. Ac. Sci. **62**, (1866) 999-1001.

[33] B. Gudden, R.W. Pohl. Gber ausleuchteung der phosphoreszenz durch elektrische felder, Zeitschrift fhr Physik **2**, (1929) 192-6.

[34] V.A. Ivanov, Diluted magnetic semiconductors and spintronics, Bull. Russ. Acad. Sci. Phys. **71**, (2007) 1610-1612.

[35] R. R. Galazka, Proc. 14th Int. Conf. on Physics of Semiconductors, Inst. Phys. Conf. Ser. 43, edited by B.L.H. Wilson, Institute of Physics, Bristol, 1978 p. 133.

[36] J.K. Furdyna, Diluted magnetic semiconductors: an interface of semiconductor physics and magnetism J. Appl. Phys. **53**, (1982) 7637.

[37] J.K. Furdyna, Diluted magnetic semiconductors: issues and opportunities J. Vac. Sci. Technol. **4**, (1986) 2002.

[38] S.J. Pearton, C.R. Abernathy, D.P. Norton, A.F. Hebard, Y.D. Park, L.A. Boatner, J.D. Budai, Wide band gap ferromagnetic semiconductors and oxides, Mat. Sci. Eng. R **40**, (2003) 137-168.

[39] J.M. D. Coey, Dilute magnetic oxides, Curr. Opin. Solid State Mater. Sci. **10**, (2006) 83-92.

[40] V.A. Ivanov, E.A. Ugolkova, O.N. Pashkova, V.P. Sanygin, A.G. Padalko, Ferromagnetism in dilute magnetic semiconductors and new materials for spintronics, J. Magn. Magn. Mater. **300**, (2006) e32-e36.

[41] C. Liu, Fi Yun, H. Morkoc, Ferromagnetism of ZnO and GaN: a review, J. Mater. Sci. Mater. Electron. **16**, (2005) 555-597.

[42] S. Kumar, S. Kumar, S. Jain, N.K. Verma, Magnetic and structural characterization of transition metal co-doped CdS nanoparticles, Appl. Nanosci. **2**, (2012) 127-31.

[43] J. Singh, N.K. Verma. Synthesis and characterization of Fe-doped CdSe nanoparticles as dilute magnetic semiconductor. J. Supercond. Nov. Magn. **25**, (2012) 2425-30.

[44] S. Singh, N. Jahan, A. Khanna, G.S. Lotey, N.K. Verma, Room temperature ferromagnetic behaviour of indium doped $SnO_2$ dilute magnetic semiconductor nanocrystalline thin films, Chalcogenide Lett. **9**, (2012) 73-8.

[45] S. Kumar, Z. Jindal, N. Kumari, N.K. Verma, Solvothermally synthesized europium doped CdS nanorods: applications as phosphors. J. Nanopart. Res. **13**, (2011) 5465-5471.

[46] S. Kumar, S. Kumar, N.K. Verma, S.K. Chakravarti, Room temperature ferromagnetism in solvothermally synthesized pure CdSe and CdSe:Ni nanorods, J. Mater. Sci. Mater. Electron. **22**, (2011) 1456-1459.

[47] S. Kumar, S. Kumar, N.K. Verma, S.K. Chakravarti, Room temperature magnetism in Ni-doped CdSe nanoparticles. J. Mater. Sci. Mater. Electron. **22**, (2011) 901-904.

[48] S. Kumar, S. Kumar, N.K. Verma, S.K. Chakravarti, Room temperature ferromagnetic behaviour of Eu-doped $Cd_{1-x}Zn_xS$ nanoparticles, J. Mater. Sci. Mater. Electron. **22**, (2011) 523-526.

[49] S. Kumar, N. Kumari, S. Kumar, S. Jain and N.K. Verma, Synthesis and characterization of Ni-doped CdSe nanoparticles: magnetic studies in 300K-100K temperature range, Appl. Nanosci. **2**, (2012) 437-443.

[50] G.S. Lotey, Z. Jindal, V. Singhi, N.K. Verma, Structural and photoluminescence properties of Eu-doped ZnS nanoparticles, Mater. Sci. Semicon. Proc. **16**, (2013) 2044.

[51] S. Kumar, N.K. Verma, M.L. Singla, Diffuse reflectance and reflective flexible coatings of capped ZnS nanoparticles, Mater. Chem. Phys. **142**, (2013) 734.

[52] S. Kumar, N.K. Verma, M.L. Singla, Reflective properties of ZnS nanoparticles Coating, J. Coat. Technol. Res. **8**, (2011) 223.

[53] Z. Jindal, N.K. Verma, Effect of Mn doping on solvothermal synthesis of CdS nanowires, Mater. Sci. Appl. **1**, (2010) 210-216.

[54] Z. Jindal, N.K. Verma, Photoluminescent properties of ZnS:Mn nanoparticles with in-built surfactant, J. Mater. Sci. **43**, (2008) 6539-6545.

[55] Z. Jindal, N.K. Verma, Structural and optical properties of CdS nanorods and CdS/ZnS nanoslabs, Physica E Low Dimens. Syst. Nanostruct. **43**, (2011) 1021-1025.

[56] K. Kaur, G. S. Lotey, N.K. Verma, Optical and magnetic properties of Fe-doped CdS dilute magnetic semiconducting nanorods, J. Mater. Sci. Mater. Electron. **25**, (2014) 2605.

[57] K. Kaur, G.S. Lotey, N.K. Verma, Structural, optical and magnetic properties of cobalt-doped CdS dilute magnetic semiconducting nanorods, Mater. Chem. Phys. **143**, (2013) 41-46.

[58] J. Singh, N.K. Verma, Synthesis and characterization of Fe-doped CdSe nanoparticles as Dilute Magnetic Semiconductor, J. Supercond. Nov. Magn. **25**, (2012) 2425.

[59] J. Singh, S. Kumar, N.K. Verma, Enhancement of room temperature ferromagnetism in $Cd_{1-x}Ni_xSe$ nanoparticles, J. Mater. Sci. Mater. Electron. **25**, (2014) 2267-2272.

[60] J. Singh, N.K. Verma, Structural, optical and magnetic properties of cobalt- doped CdSe nanoparticles, J. Bull. Mater. Sci. **37**, (2014) 1-7.

[61] J. Singh, S. Kumar, N.K. Verma, Effect of Ni-doping concentration on structural, optical and magnetic properties of CdSe nanorods, J. Mat. Sci. Semicon. Proc. **26**, (2014) 1-6.

[62] J. Singh, G.S. Lotey, N.K. Verma, Structural, optical and magnetic properties of Cr-doped CdSe nanoparticles, Dig. J. Nanomater. Bios. **6**, (2011) 1733-1740.

[63] G.S. Lotey, J. Singh, N.K. Verma, Room temperature ferromagnetism in Tb-doped ZnO dilute magnetic semiconducting nanoparticles, J. Mater. Sci. Mater. Electron. **24**, (2013) 3611-3616.

[64] H.S. Bhatti, R. Sharma, N.K. Verma, N. Kumar, S.R. Vadera, K. Manzoor, Lifetime shortening in doped ZnS nanophosphors J. Phys. D: Appl. Phys. **39**, (2006) 1754

[65] R. Bhargava, D. Gallagher, T. Welker, Doped nanocrystals of semiconductors-a new class of luminescent materials, J. Lumin. **60**, (1994) 275-80.

[66] R. Bhargava, D. Gallagher, X. Hong, A. Nurmikko, Optical properties of manganese-doped nanocrystals of ZnS, Phys. Rev. Lett. **72**, (1994) 416-9.

[67] N. Tsujii, H. Kitazawa, G. Kido. Magnetic properties of Mn-and Eu-doped ZnS nanocrystals, J. Appl. Phys. **93**, (2003) 6957-9.

[68] H. Yuan, X. Yan, Z. Zhang, D. Liu, Z. Zhou, L. Cao, J.X. Wang, Y. Gao, L. Song, L.F. Liu , X.W. Zhao, X.Y. Dou, W.Y. Zhou, S.S. Xie. Synthesis, optical, and magnetic properties of $Zn_{1-x}Mn_xS$ nanowires grown by thermal evaporation, J. Cryst. Growth **271**, (2004) 403-8.

[69] S. Biswas, S. Kar, S. Chaudhuri, Optical and magnetic properties of manganese-incorporated zinc sulfide nanorods synthesized by a solvothermal process, J. Phys. Chem. B **109**, (2005) 17526-30.

[70] S. Kar, S. Biswas, S. Chaudhuri, Optical and magnetic properties of Mn-incorporated ZnS nanorods, Synth. React. Inorg. Metal-Org. Nano-Met. Chem. **36**, (2006) 193-6.

[71] S. Bhattacharya, D. Chakravorty, Electrical and magnetic properties of cold compacted iron-doped zinc sulfide nanoparticles synthesized by wet chemical method, Chem. Phys. Lett. **444**, (2007) 319-23.

[72] Z.H. Wang, D.Y. Geng, D. Li, Z.D. Zhang, Cluster spin-glasslike behaviour in nanoparticles of diluted magnetic semiconductors ZnS:Mn, J. Mater. Res. **22**, (2007) 2376-83.

[73] I. Sarkar, M. Sanyal, S. Kar, S. Biswas, S. Banerjee, S. Chaudhuri, S. Takeyama, H. Mino, F. Komori, Ferromagnetism in zinc sulfide nanocrystals: dependence on manganese concentration, Phys. Rev. B **75**, (2007) 224409.

[74] S. Sambasivam, D.P. Joseph, J.G. Lin, C. Venkateswaran, Synthesis and characterization of thiophenol passivated Fe-doped ZnS nanoparticles, Mater. Sci. Eng. B.**150**, (2008) 125–129.

[75] T. Kang, J. Sung, W. Shim, H. Moon, J. Cho, Y. Jo, W. Lee, B. Kim, Synthesis and magnetic properties of single-crystalline Mn/Fe-doped and Co-doped ZnS nanowires and nanobelts, J. Phys. Chem. C **113**, (2009) 5352-7.

[76] S. Sambasivam, D.P. Joseph, J,G. Lin, C. Venkateswaran, Doping induced magnetism in Co-doped ZnS nanoparticles, J. Solid State Chem. **182**, (2009) 2598–601.

[77] Y. Li, Z. Zhou, P. Jin, Y. Chen, S.B. Zhang, Z. Chen, Achieving ferromagnetism in single-crystalline ZnS wurtzite nanowires via chromium doping, J. Phys. Chem. C **114**, (2010) 12099–103.

[78] H. Chen, D. Shi, J. Qi, Comparative studies on the magnetic properties of ZnS nanowires doped with transition metal atoms, J. Appl. Phys. **109**, (2011) 084338-9.

[79] N. Eryong, L. Donglai, Z. Yunsen, B. Xue, Y. Liang, J. Yong, J. Zhifeng, S. Xiaosong, Photoluminescence and magnetic properties of Fe-doped ZnS nano-particles synthesized by chemical co-precipitation, Appl. Surf. Sci. **257**, (2011) 8762-6.

[80] F.J. Owens, L. Gladczuk, R. Szymczak, P. Dluzewski, A. Wisniewski, H. Szymczak, A. Golnik, C. Bernhard, C. Niedermayer, High temperature magnetic order in zinc sulfide doped with copper, J. Phys. Chem. Solids **72**, (2011) 648-52.

[81] D.A. Reddy, G. Murali, R. Vijayalakshmi, B. Reddy, Room-temperature ferromagnetism in EDTA capped Cr-doped ZnS nanoparticles, Appl. Phys. A Mater. Sci. Process. **105**, (2011) 119-24.

[82] D.A. Reddy, G. Murali, B. Poornaprakash, R. Vijayalakshmi, B. Reddy, Structural, optical and magnetic properties of $Zn_{0.97-x}Cu_xCr_{0.03}S$ nanoparticles, Appl. Surf. Sci. **258**, (2012) 5206-11.

[83] D.A. Reddy, G. Murali, B. Poornaprakash, R. Vijayalakshmi, B. Reddy, Effect of annealing temperature on optical and magnetic properties of Cr doped ZnS nanoparticles, Solid State Commun. **152**, (2012) 596-602.

[84] S. Senthilkumaar, R.T. Selvi, N.G. Subramaniam, T.W. Kang, Facile synthesis and magnetic properties of manganese doped ZnS nanorods, Superlattices Microstruct. **51**, 201273-9.

[85] M. Ragam, G. Kalaiselvan, S. Arumugam, N. Sankar, K. Ramachandran, Room temperature ferromagnetism in $Mn_xZn_{1-x}S$ (x = 0.00–0.07) nanoparticles, J. Alloys Compd. **541**, (2012) 222-6.

[86] H. Rozale, A. Lakdja, A. Chahed, O. Benhelal, First principles study of half-metallic ferromagnetism in $Zn_{1-x}Eu_xS$, Superlattices Microstruct. **52**, (2012) 376-86.

[87] S.P. Patel, J.C. Pivin, M.K. Pate, J. Won, R. Chandra, D. Kanjilal, L. Kumar, Defects induced magnetic transition in Co doped ZnS thin films: effects of swift heavy ion irradiation. J. Magn. Magn. Mater. **324**, (2012) 2136-41.

[88] S. Kumar, C.L. Chen, C.L. Dong, Y.K. Ho, J.F. Lee, T.S. Chan, R. Thangavel, K. Chen , B.H. Mok, S.M. Rao, M.K. Wu, Room temperature ferromagnetism in Ni doped ZnS nanoparticles. J. Alloys Compd. **554**, (2013) 357-62.

[89] M. Wei, J. Cao, H. Fu, J. Yang, Y. Yan, L. Yang, D. Wang, D. Han, L. Fan, B. Wang, The structure and room temperature ferromagnetism property of the $ZnS:Cu^{2+}$ nanoparticles, Mat. Sci. Semicond. Proc. **16**, (2013) 928-932.

[90] P.C. Patel, P.C. Srivastava, Fe doping in ZnS for realizing nanocrystalline-diluted magnetic semiconductor phase, J. Mater. Sci. **49**, (2014) 6012-6019.

[91] W. Fang, Y. Liu, B. Guo, L. Peng, Y. Zhong, J. Zhang, Z. Zhao, Room temperature ferromagnetism and cooling effect in dilute Co-doped ZnS nanoparticles with zinc blende structure, J. Alloys Compd. **584**, (2014) 240–243.

[92] H. Zhang, Q. Chen, H. Zhang, W. Rui, Q. Ding, Y. Cao, W. Zhong, K. Shen, J. Du, D. Xiang, Q. Xu, Interstitial $H^+$-mediated ferromagnetism in Co-doped ZnS, J. Supercond. Nov. Magn. **28**, (2015) 1389-1393.

[93] J. Yang, H. Niu, J. Cao, D. Han, S. Yang, Q. Liu, T. Wang, Room temperature ferromagnetism and optical property of $Zn_{1-x}Co_xS$ nanorods, Superlattices Microstruct. **82**, (2015) 75–81.

[94] Y. Zhang, H. Qin, Y. Bao, J. Hu, Study of ferromagnetism in $Bi_2S_3$ and ZnS nanocrystalline powders, Physica B **406,** (2011) 4661-4665.

[95] C. Peng, Yong Liang, Kefan Wang, Y. Zhang, G. Zhao, Y. Wang, Possible origin of ferromagnetism in an undoped ZnO d0 semiconductor, J. Phys. Chem. C **116**, (2012) 9709-9715.

[96] A. Shan, W. Liu, R. Wang, C. Chen, Magnetism in undoped ZnS nanotetrapods, Phys. Chem. Chem. Phys. **15**, (2013) 2405.

[97] I. Sarkar, M.K. Sanyal, S. Takeyama, S. Kar, H. Hirayama, H. Mino, F. Komori, S. Biswas, Suppression of Mn photoluminescence in ferromagnetic state of Mn-doped ZnS nanocrystals, Phys. Rev. B **79**, (2009) 054410-6.

[98] M. Wei, J. Yang, Y. Yan, J. Cao, H. Fu, B. Wang, L. Fan, Q. Zuo, The investigation of the maximum doping concentration of iron in zinc sulfide nanowires, and its optical and ferromagnetic properties, Superlattices Microstruct **54**, (2013) 181-187.

[99] A. Goktaş, I. H. Mutlu, Room temperature ferromagnetism in Mn-doped ZnS nanocrystalline thin films grown by sol–gel dip coating process, J. Sol-Gel Sci. Technol. **69**, (2014) 120-129.

[100] X. Zeng, S. Yan, J. Cui, H. Liu, J. Dong, W. Xia, M. Zhou, H. Chen, Size- and morphology-dependent optical properties of ZnS:Al one-dimensional structures, J. Nanopart. Res. **17**, (2015) 188.

[101] H. Soni, M. Chawda, D. Bodas, Electrical and optical characteristics of Ni doped ZnS clusters, Mater. Lett. **63**, (2009) 767–769.

[102] N.G. Imam, M.B. Mohamed, Optical properties of diluted magnetic semiconductor Cu:ZnS quantum dots, Superlattices Microstruct. **73**, (2014) 203–213.

[103] Y. Zhang, W. Liu, B. Liu, R. Wang, Morphology-structure diversity of ZnS nanostructures and their optical properties, Rare Met. **33**, (2014) 1-15.

[104] M. Mall, L. Kumar, Optical studies of $C^{d2+}$ and $M^{n2+}$ Co-doped ZnS nanocrystals, J. Lumin. **130**, (2010), 660–665.

[105] G. Murugadoss, B. Rajamannan, V. Ramasamy, Synthesis, characterization and optical properties of water-soluble ZnS:Mn2+ nanoparticles, J. Lumin. 130, (2010) 2032–2039.

[106] W.Q. Peng, G.W. Cong, S.C. Qu, Z.G. Wang, Synthesis and photoluminescence of ZnS:Cu nanoparticles, Opt. Mater. **29**, (2006) 313–317.

[107] V. Ramasamy, K. Praba, G. Murugadoss, Synthesis and study of optical properties of transition metals doped ZnS nanoparticles, Spectrochim. Acta. A Mol. Biomol. Spectrosc. **96**, (2012) 963–971.

[108] M. Wang, L. Sun, X. Fu, C. Liao, C. Yan, Synthesis and optical properties of ZnS:Cu(II) nanoparticles, Solid State Commun. **115**, (2000) 493–496.

[109] A. Goudarzi, R. Sahraei, G.M. Aval, M.H. Ullah, S.S Park, A. Avane, M. Choi, C. Ha, Low-temperature growth of nanocrystalline Mn-doped ZnS thin films prepared by chemical bath deposition and optical properties, Chem. Mater. **21**, (2009) 2375-2385.

[110] Z. He, Y. Su, Y. Chen, D. Cai, J. Jiang, L. Chen, Self-catalytic growth and photoluminescence properties of ZnS nanostructures, Mater. Res. Bull. **40**, (2005) 1308–1313.

[111] W. Wang, F. Huang, Y. Xia, A. Wang, Photophysical and photoluminescence properties of co-activated ZnS:Cu, Mn phosphors, J. Lumin. **128**, (2008) 610-614.

[112] R. Kripal, A.K. Gupta, S.K. Mishra, R.K. Srivastava, A.C. Pandey, S.G. Prakash, Photoluminescence and photoconductivity of ZnS:$Mn^{2+}$ nanoparticles synthesized via co-precipitation method, Spectrochim. Acta. A Mol. Biomol. Spectrosc. **76**, (2010) 523–530.

[113] L. Peng, Y. Wang, Effects of the template composition and coating on the photoluminescence properties of ZnS:Mn nanoparticles, Nanoscale Res. Lett. **5**, (2010) 839-845.

[114] X.M. Meng, J. Liu, Y. Jiang, I. Bello, W.W. Chen, S.T. Lee, C.S. Lee, Structure- and size-controlled ultrafine ZnS nanowires, Chem. Phys. Lett. **382**, (2003) 434-438.

[115] J. Cao, J. Yang, Y. Zhang, L. Yang, Y. Wang, M. Wei, M. Gao, X. Liu, Z. Xie, Y. Liu, Optimized doping concentration of manganese in zinc sulfide nanoparticles for yellow-orange light emission, J. Alloys Compd. **486**, (2009) 890–894.

[116] P. Yang, M. Lu, D. Xu, D. Yuan, J. Chang, G. Zhou, M. Pan, Strong green luminescence of $Ni^{2+}$ -doped ZnS nanocrystals, Appl. Phys. A **74,** (2002) 257-259.

[117] N. Karar, S. Raj, F. Singh, Properties of nanocrystalline ZnS:Mn, J. Cryst. Growth **268**, (2004) 585-589.

[118] Z. Quan, D. Yang, C. Li, D. Kong, J. Lin, P. Yang, Z. Cheng, Multicolor tuning of Manganese-Doped ZnS colloidal nanocrystals, Langmuir **25**, (2009) 10259-10262.

[119] S. Kumar, N.K. Verma, M.L. Singla, Reflective characteristics of Ni doped ZnS nanoparticle-pigment and their coatings, Chalcogenide Lett. **8**, (2011) 561-569.

[120] D. Dinsmore, D. S. Hsu, S. B. Qadri, J. O. Cross, T. A. Kennedy, H. F. Gray, B. R. Ratna, Structure and luminescence of annealed nanoparticles of ZnS:Mn, J. Appl. Phys. **88**, (2000) 4985-4993.

[121] R. Chauhan, A. Kumar, R.P. Chaudhary, Photocatalytic degradation of methylene blue with Cu doped ZnS nanoparticles, J. Lumin. **145**, (2014) 6-12.

[122] C. Xu, R. Zhou, W. He, L. Wu, P. Wu, X. Hou, Fast imaging of eccrine latent fingerprints with nontoxic Mn-Doped ZnS QDs, Anal. Chem. **86**, (2014) 3279-3283.

[123] P. Wu, L. Miao, H. Wang, X. Shao, X. Yan, A multidimensional sensing device for the discrimination of proteins based on manganese-doped ZnS quantum dots, Angew. Chem. Int. Ed. Engl. **50**, (2011) 8118-8121.

[124] L. Ma, W. Chen, ZnS:Cu, Co water-soluble afterglow nanoparticles: synthesis, luminescence and potential applications, Nanotechnology **21**, (2010) 385604.

[125] O. Khani, H.R. Rajabi, M.H. Yousefi, A.A. Khosravi, M. Jannesari, M. Shamsipur, Synthesis and characterizations of ultra-small ZnS and $Zn_{(1-x)}Fe_xS$ quantum dots in aqueous media and spectroscopic study of their interactions with bovine serum albumin, Spectrochim. Acta. A Mol. Biomol. Spectrosc. **79**, (2011) 361-369.

[126] M. Geszke-Moritz, G. Clavier, J. Lulek, R. Schneider, Copper- or manganese-doped ZnS quantum dots as fluorescent probes for detecting folic acid in aqueous media, J. Lumin. **132**, (2012) 987–991.

[127] W. Zou, J. Qiao, X. Hu, X. Ge, H. Lian, Synthesis in aqueous solution and characterisation of a new cobalt-doped ZnS quantum dot as a hybrid ratiometric chemosensor, Anal. Chim. Acta. **708**, (2011) 134-140.

[128] M. Geszke-Moritz, H. Piotrowska, M. Murias, L. Balan, M. Moritz, J. Lulek, R. Schneider, Thioglycerol-capped Mn-doped ZnS quantum dot bioconjugates as efficient two-photon fluorescent nano-probes for bioimaging, J. Mater. Chem. B **1**, (2013) 698-706.

[129] A.C. Small, J.H. Johnston, N. Clark, Inkjet printing of water "soluble" doped ZnS quantum dots, Eur. J. Inorg. Chem. **2010**, (2010) 242-247.

[130] P. Wu , Y. He, H. Wang, X. Yan, Conjugation of glucose oxidase onto Mn-doped ZnS quantum dots for phosphorescent sensing of glucose in biological fluids, Anal. Chem. **82**, (2010) 1427–1433.

[131] C.S. Pathak, M.K. Mandal, enhanced photoluminescence properties of $Mn^{2+}$ doped ZnS nanoparticles, Chalcogenide Lett. **8**, (2011) 147-153.

[132] B.B. Srivastava, S. Jana, N.S. Karan, S. Paria, N.R. Jana, D.D. Sarma, N. Pradhan, Highly luminescent Mn-doped ZnS nanocrystals:gram-scale synthesis, J. Phys. Chem. Lett. **1**, (2010) 1454-1458.

[133] http://minerva.mlib.cnr.it/mod/book/view.php?id=269&chapterid=105 (Last accessed on 21. 11.2015).

[134] R.D. Shannon, Revised effective ionic radii and systematic studies of interatomic distances in halides and chalcogenides, Acta. Cryst. **A32**, (1976) 751-767.

[135] W. Chen, Z.G. Wang, Z.J. Lin, L.Y. Lin, Thermoluminescence of ZnS nano particles, Appl. Phys. Lett. **70**, (1997) 1465-1467.

[136] D.M. Wilhemly, E. Matijevic, Preparation and properties of monodispersed spherical-colloidal particles of zinc sulphide, J. Chem. Soc. Faraday Trans. **80**, (1984) 563-570.

[137] E.J. Donahue, A. Roxburgh, M. Yurchenko, Sol-gel preparation of zinc sulfide using organic dithiols-recent trends and applications, Mater. Res. Bull. 33, (1998) 323-329.

[138] S. Biswas, S. Kar, Fabrication of ZnS nanoparticles and nanorods with cubic and hexagonal crystal structures: a simple solvothermal approach, Nanotechnology **19**, (2008) 045710

[139] K. Shigeo, T. Shimoguchi, H. Takahashi, S. Motoyama, F. Kano, M. Yokoyama, S. Satou, Optimum growth condition of single-crystalline undoped ZnS grown by the molecular-beam-epitaxial method using a $H_2S$ gas source, J. Appl. Phys. **64**, (1998) 3945-3954.

[140] N. Saravanan, G.B. Teh, S.Y.P. Yap, K.M. Cheong, Simple synthesis of ZnS nanoparticles in alkaline medium, J. Mater. Sci: Mater. Electron. **19**, (2008) 1206-1208.

[141] L. Sun, C. Liu, C. Liao, C. Yan, ZnS nanoparticles doped with Cu(I) by controlling coordination and precipitation in aqueous solution, J. Mater. Chem. **9**, (1999) 1655-1657.

[142] B. Tripathi, Y.K. Vijay, S. Wate, F. Singh, D.K. Avasthi, Synthesis and luminescence properties of manganese-doped ZnS nanocrystals, Solid-State Electronics **51**, (2007) 81-84.

[143] Y. Zhang, Y. Li, Synthesis and characterization of monodisperse doped ZnS nanospheres with enhanced thermal stability, J. Phys. Chem. B **108**, (2004) 17805-17811.

[144] Z. Rui, L. Yingbo, S. Shuqing, Synthesis and characterization of high-quality colloidal $Mn^{2+}$-doped ZnS nanoparticles, Opt. Mater. **34**, (2012) 1788-1794.

[145] L. Wang , S. Huang, Y. Sun, Low-temperature synthesis of hexagonal transition metal ion doped ZnS nanoparticles by a simple colloidal method, Appl. Surf. Sci. **270**, (2013) 178-183.

[146] G. Ghosh, M.K. Naskar, A. Patra, M. Chatterjee, Synthesis and characterization of PVP-encapsulated ZnS nanoparticles, Opt. Mater. **28**, (2006) 1047-1053.

[147] H. Hu, W. Zhang, Synthesis and properties of transition metals and rare-earth metals doped ZnS nanoparticles, Opt. Mater. **28**, (2006) 536-550.

[148] N. K. Abbas, K.T. Al-Rasoul, Z.J. Shanan, New method of preparation ZnS nano size at low pH, Int. J. Electrochem. Sci. **8**, (2013) 3049-3056.

[149] S. Ummartyotin, N. Bunnak, J. Juntaro, M. Sain, H. Manuspiya, Synthesis and luminescence properties of ZnS and metal (Mn, Cu)-doped-ZnS ceramic powder, Solid State Sci. **14**, (2012) 299-304.

[150] J.Z. Liu, P.X. Yan, G.H. Yue, L.B. Kong, R.F. Zhuo, D.M. Qu, Synthesis of doped ZnS one-dimensional nanostructures via chemical vapor deposition, Mater. Lett. **60**, (2006) 3471–3476.

[151] S. Senthilkumaar, R.T. Selvi, Synthesis and characterization of one dimensional zns nanorods, Synth. React. Inorg. Metal-Org. Nano-Met. Chem. **38**, (2008) 710-715.

[152] G.H. Yue, P.X. Yan, D. Yan, J.Z. Liu, D.M. Qu, Q. Yang, X.Y. Fan, Synthesis of two-dimensional micron-sized single-crystalline ZnS thin nanosheets and their photoluminescence properties, J. Cryst. Growth **293**, (2006) 42-432.

[153] H.J. Yuan, S.S. Xie, D.F. Liu, X.Q. Yan, Z.P. Zhou, L.J. Ci, J.X. Wang, Y. Gao, L. Song, L.F. Liu, W.Y. Zhou, G. Wang, Formation of ZnS nanostructures by a simple way of thermal evaporation, J. Cryst. Growth **258**, (2003) 225-231.

[154] Yi Xi, Chenguo Hu, Bin Feng, Xue Wang, Chunhua Zheng, Xiaoshan He, Synthesis of ZnS Nanoflowers by Composite-Hydroxide-Mediated Approach, J. Supercond. Nov. Magn. **23**, (2010) 901-903.

[155] H. Zhang, L. Qi, Low-temperature, template-free synthesis of wurtzite ZnS nanostructures with hierarchical architectures, Nanotechnology **17**, (2006) 3984-3988.

[156] B. D. Cullity, Elements of X-ray Diffraction, 2nd Ed., by Addison-Wesley (1978).

[157] A.L. Patterson, The Scherrer formula for X-ray particle size determination, Phys. Rev. Lett. **56**, (1939) 978-982.

[158] http://www.panalytical.com/XPert3-Powder.htm (Last accessed on 07.12.15)

[159] http://www.britannica.com/technology/transmission-electron-microscope (Last accessed on 07.12.15)

[160] http://www.fei.com/products/tem/tecnai/ (Last accessed on 07.12.15)

[161] http://iiti.ac.in/sic/index.php?q=eds (Last accessed on 07.12.15)

[162] http://www.synchronics.co.in/items/uv-vis-spectrophotometer-specord-205.aspx

[163] http://www.perkinelmer.com/Catalog/Product/ID/l2250107

[164] S. Foner, Versatile and Sensitive Vibrating-Sample Magnetometer Rev. Sci. Instrum. **30**, (1959) 548-557.

[165] http://www.lakeshore.com/products/Vibrating-Sample-Magnetometer/7400-Series-VSM/Pages/Overview.aspx (Last accessed on 21. 11.2015)

[166] S. Kumar, N.K. Verma, Ferromagnetic and weak superparamagnetic like behaviour of Ni-doped ZnS nanocrystals synthesized by reflux method, J. Mater. Sci. Mater. Electron. **25**, (2014) 1132-1137**.**

[167] L. Zhang, D. Qin, G. Yang, Q. Zhang, The investigation on synthesis and optical properties of ZnS:Co nanocrystals by using hydrothermal method, Chalcogenide Lett. **9**, (2012) 93-98.

[168] N. Dixit, N. Anasane, M. Chavda, D. Bodas, H.P. Soni, Inducing multiple functionalities in ZnS nanoparticles by doping $Ni^{+2}$ ions, Mater. Res. Bull. **48**, 2013, 2259-2267.

[169] Z. Jindal, N.K. Verma, Enhanced luminescence of UV irradiated $Zn_{1-x}Ni_xS$ nanoparticles, Mater. Chem. Phys. **124**, (2010) 270-273.

[170] D.P. Norton, M.E. Overberg, S.J. Pearton, K. Pruessner, Ferromagnetism in cobalt-implanted ZnO, Appl. Phys. Lett. **83**, (2003) 5488.

[171] J.H. Park, M.G. Kim, H.M. Jang, S. Ryu, Co-metal clustering as the origin of ferromagnetism in Co-doped ZnO thin films, Appl. Phys. Lett. **84**, (2004) 1338.

[172] S. Kumar, N.K. Verma, Structural, optical and magnetic investigations on Fe-doped ZnS nanoparticles, J. Mater. Sci. Mater. Electron. **26**, (2015) 2754-2759.

[173] K.T. Al-Rasoul, N.K. Abbas, Z.J. Shanan, Structural and optical characterization of Cu and Ni doped ZnS nanoparticles, Int. J. Electrochem. Sci. **8**, (2013) 5594-5604.

[174] C. Bi, L. Pan, M. Xu, L. Qin, J. Yin, Synthesis and characterization of Co-doped wurtzite ZnS nanocrystals, Mater. Chem. Phys. **116**, (2009) 363-367.

[175] Y. Li, C. Cao, Z. Chen, Magnetic and optical properties of Fe-doped ZnS nanoparticles synthesized by microemulsion method, Chem. Phys. Lett. **517**, (2011) 55-58.

[176] C.C. Chen, Y.J. Hsu, Y.F. Lin, S.Y. Lu, Superparamagnetism found in diluted magnetic semiconductor nanowires: Mn-Doped CdSe, J. Phys. Chem. C **112**, (2008) 17964-17968.

[177] S. Kumar, N.K. Verma, Room temperature magnetism in Co-doped ZnS nanoparticles, J. Supercond. Nov. Magn. **28**, (2015) 137-142.

[178] S. Lee, D. Song, D. Kim, J. Lee, S. Kim, I.Y. Park, Y.D. Choi, Effects of synthesis temperature on particle size/shape and photoluminescence characteristics of ZnS:Cu nanocrystals, Mater. Lett. **58**, (2004) 342-346.

[179] A.Z. Khosravi, M. Kundu, L. Jatwa S.K. Deshpande, U.A. Bhagwat, M. Sastry, S.K. Kulkarni, Green luminescence from copper doped zinc sulphide quantum particles, Appl. Phys. Lett. **67**, (1995) 2702.

[180] H. Chen, Y. Hu, X. Zeng, Green photoluminescence mechanism in ZnS nanostructures, J. Mater. Sci. **46**, (2011) 2715-2719.

[181] M.J. Iqbal, S. Iqbal, Synthesis of stable and highly luminescent beryllium and magnesium doped ZnS quantum dots suitable for design of photonic and sensor material, J. Lumin. **134**, (2013) 739-746.

[182] M. A. Shafique, S. A. Shah, M. Nafees, K. Rasheed, R. Ahmad, Effect of doping concentration on absorbance, structural, and magnetic properties of cobalt-doped ZnO nano-crystallites, Int. Nano Lett. **2**, (2012) 31.

[183] V. Gandhi, R. Ganesan, H.H.A. Syedahamed, M. Thaiyan, Effect of cobalt doping on structural, optical, and magnetic properties of ZnO nanoparticles synthesized by coprecipitation method, J. Phys. Chem. C **118**, (2014) 9715-9725.

[184] M.Y. Lu, L. J. Chen, W. Mai, Z. L. Wang, Tunable electric and magnetic properties of $Co_xZn_{1-x}S$ nanowires, Appl. Phys. Lett. **93**, (2008) 242503.

[185] S. Kumar, N.K. Verma, Effect of Ni-doping on optical and magnetic properties of solvothermally synthesized ZnS wurtzite nanorods, J. Mater. Sci. Mater. Electron. **25**, 2014, 785-790.

[186] Z. Yang, Q.H. Liu, H.C. Yu, B. Zou, Y.G. Wang, T.H. Wang, Substrate-free growth, characterization and growth mechanism of ZnO nanorods close-packed arrays, Nanotechnology **19**, 035704 (2008).

[187] J. Cao, D. Han, B. Wang, L. Fan, H. Fu, M. Wei, B. Feng, X. Liu J. Yang, Low temperature synthesis, photoluminescence, magnetic properties of the transition metal doped wurtzite ZnS nanowires, J. Solid State Chem. **200**, 317–322 (2013).

[188] W. Sang, Y. Qian, J. Min, D. Li, L.Wang, W. Shi, L. Yinfeng, Microstructural and optical properties of ZnS:Cu nanocrystals prepared by complex transformation method, Solid State Commun. **121**, (2002) 475-478.

[189] P.H. Borse, N. Deshmukh, Luminescence quenching in ZnS nanoparticles due to Fe and Ni doping, J. Mater. Sci. **34**, (1999) 6087-6099.

[190] Q.J. Feng, D.Z. Shen, J.Y. Zhang, Y.M. Lu, Y.C. Liu, X.W. Fan, Influence of Fe content on the structural and optical properties of ZnFeS thin films, Mater. Chem. Phys. **96**, (2006) 158-162.

[191] G. Zhu, S. Zhang, Z. Xu, J. Ma, X. Shen, Ultrathin ZnS single crystal nanowires: controlled synthesis and room-temperature ferromagnetism properties, J. Am. Chem. Soc. **133**, (2011) 15605–15612.

[192] C.J. Chen, W. Gao, Z.F. Qin, W. Hu, M. Qu, W. Giriat, Magnetization and magnetic susceptibility of the diluted magnetic semiconductors $Zn_{1-x}Co_xS$ and $Zn_{1-x}Co_xSe$, J. Appl. Phys. **70**, (1991) 6277.

[193] T.M. Giebultowicz, P. Klosowski, J.J. Rhyne, T.J. Udovic, J.K. Furdyna, W. Giriat, Magnetic exchange interactions in Co-based II-VI diluted magnetic semiconductors: $Zn_{1-x}Co_xS$, Phys. Rev. B **41**, (1990) 504.

[194] S.P. Patel, J.C. Pivin, A.K. Chawla, R. Chandra, D. Kanjilal, L. Kumar, Room temperature ferromagnetism in $Zn_{1-x}C_xS$ thin films with wurtzite structure, J. Magn. Magn. Mater. **323**, (2011) 2734–2740.

[195] S. Kumar, N.K. Verma, Investigation of the magnetic and optical properties of wurtzite Fe-doped ZnS nanorods, J. Electron. Mater. **44**, (2015) 2829-2834.

[196] S. Kumar, N.K. Verma**,** Room temperature investigations on optical and magnetic studies of $Zn_{1-x}Co_xS$ Nanorods, J. Magn. Magn. Mater. **374**, (2015) 548–552.

[197] X. Fang, U. K. Gautam, Y. Bando, B. Dierre, T. Sekiguchi, D. Golberg, Multiangular branched ZnS nanostructures with needle-shaped tips: potential luminescent and field-emitter nanomaterial, J. Phys. Chem. C **112**, (2008) 4735-4742.

[198] C. Corrado, Y. Jiang, F. Oba, M. Kozina, F. Bridges, J.Z. Zhang, Synthesis, structural, and optical properties of stable ZnS:Cu,Cl nanocrystals, J. Phys. Chem. A **113**, (2009) 3830-3839.

[199] D.A. Reddy, D.H. Kim, S.J. Rhee, C.U. Jung, B.W. Lee, Chunli Liu, Hydrothermal synthesis of wurtzite $Zn_{1-x}Ni_xS$ mesoporous nanospheres: With blue-green emissions and ferromagnetic Curie point above room temperature, J. Alloys Compd. **588**, (2014) 596-604.

[200] D. Amaranatha Reddy, C. Liu, R.P. Vijayalakshmi, B.K. Reddy, Structural, optical and magnetic properties of $Zn_{0.97-x}Al_xCr_{0.03}S$ nanoparticles, Ceram. Int. **40**, (2014) 1279-1288.

[201] D.A. Reddy, S. Sambasivam, G. Murali, B. Poornaprakash, R.P. Vijayalakshmi, Y. Aparna, B.K. Reddy, J.L. Rao, Effect of Mn co-doping on the structural, optical and magnetic properties of ZnS:Cr nanoparticles, J. Alloys Compd. **537**, (2012) 208-215.

[202] Z.H. Zhang, X. Wang, J.B. Xu, S. Muller, C. Ronning, Q. Li, Evidence of intrinsic ferromagnetism in individual dilute magnetic semiconducting nanostructures, Nat. Nanotech. **4**, (2009) 523.

## Appendix I: Various JCPDS data cards for ZnS

1. JCPDS data card no. 80-0020 (Cubic)

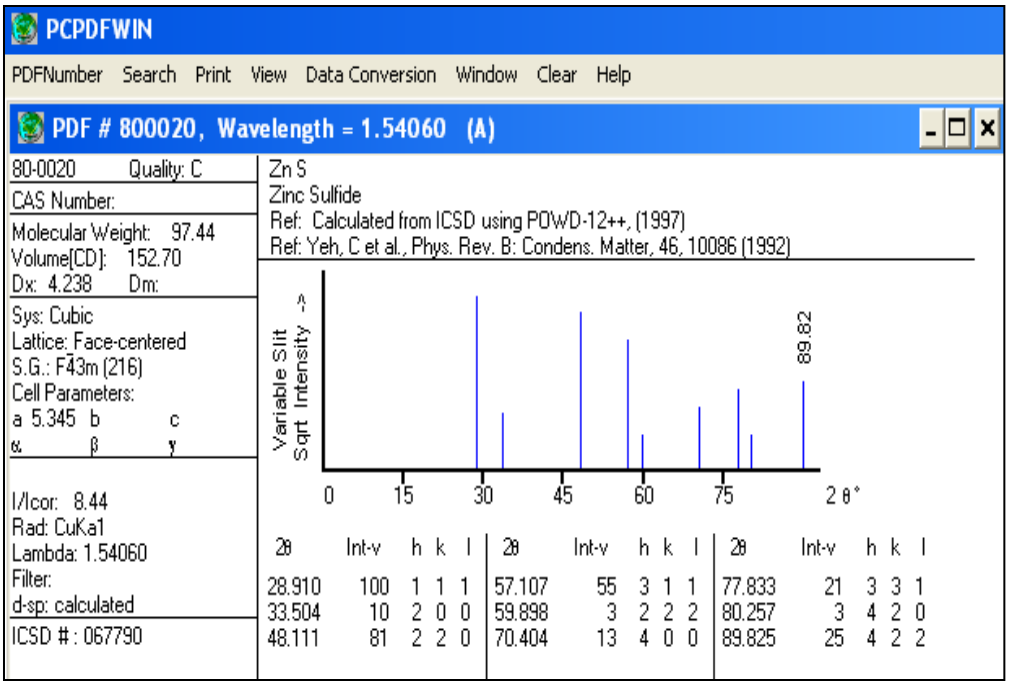


2. JCPDS data card no. 77-2100 (Cubic)

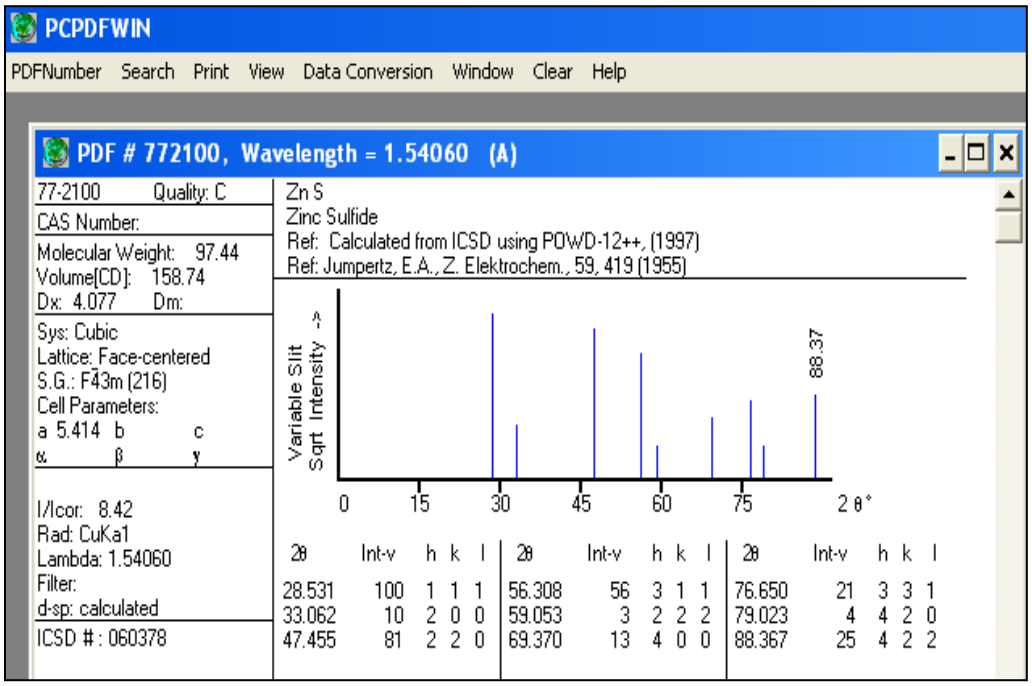

3. JCPDS data card no. 80-0007 (Hexagonal)

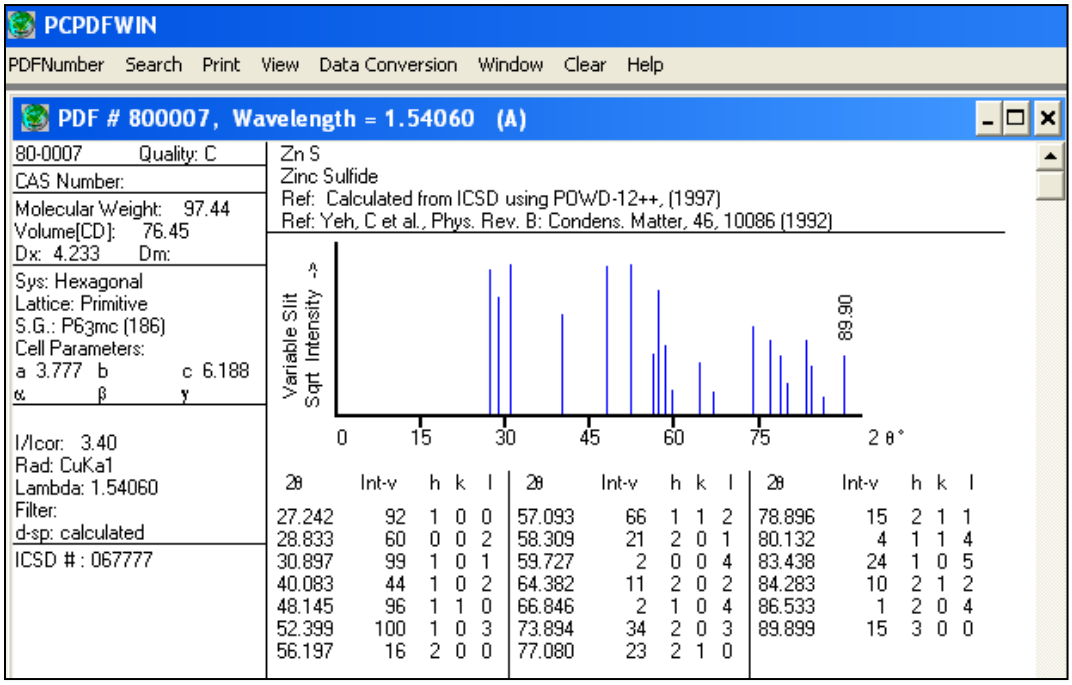


4. JCPDS data card no. 79-2204 (Hexagonal)

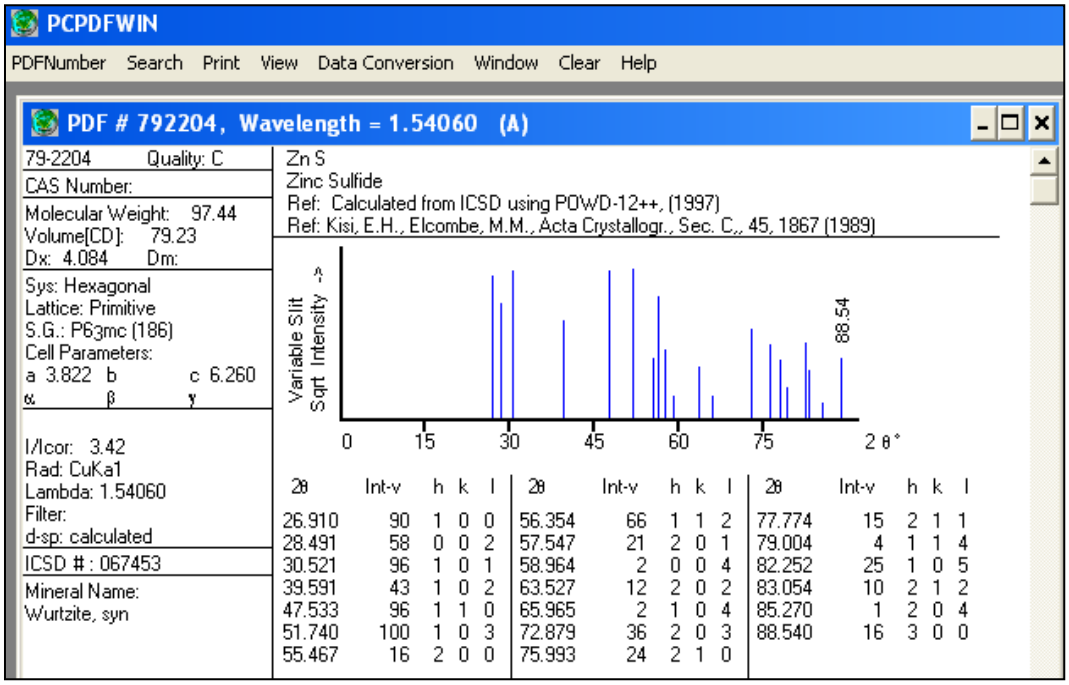

5. JCPDS data card no. 75-1547 (Hexagonal)

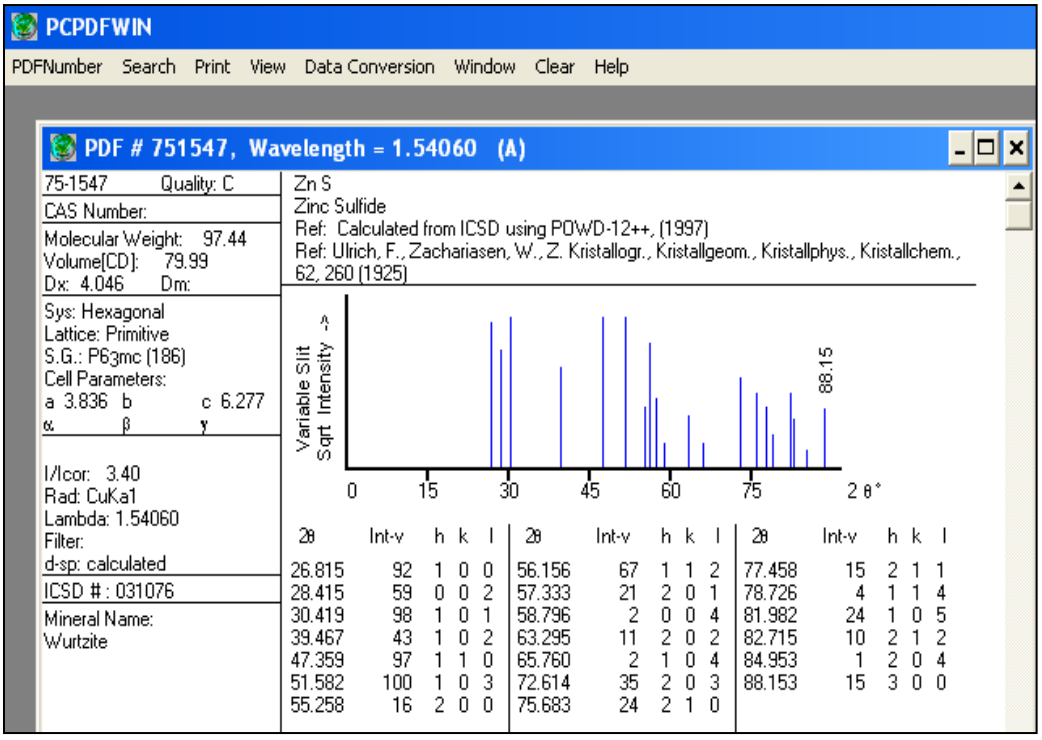


6. JCPDS data card no. 75-1534 (Hexagonal)